Technische Universität München
Institut für Energietechnik

Lehrstuhl für Thermodynamik

Hollow Cone
Spray Characterization
and Integral Modeling

Peter Bollweg

Vollständiger Abdruck der von der Fakultät für Maschinenwesen der Technischen Universität München zur Erlangung des akademischen Grades eines

DOKTOR-INGENIEURS

genehmigten Dissertation.

Vorsitzender: Univ.-Prof. Dr.-Ing. Hans-Jakob Kaltenbach

Prüfer der Dissertation: 1. Univ.-Prof. Wolfgang Polifke, Ph.D. (CCNY)
                         2. Univ.-Prof. Dr.-Ing. Georg Wachtmeister

Die Dissertation wurde am 01.12.2011 bei der Technischen Universität München eingereicht und durch die Fakultät für Maschinenwesen am 22.06.2012 angenommen.

Abstract

Gasoline direct injection (GDI) has been widely introduced in todays internal combustion engines for automotive applications. One way to increase the engines efficiency is to reduce throttling losses. This engine operation mode requires the stratification of the fuel air mixture within the combustion cylinder. Hollow cone injectors enable such mixture stratification.

The present work investigates the spray formation resulting from the injection of liquid fuel into air by a hollow cone injector. A methodological overview establishes the need of a fast spray model to simulate the engine operation at a system level. A detailed insight into the fluid mechanics of a hollow cone two-phase jet is obtained by means of a computational fluid dynamics (CFD) investigation. The model is validated experimentally both by the global penetration behavior and by the velocity field outside of the dense spray. Based on the characterization of the hollow cone two-phase flow, a one-dimensional model is derived. It describes the temporal evolution of the two-phase jet induced by the hollow cone injection process. Diffusive transport of mass, momentum, and energy between the dense spray zone and its environment is modeled by means of a boundary layer description.

Was wirklich zählt ist Intuition. (Albert Einstein)

Preface

The research work presented in this thesis was accomplished in the Gasoline Systems Advanced Development Team at Continental AG (formerly Siemens VDO Automotive AG) in Regensburg, Germany.

I express my special thanks to my thesis supervisor Prof. Wolfgang Polifke, Ph.D. Both his thorough insight into the topic and the fruitful discussions with him supported my progress to a great extend.

I also thank Prof. Dr.-Ing. Georg Wachtmeister for participating in the defense committee and Prof. Dr.-Ing. Hans-Jakob Kaltenbach for chairing the examination.

I am very grateful to Prof. Dr. André Kaufmann who introduced me to the interesting but complex subject of dispersed two-phase flows and initiated this thesis work. Him sharing his experience and ideas with me gave me a great ahead start in understanding two-phase flows and developing my own modeling ideas.

This research work was funded by Continental AG which I gratefully acknowledge. Special thanks are directed to Dr. Harald Bäcker in who's Combustion Team this research was conducted. I would also like to thank my colleagues within the combustions team for the good times and professional exchange. I am especially grateful to Dr. Christian Lohfink with whom I shared the researcher's fate.

Many thanks go to the two-phase flow group at the Lehrstuhl für Thermodynamik at Technische Universität München – namely Volker Kaufmann, Joao Carpintero, and Roland Kaess – for their open discussions at the chair and the pleasant times we spent during conferences and researching at CERFACS (Toulouse, France).

Eventually, I owe special thanks to my family, my wife and two sons, who spared some of my attention while I finished this work, and my parents, who lay the foundation to my personal and professional development years ago.

Stuttgart, July 2012

Peter Bollweg

Contents

Nomenclature

Roman letters

$\mathscr{D}$	diffusion coefficient	
$\mathscr{F}$, F	force	N
$\mathscr{L}$	length scale	m
$\mathscr{P}$	production rate	
$\mathscr{T}$	time scale	s
$\mathscr{U}$	velocity scale	m/s
C, c	constant, coefficient	
C_D	drag coefficient	
D	diameter	m
k	turbulent kinetic energy	$\mathrm{m^2\,s^{-2}}$
l	length	m
m, M	mass	kg
M_F	volume specific fuel vapor mass	kg/m
r	radial coordinates	m
x, y, z	cartesian coordinates	m
Y	species mass fraction	

Greek letters

α	volume fraction	
δ	boundary layer length scale	m
η	cross-stream cone coordinate	m
Γ	evaporating mass density source term	kg/m/s
λ	cross-stream cone coordinate	m
λ	thermal diffusion coefficient	$\mathrm{W\,m^{-1}\,K^{-1}}$
ϕ	circumferential coordinate	rad

Π	energy density source term	J/m/s
σ	surface density	1/m
τ	shear stress	N/m
τ_p	particle relaxation time	s
θ	cone half-opening angle	
ξ	streamwise cone coordinate	m

Non-dimensional numbers

Pe	Peclet number
Pr	Prandtl number
Re	Reynolds number
St	Stokes number
We	Weber number

Sub- and superscripts

τ	shear stress
(0)	initial
(c)	characteristic
c	fluid / carrier phase
F	fuel
i, j, k	indices
m	mixing / mixture
p	Particle or dispersed phase
T	turbulent

Abbreviations and acronyms

AV	artificial viscosity
BL	boundary layer
CFD	computational fluid dynamics
conv	convective
diff	diffusive

DPS	discrete particle simulation
DSZ	dense spray zone
EE	Euler-Euler
eff	effective
EL	Euler-Lagrange
entr	entrained
GDI	gasoline direct injection
ICE	internal combustion engine
LES	large eddy simulation
LIF	laser induced fluorescence
NS	Navier-Stokes
ODE	ordinary differential equation
PDE	partial differential equation
SGS	sub-grid scale
TPF	two-phase flow

1 Introduction

The development of internal combustion engines for automotive applications has been driven primarily by the international emission legislation and fuel efficiency. Until today, the focus of the legislation lay on the restriction of pollutant emissions, i.e. the unwanted side products resulting from combustion of the fuel-air mixture. In future, carbon-dioxide emission targets will additionally require the introduction of technologies to increase fuel efficiency.

In the context of gasoline internal combustion engines, the direct injection of the fuel into the combustion chamber is supposed to provide a substantial potential to reduce fuel consumption [106]. One advantage of injecting the fuel directly into the cylinder is the possibility of mixture stratification: Fuel may be injected so that an ignitable air-fuel mixture is positioned near the spark plug at the time of ignition while the total cylinder charge exhibits a lean quality. This engine operation enables to take the air into the cylinder at ambient pressure and thereby to reduce throttling losses.

The so-called first generation of gasoline direct injection (GDI) applied pressure swirl or multi-hole injectors to achieve mixture stratification [91]. The charge motion was used to redirect the ignitable air/fuel mixture towards the spark plug. The so called "wall guided" setup depends on a special piston bowl design to initiate a tumble motion of the cylinder charge [58]. Mixture stratification by a tumbling charge motion was also realized by appropriate intake port designs ("air guided"). The first generation GDI approach suffers from comparatively large cycle-to-cycle variations [26] and above all results in only limited fuel savings.

Second generation direct injection

Comparatively new to the market is the second generation direct injection – the so called "spray guided" – combustion setup [130]: Here, globally lean mixture qualities are provided with the help of an outward opening injector, which injects a liquid sheet at high pressure (figure 1.1).

The injector mounting position and orientation into the cylinder head causes the liquid sheet to be injected in the direction of the spark plug (figure 1.2 left). Due to the high intensity of supplied liquid phase momentum this combustion setup is fairly independent from the gas phase movement within the cylinder such as tumble or swirl (i.e. more resistant to cycle-to-cycle variations and more flexible in injection timings). This technology has demonstrated its potential to reduce fuel consumption by applying mixture stratification [110] and has been introduced to series production [74].
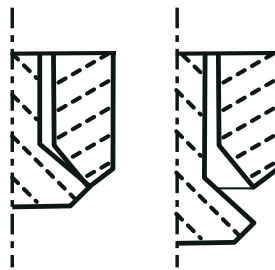
Figure 1.1: Outward opening hollow cone injector, closed (left) and open (right)

One major disadvantage of stratified engine operation is that the exhaust gas after-treatment with efficient and low-cost three-way catalysts is not sufficient. Therefore, the more expensive lean exhaust gas after-treatment has to be applied (NOx storage and oxidation catalysts). The time to achieve air/fuel mixing is shorter than cylinder external mixture preparation (port fuel injection). As a consequence, gradients in the mixture quality or even combustion at the surface of individual liquid fuel droplets may occur and result in increased soot formation.

Another challenge of direct injection is the engine's homogeneous op-

eration mode at increased and full load: It requires the injection of fuel as early as possible during gas exchange cycle. During such early injection (around the intake valve opening event), wetting of the intake valve with liquid fuel (figure 1.2 right) has to be avoided.

Simplified modeling

An increasing number of tasks during the development process is conducted with numerical investigations because they cost less than manufacturing prototypes and conducting experiments. Complex flows (such as an intake stroke or an injection event) are simulated with detailed methods such as computational fluid dynamics (CFD). By contrast, simple thermodynamic analysis may be conducted with space integral (zero-dimensional) models (figure 1.3). Due to the computational cost, detailed CFD analysis is restricted to the simulation of short physical times (i.e. one injection process). Optimization with regards to large data sets of operating conditions and/or design parameters is thus restricted to simplified models.

The injection induced two-phase flow within the cylinder incorporates comparatively complex physics. Moreover, the liquid fuel is exposed to time-variable boundary conditions (such as the cylinder pressure
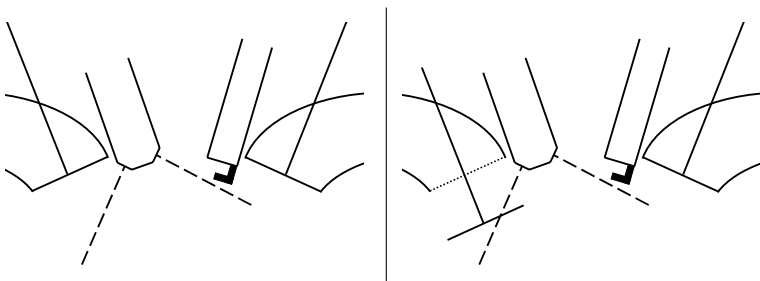
Figure 1.2: Spray guided gasoline direct injection concept, intake valves closed (left) and open (right)
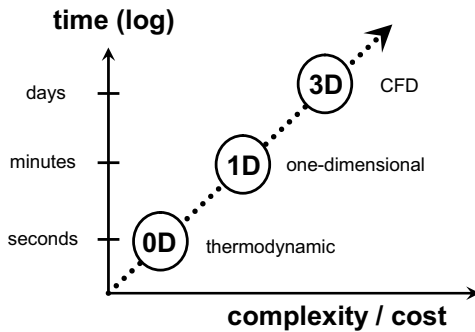
Figure 1.3: Calculation time depending on model complexity

during compression or acoustic waves in the injection system). If such dynamic response is to be incorporated into engine system simulation, its behavior has to be modeled. Because experiments only provide limited access to the involved physical quantities, it is therefore suitable to derive simplified models from an experimentally validated CFD model.

Thesis outline

This thesis is structured into three parts: a methodology section discussing the requirements of spray modeling for engine system simulation, a CFD section presenting a CFD model and its validation against experimental data, and a modeling section deriving a spray model for hollow cone sprays.

At first, the methodology section 2 discusses the physics relevant to injection processes and the different levels of modeling. The motivation for a simplified spray model for engine system simulation and a preliminary assessment of the hollow cone two-phase flow are presented.

The hollow cone injection process is investigated by means of three-dimensional CFD in section 3. The basic physical description is summarized in section 3.1. The transient evolution of spray characteristics is modeled by both Lagrangian and Eulerian two-phase flow descriptions. The CFD model's validation is based on carrier phase velocity measurements outside the dense hollow cone sheet. The sensitivity of both physical and numerical quantities is investigated. The CFD analysis (section 3.2) focuses on the mechanisms occurring due to interphase momentum exchange and the global flow structure due to the hollow cone geometry.

Based on the presented flow details, an integral model for the hollow cone injection process is proposed in section 4. It describes the transient evolution of the two-phase jet induced by the hollow cone injection process. Mass, momentum and energy equations are resolved in one spatial coordinate. Sources due to momentum exchange, droplet heat-up, and fuel evaporation are accounted for.
The model is explicitly suited for dense sprays. Diffusive transport of momentum, energy, and fuel species mass between the dense spray zone and its environment is modeled by means of a boundary layer description. The dense spray characteristics predicted by the model are assessed both qualitatively and in comparison to CFD data.

2 Modeling methodology

In order to deduce a simplified model for a hollow cone spray, the physical phenomena relevant to describe the two-phase jet need to be identified. For this reason, injection specific physics are shortly discussed in section 2.1 and the dominant effects for the injection into a cold gas environment are outlined. In section 2.2, an overview of the different levels of physical modeling is given. The detailed motivation for a simplified description for hollow cone sprays is presented in section 2.3. The preliminary assessment of an injection induced hollow cone flow (section 2.4) provides the basis for both the CFD investigation and the modeling approach presented in the later chapters.

2.1 Injection induced two-phase flow characterization

The spatial distribution of a liquid dispersed phase injected into a gaseous carrier phase environment is the result of several (interacting) basic physical phenomena. They are shortly reviewed in the following in order to emphasize their contribution to the overall evolution of the two-phase flow. Special attention is directed towards the process of inter-phase momentum exchange.

Basic physical phenomena

An injection induced two-phase flow is influenced by the *injector internal flow* (ejection direction, mean mass flow rate, etc.). The characteristics of the dispersed phase closed to the injector exit are the result of *primary breakup*, the formation of ligaments and droplets from a

liquid core. Due to slip with respect to the carrier phase, *secondary breakup* of bigger droplets into smaller ones occurs. Also due to slip, inter-phase *momentum exchange* dominates the local acceleration of both phases depending on their local mass loading. In *dense* zones (high dispersed phase concentration), droplets may collide and coagulate or again break up. Adjacent to the injection induced two-phase jet, a *shear layer* is formed within the carrier phase which counteracts local acceleration of carrier phase mass due to momentum exchange with the dispersed phase. Both within the shear layer and in the wakes of dispersed phase elements, *turbulent fluctuations* may occur and locally enhance mean transport. In a comparatively hot carrier phase environment moreover, *heat exchange* with the dispersed phase elements is non-negligible and *evaporation* takes place at their surface depending on the local carrier phase saturation state. If a liquid fuel is injected into air, the resulting local equivalence ratio determines the onset of *combustion*. Depending on the corresponding time scales, the strong *coupling* of the above mentioned physical phenomena heavily
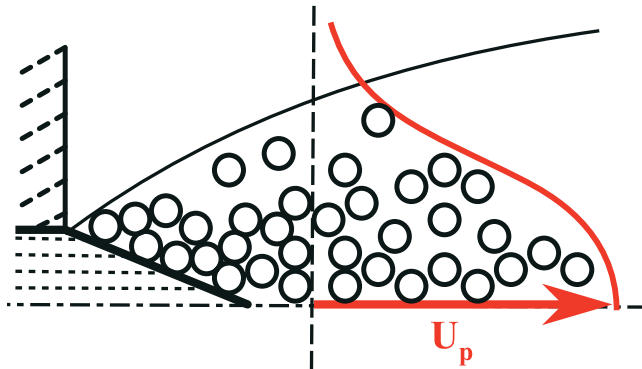
Figure 2.1: Liquid injection: Liquid core and dispersed droplets with resulting jet velocity profile; sketch

influences the dynamics of the individual effects.

Physical time scales

The application of an internal combustion engine incorporates a large range of physical time and corresponding length scales: For example, the transient engine-warmup process after a cold-start may take minutes until a cycle-stationary mean temperature is approximately reached. Transients in engine operating conditions such as engine speed and load are completed within seconds. One engine working cycle takes several milliseconds and the injection of small quantities lasts for times of the order of fractions of milliseconds.

On the other hand, cumulated small time scale effects dominate the large time scale behavior: The dynamics of e.g. mixture formation and combustion are influenced by turbulent fluctuations, which determine the local mixing rate of evaporated fuel and air. The inclusion of local turbulent fluctuations necessitates the spatial and temporal resolution of the smallest scales – namely the Kolmogorov scale at which turbulent eddies are consumed by viscous dissipation. Even when cycle-stationary conditions in the environment (e.g. for the cylinder head temperature) are reached based on the resolution of the smallest scales, the chaotic nature of turbulent fluctuations brings about cycle-to-cycle fluctuations [3]. In order to accurately describe the cycle-average transport due to turbulent fluctuations, several realizations of individual cycles have to be accounted for.

Momentum exchange

The momentum exchange of injected dispersed phase with the carrier phase is dominated by the local values of slip velocity and mass concentrations of both phases:

Momentum is locally exchanged if a particle's velocity differs from the carrier phase velocity (source term magnitude, drag force). The acceleration due to the resulting drag force acting on both phases de-

pends on the local mass concentrations. If no further momentum is supplied to the two-phase flow system, slip velocities decrease until both phases move with approximately the same velocity (*unforced* or *free system*): The injection process after injection has ended is characterized by a relaxation process.

By contrast during the injection process, momentum is continually supplied at the injection outlet so that velocity differences within the dense spray zone between both phases are maintained (*forced system*). After the injection has begun, the external forcing leads to increased penetration of dispersed phase into the carrier phase environment and to local acceleration of the carrier phase (spatially distributed forcing). The local pressure drop due to the accelerated carrier phase mass forces convective transport of carrier phase towards the dense spray zone in the direction normal to the main injection direction (entrainment). Also, the local carrier phase acceleration causes steep gradients in the carrier phase velocity profile so that tangential *shear stresses* due to the carrier phase's molecular viscosity are evoked. They cause the adjacent carrier phase mass to be accelerated (and the carrier phase mass exposed to momentum exchange with the dispersed phase to decelerate). The above mentioned transport of carrier phase mass normal to the main injection direction additionally enforces the formation of steep cross-stream gradients of the carrier phase streamwise velocity component.

The cumulative effect of local displacement (acceleration) of carrier phase mass due to momentum exchange as well as the shearing motion within the carrier phase and the consequential growth of the width of cross-stream velocity profiles is called *entrainment*. In a single phase jet, the cross-stream integral of streamwise momentum is conserved along the injection direction while the contained volume increases.

The flow field resulting from injection induced spatially distributed forcing of the carrier phase flow may be termed a *two-phase jet*. In a two-phase jet, the local acceleration of carrier phase mass causes an

additional *excess* entrainment of carrier phase mass into the two-phase jet.

Since the amount of carrier phase mass available for (excess) entrainment may be restricted both due to the chamber geometry (confined jet) and due to the rate of momentum diffusion, vortex structures are formed (*vortex formation*). Depending on their position and intensity, local entrainment of carrier phase mass is enhanced or reduced.

Breakup & poly-dispersion

The existence of dispersed phase elements like droplets within the domain results from liquid disintegration in the vicinity of the injector outlet due to instabilities within and at the boundary of the initially cohesive liquid (primary breakup) [25]. The instability of a liquid core surrounded by gas is a three dimensional and non-linear effect [69, 87]. Many works investigate the disintegration of liquid round jets injected in air (e.g. [85]) and the shear induced instability at the surface of liquid sheets [37, 66, 76, 78] and the resulting formation of droplets [103].

The processes involved with primary breakup result in a spatial and temporal distribution of droplet diameters and velocities which give the boundary condition for momentum exchange and secondary breakup. Models have been proposed to account for breakup mechanisms based on injector internal flow properties and geometrical boundary conditions both for round Diesel like jets [13] as well as for conical sheets (resulting from low pressure [32] or high pressure injection [111]). Such models have been implemented in CFD codes (e.g. [29]) and applied to gasoline direct injection applications [28, 123].

Dense dispersed phase coupling

If dispersed phase elements are influenced by the carrier phase flow but not vice versa, the two-phase flow is termed *one-way coupled*. With increasing local dispersed phase volume loading, the dispersed

phase elements influence the carrier phase flow (*two-way coupling*). If additionally, an increased local dispersed phase velocity dispersion occurs, dispersed phase elements directly influence each other (*four-way coupling*) by means of momentum, energy and species mass transport within the surrounding carrier phase [102]. Also, the probability of droplet collisions increases with increasing dispersed phase volume loading and velocity dispersion [6].

Usually correlations for momentum exchange (e.g. [107]) and evaporation (Spalding concept, described thoroughly in e.g. [73]) reproduce the mean transport at the surface of isolated droplets. Models for dense spray momentum exchange (four-way coupling) account e.g. for a cumulative drag force due to particle collective structures [86] or aligned droplet arrays [128].

In an evaporating dense spray, four-way coupling effects with regards to both momentum exchange and heat and mass transfer influence each other and lead to possibly complex interaction mechanisms, whose overall behavior may not be represented by correlations obtained from isolated droplet dynamics [9, 112].

The probability of droplet or particle collisions is modeled with statistical approaches [118] and supported by PDA measurements [119].

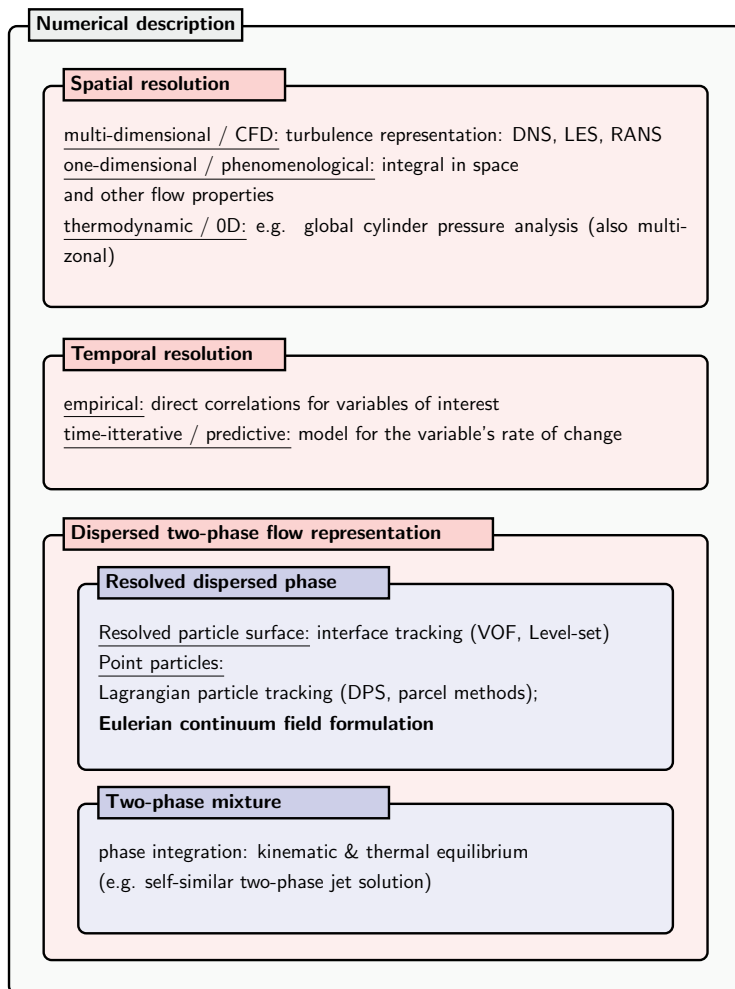The presence of dispersed phase elements influences the carrier phase
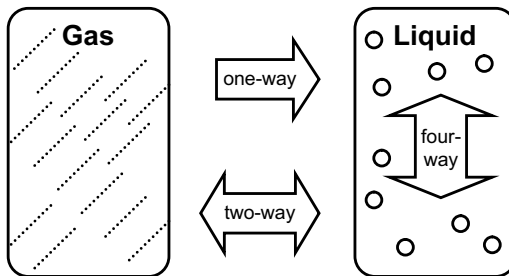
Figure 2.2: Two- and four-way coupling of dispersed two-phase flows

turbulence statistics [33]. The *turbulence modulation* within in-homogenous turbulent carrier phase flows at non-uniform particle mass loading is e.g. investigated by means of very sophisticated simulation approaches such as point-particle DNS [19, 120, 121]. Contributions to statistical modeling of two-phase turbulence effects also include kinetic models for joint probability density functions [53, 113, 115, 127]. More simple models accounting for turbulent transport in the context of the two-fluid model include two-equation two-phase turbulence models [46, 47] or simple gradient diffusion models [18, 79, 80].

2.2 Model classification overview

The underlying mean dynamics of both laminar and turbulent single-phase fluid flows are described in detail by numerous authors, e.g. [4, 11, 94, 108]. Dispersed two-phase flows are characterized both experimentally and numerically [22, 65]. Numerical methods providing high quality temporal integration solutions are proposed both with respect to single [52] and two-phase flows [96]. In order to later choose an appropriate model concept, a classification of numerical descriptions available for two-phase flows is presented in figure 2.3.

Any numerical simulation technique may be characterized by the degree of spatial homogeneity it assumes: Computational fluid dynamic models usually incorporate a spatial resolution in three dimensions. Turbulent fluctuations are resolved depending on their energy level: In a "direct numerical simulation" (*DNS*) approach, all scales down to the smallest ones being dissipated by molecular viscosity are resolved and no turbulence related modeling is required. In "large eddy simulation" (*LES*), a filter function is applied and the effect of scales smaller than the filter size on the resolved scales is modeled as a sub-grid viscosity. In the "Reynolds averaged Navier-Stokes" (*RANS*) description, the total of the Reynolds stress tensor is modeled and only the

Numerical description

Spatial resolution

multi-dimensional / CFD: turbulence representation: DNS, LES, RANS
one-dimensional / phenomenological: integral in space
and other flow properties
thermodynamic / 0D: e.g. global cylinder pressure analysis (also multi-zonal)

Temporal resolution

empirical: direct correlations for variables of interest
time-itterative / predictive: model for the variable's rate of change

Dispersed two-phase flow representation

Resolved dispersed phase

Resolved particle surface: interface tracking (VOF, Level-set)
Point particles:
Lagrangian particle tracking (DPS, parcel methods);
Eulerian continuum field formulation

Two-phase mixture

phase integration: kinematic & thermal equilibrium
(e.g. self-similar two-phase jet solution)

Figure 2.3: Numerical two-phase flow modeling methodologies

isotropic part is transported, e.g. in one- and two-equation turbulence models such as the k-ε, the k-ω-model or a combination of both like the "shear stress transport" (SST) model [88].

One-dimensional models describe integral properties in space such as pipe flow where only the dynamics along the pipe axis are spatially resolved and phenomena like friction forces within the flow and at the wall boundary are accounted for by loss coefficients. The modeling assumption of *self-similarity* also produces the projection of multi-dimensional effects onto only one (non-dimensional) similarity variable such as in single phase boundary layer flows*.

Purely *thermodynamic* models assume complete spatial homogeneity (zero-dimensional). For example, steady states within turbo-engines (stationary open system) are analyzed or transient work cycles as in reciprocating engines (transient closed system) may be characterized in this way.

The modeling approaches accounting for the *temporal evolution* incorporate mainly two types: Either the temporal development of the quantity of interest is provided in the form of an explicit function in time (such as the penetration depth of an injected jet), or the model describing the temporal rate-of-change of the quantity of interest is obtained from temporal integration (e.g. of the current particle velocity in order to obtain the particle's path). The latter kind of model represents the dynamics inherent to the described physical system and is therefore termed "predictive".

The appropriate numerical description of dispersed two-phase flows depends among other factors on the material densities of the phases involved. Here the focus lies on the flow induced in a gaseous carrier phase by a liquid dispersed phase. Hence, the dispersed to carrier phase material density ratio and consequentially also the momentum

---

* Furthermore assuming locally stationary conditions most often allows the derivation of an analytic solution from the remaining ODE so that the integral quantity is known a-priori and is not subject to numerical integration.

ratio in the vicinity of a dispersed phase element (particle) are of the order $\rho_p/\rho_c \approx 10^3 \gg 1$.

In advanced *two-phase descriptions*, the interface separating the two phases may be resolved, such as in interface tracking methods [125]. The volume of fluid method applies a discrete marker function indicating the phase jump-condition as a diffuse inter-phase. The level-set method incorporates a continuous marker function which enables a more precise reconstruction of the interface.

Less detail and thereby more computational efficiency provides the assumption that with regards to the global carrier phase flow pattern, the dispersed phase elements (droplets) occupy only a small volume and may therefore be characterized as *point-particles*, whose individual equation of motion defines their path (*Lagrangian particle tracking*) [57, 89, 95]. The detailed interaction with the carrier phase at the particle surface (drag, heat and mass transfer) is described by integral correlations obtained experimentally (such as drag correlations) or analytically (such as the Spalding droplet evaporation model). According to the level of detail in single phase turbulence modeling, the representation of the total amount of dispersed phase mass by individually tracked particles is termed "discrete" particle simulation (*DPS*). Because spatially neighboring particles of similar initial properties (e.g. diameter, velocity, temperature etc.) interact with approximately the same carrier phase mass elements, they tend to keep on carrying similar properties after the interaction. This physical effect suggests to model numbers of particles of similar properties to be grouped in *computational parcels*. The strongest advantage of the Lagrangian method is that it intrinsically incorporates a statistical representation of the dispersed phase property dispersion: The spatial and temporal development of distributions in e.g. diameter, velocity, temperature etc. due to some initial conditions is produced by the application of this method. If large amounts of particles (parcels) have to be tracked, the computational cost increases.

The *two-fluid method* applies volume or ensemble averaging to the

dispersed phase and thereby locally assigns continuum properties to the dispersed phase. The averaging process introduces a "one-point one-value" relation to the dispersed phase: If particles are to exhibit e.g. two different velocities at one location, two such continua have to be transported. A dispersed phase property dispersion may only be accounted for by a "spectral solution", where several continua represent the local distribution function. If the accuracy loss due to volume averaging is increased by such a spectral approach, the computational cost increases with the power of the covered dispersion relations (e.g. for diameter, velocity, and temperature with the power of three) so that the Lagrangian representation again becomes more attractive.

The least detailed method to treat dispersed two-phase flows is the *mixture model* which assumes both phases to be in kinematic and thermal equlilibrium by applying a local integration over both phases.

Eulerian multi-fluid

In the context of dispersed two-phase flow, a contradiction occurs when the Lagrangian statistical approach is used and turbulence effects are to be partly resolved as in LES. The increase in spatial resolution required for LES reduces the statistical quality of the dispersed phase representation. Also, spatial resolutions of the order of the local particle diameter contradict the point-particle assumption, introduce (possibly non-physically) high local gradients to the carrier phase and thereby necessitate the modeling of spatially distributed inter-phase coupling.

The field of high spatial resolution is thus a domain of the Eulerian continuum representation of the dispersed phase. The Eulerian turbulence modeling of the dispersed phase (which becomes important where $St = \tau_p/\tau_f \approx 1$) was introduced by [115] and further developed and implemented by [68, 75, 100]. An extension to poly-dispersion has been proposed by [90].

Eulerian moment transport & poly-celerity

The representation of dispersed phase property dispersion (e.g. regarding the local diameter or velocity distribution) was introduced with the Lagrangian statistical approach. The exact statistical probability of finding a particle with properties within a certain range of the total spectrum is described by the Williams spray equation [131]. With regards to the Eulerian dispersed phase transport, several approaches attempt to transport integrals of the distribution function, i.e. their moments.

Most interest lies in the representation of poly-dispersion, i.e. a distribution of particle diameters. The proposed methods contain the "method of moments" (*MOM*), where moments of the local particle diameter distribution are transported [14, 15, 16, 17] and which was further developed for impinging sprays [7] and applied to mass and heat transfer [23]. An alternative approach is the "direct quadrature method of moments" (*DQMOM*) [43, 48, 81, 84] which models the temporal change of a (possibly complex) diameter distribution by transporting convenient abscissas and weights representing the distribution function.

An important property of poly-dispersed systems is their non-linear response to momentum exchange with the carrier phase. Some models directly focus on the effect of the local dispersion in velocity (*poly-celerity*) [75]. Others relate the velocities at which diameter distribution moments are transported to some representative velocity for a representative diameter and introduce moment specific slip velocities to account for changes in the diameter distribution [14]. Yet another approach is to directly model moment velocities [56].

An alternative to modeling moments of the diameter distribution function is to reduce the computational cost of the full spectral solution. This is performed by relating the acceleration of particles corresponding to some class by the acceleration of a neighboring size class and thereby avoiding to solve momentum equations for some size classes.

For inertial particles of limited Stokes number this was introduced with the "equilibrium Eulerian approach" [50, 51] in the context of turbulent dispersion modeling. An extension of this approach enabling the transport of inertial particles of increased Stokes numbers has been suggested by the author and co-workers [21].

2.3 Motivation and modeling strategy

The improvement of the performance of a product like e.g. an injector or an engine necessitates a thorough understanding of the various relevant physical functionalities. In order to enhance the understanding of complex physical systems like an injection process, experimental and numerical investigations work in a complimentary manner. Depending on the required degree of detail and the available computational power, numerical models produce the response of dynamics of physical systems to certain initial and boundary conditions at different time scales: Some models feature real-time capabilities (such as "hardware in the loop" models for engine CPUs), while complex models incorporating a vast range of time and length scales (like e.g. climatic models) may require months of computational time on thousands of processors to produce results.

In an industrial context, even complex models (such as high resolution CFD models of an injection process) are supposed to produce results at the most within days so that then, changes in the model or the design may be applied. Processes like one single injection happen at characteristic time scales of milliseconds. By contrast, a transient engine system operation may take seconds or minutes. Depending on the engine speed, a significant number of working cycles with several injections per working cycle may need to be characterized (e.g. at 6000 rpm, 50 working cycles per second in a four-stroke engine).
The main physical effects present within an engine system – except

the injection and combustion cycle within the cylinder – may be described with sufficient accuracy by comparatively simple models (e.g. gas exchange dynamics or transient engine warm-up). Engine system simulation thus requires less computational power than a complex CFD analysis. On a desktop computer, several working cycles may be simulated within minutes. The injection of liquid fuel and the consequential combustion are most efficiently accounted for by experimentally obtained cylinder pressure traces. For this approach, engine hardware has to exist prior to any simulation work and engine system simulation is therefore applied as a post-processing tool to an experimental investigation.

By contrast during an early stage in the development cycle, engine system simulation is used to investigate major changes in engine geometry or operating conditions. Even though burn rates from previous engine applications may be adopted, such explicit functions lack the ability to respond dynamically to changes in boundary conditions (such as e.g. an altered thermodynamic state of the charge initially contained within the cylinder after the intake valve has closed). An approach to introduce dynamics to integral heat release characteristics has been presented by the author and co-workers [20]. The assessment scrutinizes the need to incorporate mixture formation effects resulting from the injection process into the engine system simulation, especially for gasoline engines.

Modeling limits

If numerical models of certain applications are first built, their accuracy is assessed applying comparisons to experimental data (*model validation*). Measurements include detailed investigations of isolated effects such as individual droplet kinematics or heat and mass transfer at isolated droplet surfaces. When models are to incorporate the cumulative effects of e.g. the propagation of a droplet cloud in initially quiescent air or the evaporation of a droplet cloud, often only integral

qualities such as the spray penetration depth into a pressure chamber or a spray life time may be obtained experimentally.

Especially for *dense* dispersed systems, to which optical measurement techniques provide only limited access, the link between the detailed dynamics on the level of individual droplets and the cumulative (integral) effects is very hard to establish: A breakup model may reproduce the temporal and spatial development obtained from a PDA investigation, but the question whether the congruence stems from correct modeling of the underlying individual droplet dynamics within the cloud (wind induced breakup, collision and coalescence, etc.) remains questionable. Likewise heat and mass transfer correlations obtained from experiments with isolated or a limited number of interacting droplets may produce an experimentally obtained spray life time. But the validation of individual droplet evaporation dynamics within a cloud of several hundreds of thousands of droplets is practically impossible. When high-detail models such as breakup models are applied with success, the (numerical) "path" at which the solution is obtained remains unclear and the congruence of results may well be the result of an interference of model errors, which cancel each other out. These effects introduce limits of applicability of computational dispersed phase transport descriptions like the Lagrangian particle tracking in dense spray zones [1, 38, 60] and demonstrate the need to locally introduce models accounting for integral effects in dense sprays.

Simplified modeling

Thorough documentation of basic physical dynamics and modeling is available with regards to the overall engine system [59], the gas dynamics within the intake and exhaust system [77], and spray injection and mixture formation [12, 122].

Among the simplified models for the overall engine system, the model part representing the processes happening within the cylinder after "intake valve closes" and before "exhaust valve opens" (cylinder model)

has to reproduce the most complicated dynamics. The need to introduce models more sophisticated than simple thermodynamical ones – accounting for the injection and mixture formation process at comparatively low computational cost – has been accentuated [20, 122]. Integral spray quantities like spray tip penetration depth or the global spray life time may be characterized by purely empirical correlations. Dynamic response to altered boundary conditions by contrast has to result from a dynamic, time-iterative (predictive) model.

Dispersed two-phase jet models

Several attempts have been made to dynamically describe injection induced propagation of a dispersed two-phase jet. The so called "packet model" of Hiroyasu [62] is aimed at the description of *round jet* Diesel spray and combustion modeling. With a somewhat reduced CFD philosophy, a limited region around the injector is resolved and explicit correlations for e.g. the spray tip velocity are given (two-phase mixture model). This approach has been adopted by several authors, e.g. [71].

Inspired by the space integral description of turbulent jet diffusion flames of Peters [92], Wan [129] presented a spray model for a round Diesel jet. The penetration behavior of the two-phase jet results from assumed cross-stream top hat profiles which represent the mean properties of both phases within the jet. It utilizes a parameter which accounts for the jet opening angle. Depending on this spreading rate, the local increase of carrier phase mass due to entrainment available for inter-phase momentum exchange is modeled. Breakup and evaporation are accounted for. Based on Hiroyasu's classification of a complete spray (locally homogeneous two-phase flow) [61], velocity differences between phases are completely neglected in a second step. From this assumption of a two-phase mixture, relations for spray tip penetration (which are explicit in time) are derived. After a first implementation in the context of [129], the model was validated for Diesel

injection applications [72].

With the assumption of a steady state condition within the main part of the round jet (except for regions very close to the injector and at the spray front), a square root dependency of the spray front penetration with time is found from the cross-stream integrated momentum equation. The accuracy of this description for Diesel jets is confirmed by e.g. [101] for various experimental data sets. For the description of the initially transient penetration behavior of a round fuel jet, Sazhin et al. [105] employed the individual droplet's kinematics as characteristic to the front propagation. In combination with models for evaporation and breakup, good agreement with experimental data was obtained.

Hollow cone sprays are much less commonly applied in industry than round fuel jets as typically found in Diesel engines. As a consequence, also less theoretical and characterization work has been performed. The major difference of a hollow cone spray is that its global structure is less stable than the spray structure resulting from a round jet (see section 2.4). It causes an injection induced global recirculation zone. This behavior was observed in experiments with *pressure swirl injectors* [29] as well as piezo-electrically driven, outward-opening injectors [97] and is again supported by the CFD investigation in section 3.2.

Cossali [31] studied the gas entrainment into a hollow cone spray based on a spatial self-similarity assumption and for steady state conditions (i.e. for constant boundary conditions and flow states long after the injector has opened). He confirms that the hollow cone jet dynamics resulting from an injection induced two-phase flow differ considerably from those of both single phase jets and round Diesel jets.

Model outline

In order to model a dynamic response to altered boundary conditions such as in an ICE environment, a *transient* two-phase description is the goal of this work. The first modeling priority lies on an adequate description of the deceleration of dispersed phase mass within the pressure chamber (momentum exchange). A sufficient accuracy of the momentum exchange early during injection is indispensable for the early development of the evaporation process (heat transfer towards the dispersed phase and consequential droplet warm-up). Hence, a *two-phase* description is chosen within this work. According to single phase jet theory [2], the dispersed phase is modeled to interact with an amount of carrier phase mass which increases along the injection direction (jet widening due to momentum diffusion). Additionally, jet boundary layer effects acting on the carrier phase mass within the two-phase jet are modeled which exceeds the contribution of [129]. The overall modeling process of the hollow cone injection induced two-phase flow at hand is supported and inspired by CFD investigations.
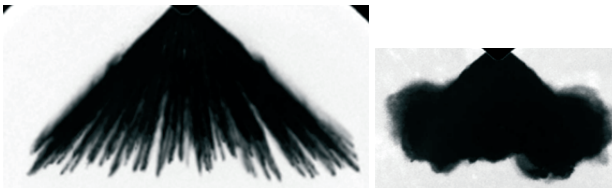
Figure 2.4: Hollow cone spray; spray images obtained from back-light photography; injection into carrier phase environment at 1 bar (left) and 15 bar (right) chamber pressure and 300 K chamber temperature [35]

2.4 Hollow cone injection

The spray structure resulting from a hollow cone injector depends on the carrier phase density: With increasing carrier phase density, the dispersed phase interaction with the carrier phase intensifies. As a result, the spray tip penetration length decreases and a more complex flow structure develops (figure 2.4).

The general dynamics of a two-phase jet apply also to the induced flow resulting from a hollow cone injection. Special about the hollow cone structure is its limited symmetry: Provided that the influence of the chamber geometry is negligible and that a rotationally perfectly symmetrical spray is provided by the injector, then the injector axis is a symmetry axis for the induced two-phase flow. With respect to the dispersed phase cone structure, the surrounding carrier phase reservoir is – by contrast – not symmetrical: At the outside of the hollow cone, a much greater volume of carrier phase is available (e.g. for entrainment) than at the inside. As a consequence, the flow in the vicinity of the dispersed phase is not symmetrical.
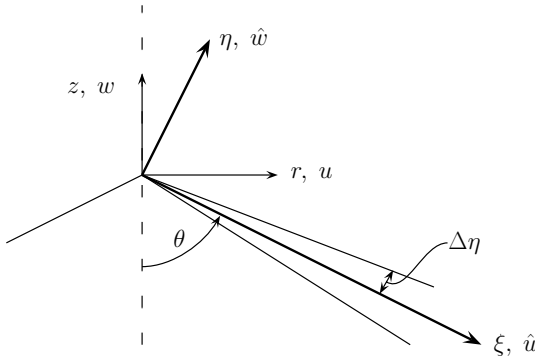
Experimental database

The spray provided by the high-precision, piezo-electrically driven, outward-opening injector [130] has been characterized experimentally in several investigations. They include the characterization of the global penetration behavior both in cold [35] and hot carrier phase environments obtained from back-light photography [10] as well as measurements of the carrier phase velocity field by means of PIV measurements [39, 40, 41, 42]. Of special benefit also for the present work are the investigations of Prosperi [97, 98], whose experimental data are used to validate the CFD model. Other investigations use optical measurement techniques in transient engine operating conditions [36, 83].

2.4.1 Conservation equations in conical coordinates

In order to emphasize the dominance of the injection direction of the dispersed phase hollow cone sheet, flow field results are presented in a conical coordinate frame (see figure 3.2.1). The hollow cone is characterized by a total cone opening angle of 2θ. The coordinate ξ indicates the penetration depth in injection direction along the liquid sheet on a presumed spray symmetry axis. The distance from the sheet normal to the main injection direction is characterized by the coordinate η.[†]

$$\xi = r \sin\theta - z \cos\theta \qquad \hat{u} = u \sin\theta - w \cos\theta \qquad (2.1)$$

$$\eta = r \cos\theta + z \sin\theta \qquad \hat{w} = u \cos\theta + w \sin\theta \qquad (2.2)$$

Figure 2.5: Conical coordinates

[†]The full derivation of conservation equations in cone coordinates is presented in detail in appendix A.

The equation of the conservation of mass (see eq. (A.6))

$$\frac{\partial \rho}{\partial t} + \frac{\partial(\rho\hat{u})}{\partial \xi} + \frac{\partial(\rho\hat{v})}{\partial \eta} + \underbrace{\rho \, \frac{\hat{u} \, \sin\theta + \hat{v} \, \cos\theta}{\xi \, \sin\theta + \eta \, \cos\theta}}_{RADconti} = \Gamma^{(evap)} \qquad (2.3)$$

relates the rate of change in mass density ρ to the mass fluxes and the mass source due to evaporation $\Gamma^{(evap)}$.

Momentum is conserved both tangential (see eq. (A.7))

$$\frac{\partial(\rho\hat{u})}{\partial t} + \frac{\partial(\rho\hat{u}^2)}{\partial \xi} + \frac{\partial(\rho\hat{u}\hat{v})}{\partial \eta} + \underbrace{\rho \, \frac{\hat{u}^2 \, \sin\theta + \hat{u}\hat{v} \, \cos\theta}{\xi \, \sin\theta + \eta \, \cos\theta}}_{RADmomX} = -\frac{\partial p}{\partial \xi} + \underbrace{I_\xi}_{dragX}$$

$$+ \mu_{eff} \left[\underbrace{\frac{\partial^2 \hat{u}}{\partial \xi^2}}_{\frac{viscX1}{\mu}} + \underbrace{\frac{\sin\theta \, \frac{\partial \hat{u}}{\partial \xi} + \cos\theta \, \frac{\partial \hat{u}}{\partial \eta}}{\xi \, \sin\theta + \eta \, \cos\theta}}_{\frac{viscX2}{\mu}} + \underbrace{\frac{\partial^2 \hat{u}}{\partial \eta^2}}_{\frac{viscX3}{\mu}} - \underbrace{\sin\theta \, \frac{\hat{u} \, \sin\theta + \hat{v} \, \cos\theta}{(\xi \, \sin\theta + \eta \, \cos\theta)^2}}_{\frac{viscX4}{\mu}} \right] \, ,$$

$$(2.4)$$

and normal to main injection direction (see eq. (A.8))

$$\frac{\partial(\rho\hat{v})}{\partial t} + \frac{\partial(\rho\hat{u}\hat{v})}{\partial \xi} + \frac{\partial(\rho\hat{v}^2)}{\partial \eta} + \underbrace{\rho \, \frac{\hat{u}\hat{v} \, \sin\theta + \hat{v}^2 \, \cos\theta}{\xi \, \sin\theta + \eta \, \cos\theta}}_{RADmomY} = -\frac{\partial p}{\partial \eta} + \underbrace{I_\eta}_{dragY}$$

$$+ \mu_{eff} \left[\underbrace{\frac{\partial^2 \hat{v}}{\partial \xi^2}}_{\frac{viscY1}{\mu}} + \underbrace{\frac{\sin\theta \, \frac{\partial \hat{v}}{\partial \xi} + \cos\theta \, \frac{\partial \hat{v}}{\partial \eta}}{\xi \, \sin\theta + \eta \, \cos\theta}}_{\frac{viscY2}{\mu}} + \underbrace{\frac{\partial^2 \hat{v}}{\partial \eta^2}}_{\frac{viscY3}{\mu}} - \underbrace{\cos\theta \, \frac{\hat{u} \, \sin\theta + \hat{v} \, \cos\theta}{(\xi \, \sin\theta + \eta \, \cos\theta)^2}}_{\frac{viscY4}{\mu}} \right] \, .$$

$$(2.5)$$

From the conservation equations, the cylindrical character is clearly visible. The cone specific terms appearing on the left hand side (LHS) of the set of equations (2.3) through (2.5) reflect the dependency on both the spatial coordinates and the velocity vector components. The fourth viscous term on the right hand side (RHS) of equations (2.4) and (2.5) directly corresponds to the cylindrical description. Special about the momentum conservation equations expressed in cone coordinates are the second viscous terms *viscX*2 and *viscY*2, which account for the spatial velocity gradients of the conserved momentum component.

Hollow cone boundary layer

The formulation of the momentum conservation equations in conical coordinates introduces viscous terms accounting for radial widening. In order to estimate the contribution of the individual terms in the streamwise momentum equation (2.4), the conservation equations (2.3) through (2.5) are assessed in terms of dimensionless variables for a boundary layer of characteristic thickness δ according to the procedure presented by Schlichting [108].

The momentum of the evaporating mass flux according to the continuity equation (2.3) is assumed to be much smaller than the convective fluxes in the streamwise momentum equation (2.4):

$$\hat{u}\,\Gamma^{(evap)} \ll \rho\,\hat{u}\,\frac{\partial \hat{u}}{\partial \xi}\;. \tag{2.6}$$

As result of a CFD model analysis (section 3.2) and according to the modeling approach presented later (section 4.3.2), effects of compressibility play a minor role in the hollow cone injection and the local mass density may be assumed to be approximately constant in time and space ($\rho \approx$ const.). Thus, the "primitive" version of the stream-

wise momentum conservation equation

$$\frac{\partial \hat{u}}{\partial t} + \hat{u}\,\frac{\partial \hat{u}}{\partial \xi} + \hat{v}\,\frac{\partial \hat{u}}{\partial \eta} = -\frac{1}{\rho}\,\frac{\partial p}{\partial \xi} + \underbrace{J_\xi}_{dragX}$$

$$+ v_{eff}\left[\underbrace{\frac{\partial^2 \hat{u}}{\partial \xi^2}}_{\substack{viscX1 \\ v}} + \underbrace{\frac{\sin\theta\,\frac{\partial \hat{u}}{\partial \xi} + \cos\theta\,\frac{\partial \hat{u}}{\partial \eta}}{\xi\,\sin\theta + \eta\,\cos\theta}}_{\substack{viscX2 \\ v}} + \underbrace{\frac{\partial^2 \hat{u}}{\partial \eta^2}}_{\substack{viscX3 \\ v}} - \underbrace{\sin\theta\,\frac{\hat{u}\,\sin\theta + \hat{v}\,\cos\theta}{(\xi\,\sin\theta + \eta\,\cos\theta)^2}}_{\substack{viscX4 \\ v}}\right]$$

$$(2.7)$$

is obtained[‡]. With the help of a macroscopic length scale $\mathscr{L}$ and a velocity scale $\mathscr{U}$, dimensionless variables $\xi^* = \xi/\mathscr{L}$, $\eta^* = \eta/\mathscr{L}$, $u^* = \hat{u}/\mathscr{U}$, $v^* = \hat{v}/\mathscr{U}$, $t^* = t\,\mathscr{U}/\mathscr{L}$ and $p^* = p/(\rho\mathscr{U})$ are defined so that the dimensionless momentum equation

$$\frac{\partial u^*}{\partial t^*} + u^*\,\frac{\partial u^*}{\partial \xi^*} + v^*\,\frac{\partial u^*}{\partial \eta^*} = -\frac{\partial p^*}{\partial \xi^*} + \frac{\mathscr{L}}{\mathscr{U}^2}\,J_\xi$$

$$+ \frac{1}{\mathrm{Re}}\left[\frac{\partial^2 u^*}{\partial \xi^{*2}} + \frac{\sin\theta\,\frac{\partial u^*}{\partial \xi^*} + \cos\theta\,\frac{\partial u^*}{\partial \eta^*}}{\xi^*\,\sin\theta + \eta^*\,\cos\theta} + \frac{\partial^2 u^*}{\partial \eta^{*2}} - \sin\theta\,\frac{u^*\,\sin\theta + v^*\,\cos\theta}{(\xi^*\,\sin\theta + \eta^*\,\cos\theta)^2}\right]$$

$$(2.8)$$

may be formed. The streamwise coordinate and velocity are of the order

$$\mathscr{O}(\xi^*) = 1 \quad \text{and} \quad \mathscr{O}(u^*) = 1\,. \qquad (2.9)$$

Within the boundary layer, η^* is of the order of the boundary layer

---

[‡] Note that the conical term on the left hand side of equation (2.4) termed *RAD-momX* is substituted by the mass conservation equation (2.3) when the "primitive" momentum conservation equation is derived.

thickness δ^*. In order to satisfy the dimensionless continuity equation

$$\frac{\partial u^*}{\partial \xi^*} + \frac{\partial v^*}{\partial \eta^*} + \frac{u^* \sin\theta + v^* \cos\theta}{\xi^* \sin\theta + \eta^* \cos\theta} = 0 \qquad (2.10)$$

also in the case of $\delta^* \to 0$ (Re $\to \infty$), v^* needs to be of the order of δ^* [108] because

$$\mathscr{O}\left(\frac{\partial u^*}{\partial \xi^*}\right) = 1 \quad \text{and} \quad \mathscr{O}\left(\frac{u^* \sin\theta + v^* \cos\theta}{\xi^* \sin\theta + \eta^* \cos\theta}\right) = 1 . \qquad (2.11)$$

At finite Reynolds number, the convective terms in equation (2.8) are of the orders of magnitude

$$\mathscr{O}\left(\frac{\partial u^*}{\partial t^*}\right) = 1 , \ \mathscr{O}\left(u^* \frac{\partial u^*}{\partial \xi^*}\right) = 1 , \ \mathscr{O}\left(v^* \frac{\partial u^*}{\partial \eta^*}\right) = 1 , \ \mathscr{O}\left(\frac{\partial p^*}{\partial \xi^*}\right) = 1 , \tag{2.12}$$

while those of the viscous terms are

$$\mathscr{O}\left(\frac{1}{\text{Re}}\right) = \delta^{*2} , \ \mathscr{O}\left(\frac{\partial^2 u^*}{\partial \xi^{*2}}\right) = 1 , \ \mathscr{O}\left(\frac{\sin\theta \frac{\partial u^*}{\partial \xi^*} + \cos\theta \frac{\partial u^*}{\partial \eta^*}}{\xi^* \sin\theta + \eta^* \cos\theta}\right) = \frac{1}{\delta^*} ,$$

$$\mathscr{O}\left(\frac{\partial^2 u^*}{\partial \eta^{*2}}\right) = \frac{1}{\delta^{*2}} , \ \mathscr{O}\left(\sin\theta \frac{u^* \sin\theta + v^* \cos\theta}{(\xi^* \sin\theta + \eta^* \cos\theta)^2}\right) = 1 . \tag{2.13}$$

Just like in the plane flow configuration, the viscous term incorporating the second order cross stream gradient $\frac{\partial^2 u^*}{\partial \eta^{*2}}$ is of the same order of magnitude as the convective fluxes in equation (2.8). Second in magnitude is the term *viscX2* due to the first order gradient $\frac{\partial u^*}{\partial \eta^*}$.

2.4.2 Two-phase jet dynamics

The carrier phase flow induced by the injection of a liquid jet differs fundamentally from the evolution of single phase jet.

Single phase jet

Consider a single phase viscous jet flow in steady state as depicted in figure 2.6. The fluid elements at the jet boundary δ (at a certain streamwise location x) travel at some finite (non-zero) streamwise velocity. This corresponds to a finite boundary layer thickness δ. The local change of the jet boundary layer thickness δ over time results from three contributions:

The local boundary layer thickness δ is exposed to a downstream convective transport (indicated by the velocity U_δ). If only convection would be considered, then the boundary layer thickness would shrink locally because of its decreasing width in the upstream direction ($\left.\frac{\partial \delta}{\partial t}\right|_{conv} < 0$)[§].
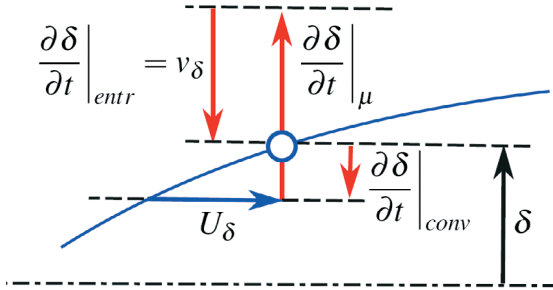
Figure 2.6: Rate of change $\frac{\partial \delta}{\partial t}$ of the jet boundary layer thickness δ due to convection, diffusion, and entrainment

---

[§] Note that in the case of pure convection, the boundary layer thickness δ in steady flow would be a path line. So the time-derivative of the local boundary layer thickness δ – whose streamwise location x is fixed in time and space – could also be understood as a Lagrangian derivative; in other words, the material derivative in that

At the same time, cross-stream diffusion of streamwise momentum causes the fluid outside of the boundary layer region to accelerate, thereby contributing to the local growth of the boundary layer thickness ($\frac{\partial \delta}{\partial t}\big|_\mu > 0$).

At the boundary layer boundary δ, mass is entering the jet region with a non-zero velocity component normal to the injection direction. This entrainment causes a contraction of the jet width δ (at the speed of the entrainment velocity $v_\delta(y = \delta) = \frac{\partial \delta}{\partial t}\big|_{entr} < 0$).

After the initial boundary layer growth (also referred to as a "startup process"), the three contributions named above approach an equilibrium state. The superposition of the three contributions is here referred to as the net diffusive boundary layer growth $\left(\frac{\partial \delta}{\partial t}\right)_\mu^{(net)}$, where

$$\left(\frac{\partial \delta}{\partial t}\right)_\mu^{(net)} = \frac{\partial \delta}{\partial t}\bigg|_{(t \gg \mathcal{T}_{shear}^{(c)})} = \frac{\partial \delta}{\partial t}\bigg|_{conv} + \frac{\partial \delta}{\partial t}\bigg|_\mu + \frac{\partial \delta}{\partial t}\bigg|_{entr} = 0\,.$$
$$(2.14)$$

In a single phase jet (resulting from a single point of momentum supply) and for a comparatively large boundary layer measure of choice (e.g. the displacement thickness δ_1), the velocity magnitudes at the jet boundary are comparatively small so that the entrainment velocity at the boundary layer border is small.

In a conventional single phase jet of incompressible media resulting from a single location of momentum supply, the total volume flux along the main injection direction remains constant, i.e. the stream-

---

case equals the convective derivative since no change in δ occurs along the streamwise coordinate x. In viscous flow however, the jet boundary layer thickness δ (and the mass contained within the jet) changes along the streamwise direction, so that – in general – the jet boundary does not lie on a path line. For this reason, the boundary layer evolution with respect to a steady (resting) coordinate frame is investigated here and the Eulerian derivative is used.

wise momentum contained within the jet cross section is conserved along the streamwise coordinate [108]. Along the injection direction, the cross-stream distribution of the streamwise momentum is rearranged to broader and flatter profiles due to momentum diffusion so that additional mass is *"entrained"* into the jet. As the jet spreads and an increasing volume normal to the injection direction is affected, the cross-stream peak of the streamwise velocity (the center line velocity) decreases.

Two-phase jet and "excess entrainment"

By contrast in the *two-phase jet* (here liquid droplets dispersed in air), additional streamwise momentum is introduced to the carrier phase as it travels downstream: Due to the injection process, the liquid droplets travel at a higher velocity than the carrier phase. The drag forces between both phases cause the carrier phase to be accelerated. Velocity differences and consequential drag do not occur at the point of injection only but are spatially distributed along the main injection direction ξ ("spatially distributed forcing").

The excess carrier phase mass flux caused by the drag with the dispersed phase has to be accomplished for by *additional entrainment* ("excess entrainment") of carrier phase mass into the jet volume. As a consequence from the entraining carrier phase mass, the boundary layer is locally contracted.

Both effects named above lead to a local increase of velocity gradients which again cause the shear stress within the carrier phase of the two-phase flow to increases.

Exemplary CFD results

As a more detailed insight into the dynamics of the injection induced two-phase flow field, an exemplary result from the CFD investigation provided later in this work (see sec. 3.2) is presented in figure 2.7. The horizontal line at $\eta = 0\,$mm is the presumed spray center line and the

diagonal line with $\eta < 0\,\text{mm}$ identifies the injector axis. The normed carrier phase velocity vector field is displayed. Due to the effect of spatially distributed acceleration of carrier phase mass, small vortex structures develop closed to the presumed spray center line. Their non-symmetrical arrangement with respect to the spray center line is outlined. In the middle of the hollow cone, the injector symmetry line dictates the flow direction. At greater distances from the spray center line, a global recirculation zone is formed both outside and inside of the hollow cone.

As long as the injection is in progress, the development of the carrier phase flow field along the injection direction (along ξ) is dominated by the spatially distributed forcing due to the injection of dispersed phase. By contrast in the direction normal to the main injection direction (along η), the induced carrier phase flow dominates the development of the dispersed phase spatial distribution. This is illustrated by figure 2.8 which contains velocity profiles extracted at the spray center line $\eta = 0\,\text{mm}$ at two successive time steps during injection. The dispersed phase velocity at $\xi = 0\,\text{mm}$ is defined by the injection boundary
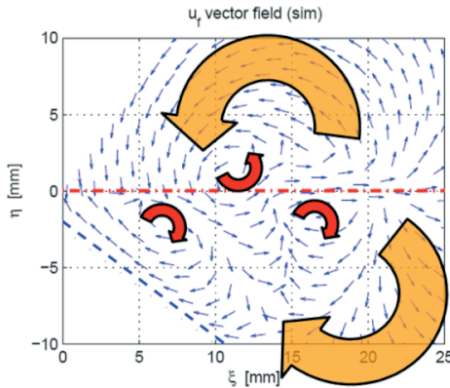

Figure 2.7: Carrier phase velocity vector field with vortices during injection

condition. With increasing penetration length ξ both the carrier and dispersed phase velocities decrease while a finite slip between both phases is maintained. With increasing time, a carrier phase cross-flow of increasing magnitude develops.

Self-similarity

In the context of a laminar boundary layer of a *single phase* flow over a *flat plate*, the velocity profile may be described in terms of a single similarity variable $\kappa = y/(2 \sqrt{\nu\, t})$, so that the linear PDE for $u(y,t)$ reduces to an ODE for $u(\kappa)$, for which an analytic solution may be derived, see e.g. Schlichting 2001 [108]. The temporal relaxation of the shear stress at the center line due to a suddenly induced forcing
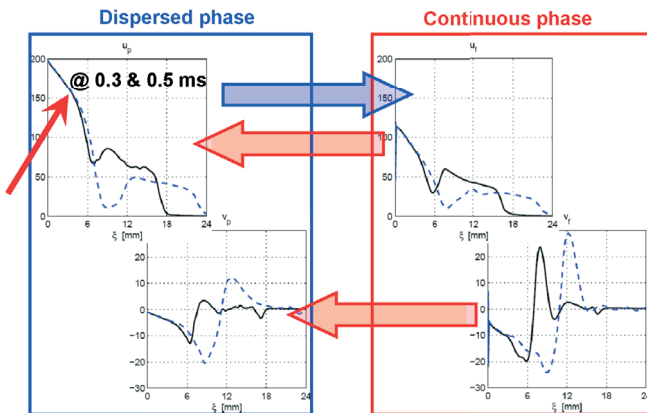
Figure 2.8: Kinetic energy flux within both phases during injection

("moving wall") velocity $U_c = u(\kappa \rightarrow 0)$ is then described by[¶]

$$\tau_c(U_c, t) = \mu \left. \frac{\partial u}{\partial y} \right|_c = -\rho \, U_c \sqrt{\frac{\nu}{\pi \, t}} \tag{2.15}$$

while the boundary layer thickness evolves over time according to

$$\delta = 3.6 \cdot \sqrt{\nu \, t} \, . \tag{2.16}$$

Turbulence

Turbulence effects are only accounted for with respect to the gaseous carrier phase. The level of turbulent fluctuations within the liquid phase resulting from the injector internal flow is neglected here.

Within the flow domain, maximum magnitudes of the carrier phase velocity are of the order of $\mathcal{O}(u_c) = 100\,\mathrm{m/s}$. The kinematic viscosity of the gas phase is assumed to be $\nu_c = 1.5 \times 10^{-5}\,\mathrm{m^2/s}$. When the injector is fully open, the half width associated with the effective cross-section of the exiting liquid flow is of the order of $\mathcal{O}(h/2) = 10\,\mu\mathrm{m}$. The Reynolds number

$$\mathrm{Re}_h = \frac{u_c \, h/2}{\nu_c} = 67 \ll 2 \times 10^5 \tag{2.17}$$

corresponding to the half-width $h/2$ indicates that no noteworthy turbulent intensity may be expected directly at the injector outlet.
On the level of individual particles, the slip velocity does not exceed $200\,\mathrm{m/s}$ (which corresponds to the limiting case of particles injected

---

[¶] For locally constant carrier phase center line velocity U_c, eq. (2.15) delivers the time rate of change of shear stress at the center line position

$$\left. \frac{\partial \tau_c}{\partial t} \right|_{U_c} = \frac{\rho \, U_c}{2} \sqrt{\frac{\nu}{\pi \, t^3}} \, .$$

at 200 m/s into quiescent air). The carrier phase flow around individual particles of diameter $\mathcal{O}(D_p) = 20\,\mu\text{m}$ may therefore be characterized by a Reynolds number of $\text{Re}_p = 267$. Anticipating the flow simulation result presented in figure 3.12, a carrier phase boundary layer thickness of the order of $\mathcal{O}(\delta) = 1\,\text{mm}$ at $\xi = 6\,\text{mm}$ is estimated. The streamwise centerline velocity depicted in figure 3.15 suggests a carrier phase velocity of about 50 m/s. The Reynolds number corresponding to the cross-stream length scale δ is of the order of $\text{Re}_\delta = 3300$.

In a steady state condition and neglecting mass and momentum exchange, the streamwise velocity at the centerline position (at $\eta = 0$) may be approximated from the continuity equation (2.3) [||]

$$u_c = u_c^{(0)} \frac{\xi^{(0)}}{\xi} \,. \tag{2.18}$$

Because $\frac{\partial^2 u_c}{\partial \xi^2} > 0$, a Reynolds number based on the length scale ξ increases monotonically with ξ. According to e.g. figure 3.15, you have roughly $\text{Re}_\xi = 3 \times 10^4$ at $\xi = 10\,\text{mm}$ ($u_c \approx 50\,\text{m/s}$) and $\text{Re}_\xi = 4 \times 10^4$ at $\xi = 20\,\text{mm}$ ($u_c \approx 30\,\text{m/s}$).

All Reynolds numbers estimated in this section are well below a critical Reynolds number of $\text{Re}_{crit} = 5 \times 10^5$ at which a transition from laminar to turbulent flow may be expected in single phase free stream flows [109]. Nevertheless, the presence of particles and the strong injection induced acceleration of carrier phase mass constitute strong disturbances to the gaseous phase flow so that turbulent fluctuations

---

[||] Applying the symmetry conditions $v_c|_{\eta=0} = 0$ and $\left.\frac{\partial v_c}{\partial \eta}\right|_{\eta=0} = 0$ at the centerline $\eta = 0$ in a steady state condition simplyfies the continuity equation (2.3) to

$$\frac{\partial u_c}{\partial \xi} + \frac{u_c}{\xi} = 0 \,.$$

Integration by separation of variables delivers $u_c \sim 1/\xi$.

may well occur below the critical Reynolds number known from single phase flow.

2.5 Summary

Computational models support today's product engineering. The simulation of an internal combustion engine system incorporates a large range of time scales. In an industrial development environment, suitable models need to produce results at the most within days in order to suggest design changes.

In the context of direct injecting gasoline engines, priority lies on the modeling of heat release and thus mixture formation. They result from an appropriate model of the injection process.

The analysis of the non-dimensional conservation equations for mass and momentum in a problem specific cone coordinate system reveal a dominance of the second order cross-steam gradients among the viscous fluxes in the streamwise momentum equation. In comparison to a single phase jet, additional ("excess") entrainment of gas is caused by the two-phase jet. The ability of the gas phase to transport momentum away from regions of dense spray determines the global spray front propagation. Although gas phase Reynolds numbers based on different length scales are below the critical Reynolds number for free stream flows, turbulent fluctuations are expected close to the dense spray zones due to the locally high velocity gradients induced in the two-phase flow by the injection of liquid fuel.

3 Dispersed two-phase flow analysis

The preliminary assessment of the two-phase flow induced by the injection of a dispersed phase presented in section 2.4 revealed the principal physical effects leading to the experimentally observed flow behavior (cf. figure 2.4):

The penetration behavior of the two-phase jet results from the momentum exchange between both phases in regions of high dispersed phase loading. The available experimental data characterizing the carrier phase flow field (cp. section 3.2.1 in this chapter) only provide access to flow regions comparatively far away from the dense spray zones and as a result do not allow to examine the carrier phase flow in regions of high dispersed phase loadings. For this reason, the hollow cone injection is investigated by means of a computational fluid dynamics (CFD) model, which provides access to flow properties within the whole flow domain.

As a basis for both the CFD investigation (and the chapter 4 on simplified modeling presented later), the mathematical description applied to two-phase flows is recapitulated in section 3.1. The CFD model settings are presented in section 3.1.4.

In section 3.2, the flow results from the CFD model are presented. The first part contains the validation of the CFD model on the basis of measured carrier phase velocity fields. Then, the inter-phase momentum exchange and the induced carrier phase flow are discussed in detail.

3.1 Two-phase flow description

Conservation laws are usually derived from a volume integral over a material element: The accumulation of quantity ψ within the volume element V_m is composed by the influx $\dot{\psi}_{in}$ over the volume element surface A_m and the rate of production $\dot{\psi}_{source}$ of ψ within volume element V_m.

$$\frac{\partial}{\partial t} \int_{V_m} \psi \, dV = - \oint_{A_m} \dot{\psi}_{in} \, dV + \int_{V_m} \dot{\psi}_{source} \, dV \tag{3.1}$$

If the spatial distribution of ψ is sufficiently smooth for spatial derivatives to exist (continuity assumption), the general conservation law for the quantity ψ in differential form

$$\underbrace{\frac{D\psi}{Dt}}_{\text{Lagrangian time derivative}} = \underbrace{\frac{\partial \psi}{\partial t}}_{\text{rate of change}} + \underbrace{\frac{\partial (\psi u_j)}{\partial x_j}}_{\text{convection}} = \underbrace{-\frac{\partial \Phi_j}{\partial x_j}}_{\text{surface flux}} + \underbrace{\dot{\psi}_{source}}_{\text{volume source}}$$

$$\tag{3.2}$$

with the diffusion flux Φ may be obtained.

In accordance with Newton's second law, the acceleration of mass per unit volume depends on the net force it is exposed to (with the stress tensor σ_{ij} and force vector F_i).

$$\frac{D(\rho u_i)}{Dt} = \frac{\partial \sigma_{ij}}{\partial x_j} + F_i \tag{3.3}$$

For Newtonian fluids with constant material properties, a linear dependence of the stresses on the time rate of strain, respectively velocity gradients, is assumed (e.g. to describe one-dimensional wall shear stress according to $\tau_w = \mu \frac{\partial u}{\partial y}|_w$).

The stress tensor σ_{ij} may be expressed in terms of an isotropic (symmetric) part representing the normal (hydrostatic) stress ($p = \sigma_{kk}/3$) and a deviatoric (anti-symmetric) part containing the tangential stresses

acting on a fluid element [93]

$$\sigma_{ij} = -p \, \delta_{ij} + \tau_{ij} \, . \qquad (3.4)$$

The deviatoric (viscous) stress tensor τ_{ij} depends on the rate of strain tensor S_{ij} *

$$\tau_{ij} = 2\mu \, S_{ij} \qquad \text{with} \qquad S_{ij} = \frac{1}{2} \left(\frac{\partial u_i}{\partial x_j} + \frac{\partial u_j}{\partial x_i} \right) \, . \qquad (3.5)$$

Insertion of the above produces the well known Navier-Stokes equations. They describe the time-dependent movement of a continuous compressible fluid in space based on the rate of change in velocity

---

* The effect of a non-linear relation emerges for flows with fast varying density (such as acoustic wave propagation or shock). Then the fluid is subject to an additional viscocity contribution called volume viscosity or bulk viscosity which resists to sudden volume expansion or contraction. In this case, the stress tensor is not soleniodal so that $\frac{\partial u_i}{\partial x_i} \neq 0$ and with the Stokes hypothesis ($\mu^{(2)} = -2/3\mu$), eq. (3.4) becomes [70]

$$\tau_{ij} = 2\mu \left(s_{ij} - \frac{1}{3} s_{ii} \delta_{ij} \right) = \mu \left(\frac{\partial u_i}{\partial x_j} + \frac{\partial u_j}{\partial x_i} - \frac{2}{3} \frac{\partial u_i}{\partial x_i} \right) .$$

depending on the pressure field and viscous stress forces[†]

$$\frac{\partial \rho}{\partial t} + \frac{\partial (\rho u_j)}{\partial x_j} = S \,, \tag{3.6}$$

$$\frac{\partial (\rho u_i)}{\partial t} + \frac{\partial (\rho u_i u_j)}{\partial x_j} = -\frac{\partial p}{\partial x_i} + \frac{\partial \tau_{ij}}{\partial x_j} + F_i \,. \tag{3.7}$$

3.1.1 Continuous phase transport

In the description of dispersed two-phase flows, the conservation of the (bulk) carrier phase mass per unit volume $\overline{\rho}_c = (\alpha_c \rho_c)$ is described applying the Navier-Stokes equations.

$$\frac{\partial \overline{\rho}_c}{\partial t} + \frac{\partial (\overline{\rho}_c u_{c,j})}{\partial x_j} = \Gamma^{(evap)} \,, \tag{3.8}$$

$$\frac{\partial (\overline{\rho}_c u_{c,i})}{\partial t} + \frac{\partial (\overline{\rho}_c u_{c,i} u_{c,j})}{\partial x_j} = -\frac{\partial p_c}{\partial x_i} + \frac{\partial}{\partial x_j} \left(\mu_c \frac{\partial u_{c,j}}{\partial x_j} \right) + \mathscr{F}_{D,i} \,. \tag{3.9}$$

The source terms account for mass transfer due to evaporation ($\Gamma^{(evap)}$) and momentum exchange with the dispersed phase ($\mathscr{F}_D$).

[†] The Navier-Stokes equation (or more specifically the momentum conservation equation) is a non-linear, second order PDE which is broadly applied when solving fluid dynamic problems. In spite of its universal acceptance (which is based on the high accuracy solutions it produces when integrated numerically) it is noteworthy that the unrestricted existence of solutions is not proven to the present day, just like the general smoothness of such solutions (the universal exclusion of discontinuities and singularities). Both problems belong to the top ten unsolved mathematical problems today [49].

3.1.2 Dispersed phase transport

One important aspect in two-phase flow CFD is the representation of the dispersed phase. Two major approaches exist.

Lagrangian

In the Lagragian description, the path of the dispersed phase elements (here also termed "particles" and therefore indexed "p") is obtained from solving an equation of motion for individual particles ("Lagrangian particle tracking")

$$m_p \frac{Du_{p,i}}{Dt} = \mathscr{F}_{D,i} \,. \tag{3.10}$$

This equation accurately describes the path of particles when the dispersed phase is dilute, i.e. if the time τ_p characterizing the relaxation of fluid forces acting on the particle (see eq. (3.28)) is much smaller than the characteristic time between inter-particle collisions $\mathscr{T}_{coll}^{(c)}$.
The diluteness of dispersed two-phase flow may also be characterized when the mean distance between particles L_p is than their diameter D_p: For a ratio $L_p/D_p > 10$ it may well be assumed that collisions do not dominate the dispersed phase movement. This corresponds to a dispersed phase volume fraction of $\alpha_p < 10^{-3}$.
When the diluteness assumption is applied in CFD analysis of injection processes, the effect of volume displacement due to the presence of dispersed phase is generally neglected with regard to the carrier phase transport: In equation (3.8), the carrier phase volume fraction is set to $\alpha_c = 1$ and consequently $\overline{\rho}_c = \rho_c$.

The obvious advantage of the Lagrangian dispersed phase representation – that each dispersed phase element is assigned its unique characteristics – also bears limitations to its applicability: The number of particles summing up to a constant dispersed phase mass increases when smaller particles are transported ($n_p \sim D_p^{-3}$, see eq. (3.11)), so that the demand for both computation power and storage requirements

rises accordingly.

Another problem resulting from the Lagrangian description arises when the spatial resolution of the computational mesh is increased to or above the order of the mean particle diameter such as in the context of DNS or LES of turbulent reactive two-phase flows, e.g. [30, 44]. If the spatial resolution is of the order of the dispersed phase diameter, the dispersed phase concentration may locally no longer be assumed to be dilute. The resulting increased dispersed phase volume fractions then also introduce discontinuities to the carrier phase mass conservation equation.

Eulerian

An alternative to the tracking of the individual particle paths is a continuum formulation for the dispersed phase. It is obtained from an averaging procedure [45].

With regards to turbulence effects in a dilute two-phase flow with solid particles, Simonin et al. [115] derive a continuum formulation by means of *ensemble averaging* based on the kinetic theory of gases. Similar to the LES approach, a continuum formulation for the dispersed phase may also be derived by *volume filtering* [114]. Here, the existence of the Navier-Stokes equations for both phases is assumed. A sub-grid energy is identified which accounts for the uncorrelated motion at length scales below the filter size (which in numerical simulation is identical to the mesh size). Among other contributions, it results from gradients in the dispersed phase velocity and contributes as a diffusion term to the dispersed phase momentum transport. Both derivations are compared in [68].

The solver used in this investigation [5] applies a simplified conservation equation based on volume filtering for the dispersed phase volume fraction

$$\alpha_p = n_p \, \frac{\pi}{6} \, D_p^3 \, . \tag{3.11}$$

No pressure (and therefore no pressure gradient) is assigned to the dispersed phase liquid. No sub-grid energy conservation is solved. A mean viscosity μ_p is assigned to the dispersed phase and the diffusion of dispersed phase momentum is modeled by a simple gradient diffusion hypothesis.

$$\frac{\partial(\rho_p\alpha_p)}{\partial t} + \frac{\partial(\rho_p\alpha_p u_{p,j})}{\partial x_j} = -\Gamma^{(evap)} , \tag{3.12}$$

$$\frac{\partial(\rho_p\alpha_p u_{p,i})}{\partial t} + \frac{\partial(\rho_p\alpha_p u_{p,i} u_{p,j})}{\partial x_j} = \frac{\partial}{\partial x_j}\underbrace{\left(\mu_p\frac{\partial u_{p,j}}{\partial x_j}\right)}_{\sigma_p} - \mathscr{F}_{D,i} . \tag{3.13}$$

Formally, both equations are similar to the description of the carrier phase (eqs. (3.8) and (3.9)). Note that in order to conserve volume, the carrier phase volume fraction is generally $\alpha_c \leq 1$.

The key issue with the Eulerian description of dispersed two-phase flow is the modeling of the stress tensor σ_p (or the apparent particle viscosity μ_p). It may e.g. incorporate mean stresses resulting from inter-particle collisions (resulting in diagonal contributions or pressure terms assigned to the dispsersed phase) or turbulent fluctuations of the dispersed phase velocity [68, 100].

The major shortcoming emerging with the Eulerian representation of the dispersed phase results from the averaging process: For each dispersed phase characteristic (e.g. temperature, particle diameter, or velocity), only one (average) may be transported. Especially the representation of poly-dispersion (multiple particle diameters) or poly-celerity (multiple velocities, e.g. in the case of two dilute and possibly inter-penetrating jets resulting from two different injection directions) may not be described with the conventional (two-fluid) model. Several contributions have been proposed accounting for poly-dispersion [90] and poly-celeridity [43, 75] by transporting additional integrals of the particle size distribution and introducing additional source terms (see sec. 2.2).

3.1.3 Source terms

The two-phase flow resulting from an injection process is dominated by the local slip between dispersed and carrier phase. As a consequence, the drag force is assumed to dominate the momentum exchange and other accelerations such as gravity are neglected. The slip velocity also influences the local environment of the evaporating liquid. The effects considered in this thesis are described in detail e.g. in [22, 73, 116] and are shortly summarized in the following.

Evaporation

The description of the evaporation process at the surface of isolated droplets is based on the assumption that in the vicinity of the droplet surface (within the saturated gas-vapor mixture), the diffusive fluxes of heat towards and mass away from the liquid droplet surface are in an equilibrium condition. The analysis of the diffusive mass transport
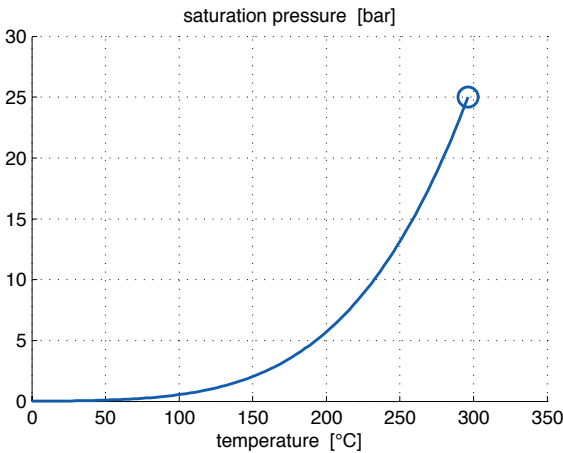
Figure 3.1: Saturation pressure of octane (C_8H_{18}) with critical point ($p_{cr} = 2.5\,\text{MPa}$, $T_{cr} = 569.3\,\text{K}$) and latent heat $\Delta h_v = 301.2\,\text{kJ/kg}$

in the vicinity of an isolated droplet's surface leads to the well known D^2-law. It describes the decrease of the square of the droplet diameter to be linearly dependent on time

$$D_p^2 = (D_{p,0})^2 - \beta_{Spald} \, t \, .$$

$$(3.14)$$

The Spalding coefficient

$$\beta_{Spald} = 8 \, \frac{\rho_{Fs} \, \mathscr{D}_{Fs}}{\rho_p} \, \ln(1 + B_M)$$

$$(3.15)$$

incorporates the mass diffusion potential

$$B_M = \frac{Y_{Fs} - Y_{F\infty}}{1 - Y_{Fs}}$$

$$(3.16)$$

between the mass concentrations of fuel vapor in the saturated film (with fuel species mass fraction Y_{Fs}) and in the undisturbed surrounding ($Y_{F\infty}$). $\mathscr{D}_s$ quantifies the material diffusion coefficient within the saturated mixture at the droplet surface.

The saturated fuel vapor concentration Y_{Fs} is calculated from the molecular masses of the pure carrier phase gas m_c and the saturated gas vapor mixture m_s where p_c is the carrier phase pressure and p_s is the saturation pressure according to the Clausius-Clapeyron equation (latent heat Δh_v, gas constant of saturated mixture R_s).

$$Y_{Fs} = \frac{p_s m_s}{p_s m_s + (p_c - p_s) m_c} \quad \text{and} \quad p_s = p_{ref} \cdot \exp\left\{ \frac{\Delta h_v}{R_s} \left(\frac{1}{T_{ref}} - \frac{1}{T_l} \right) \right\}$$

$$(3.17)$$

The evaporating fuel mass flow rate at the surface of an isolated droplet is

$$\Gamma_{iso}^{(evap)} = -\rho_p \, \frac{\partial (\frac{\pi}{6} D_p^3)}{\partial t} = \frac{\pi}{4} \, \rho_p \, D_p \, \beta_{Spald}$$

$$(3.18)$$

so that the total evaporating mass flow rate of n_p particles per unit volume is simply

$$\Gamma^{(evap)} = n_p \, \frac{\pi}{4} \, \rho_p \, D_p \, \beta_{Spald} \, . \tag{3.19}$$

The characteristic time for the evaporation process is the droplet life time

$$\mathcal{T}_{evap}^{(c)} = \frac{D_{p,0}^2}{\beta_{Spald}} = \frac{\rho_p D_{p,0}^2}{8 \, \rho_{s,c} \, \mathcal{D}_s \, \ln(1 + B_M)} \, . \tag{3.20}$$

Note that the characteristic time needed for a droplet to reach the equilibrium temperature is of the order $\mathcal{T}_{heatup}^{(c)} = \mathcal{O}(\rho_l C_l D_p^2 / \lambda_l)$. Generally it may be estimated [116] that

$$\frac{\mathcal{T}_{heatup}^{(c)}}{\mathcal{T}_{evap}^{(c)}} = 2 \, \frac{\lambda_c}{\lambda_p} \, \frac{C_{v,c}}{C_p} \, \ln(1 + B_M) \ll 1 \tag{3.21}$$

so that from the energy flux equilibrium at the saturated droplet surface ($\frac{\partial T_s}{\partial t} = 0$), the so called adiabatic "wet bulb" temperature $T^{(wb)}$ may be quantified

$$T^{(wb)} = T_\infty - \frac{\Delta h_v}{C_{v,c}} \, B_M \, . \tag{3.22}$$

Drag

If the particle surface velocity differs from the carrier phase velocity in the vicinity of the droplet, a boundary layer is formed at the particle surface, which results in shear forces tangential to the particle surface and momentum is exchanged between both phases. Additionally if the carrier phase is considered compressible, a local pressure maximum ahead of the particle and a local pressure minimum in the rear of the particle is formed. The surface integral of the carrier phase fluid forces acting on the particle surface may be represented by a net drag force

$\mathscr{F}_D$. If the particle surface is not spatially resolved (which is typically the case when applying the above mentioned point particle description of the dispersed phase), the net drag force

$$\mathscr{F}_D = \frac{1}{2} \rho_c \, C_D \, A_p \, |u_p - u_c| \, (u_p - u_c) \tag{3.23}$$

is estimated from experimental correlations incorporating e.g. a drag coefficient

$$C_D = \frac{\mathscr{F}_D}{\frac{1}{2} \rho_c \, u_{slip}^2 \, A_p} \tag{3.24}$$

which relates the effective drag force $\mathscr{F}_D$ acting on the particle to the dynamic pressure $p_{dyn} = \frac{1}{2} \rho_c \, u_{slip} \, A_p$ with the projected particle surface $A_p = \pi \, D_p^2/4$.
Stokes found that for creeping flow ($\mathrm{Re_p} < 1$), $C_D = \mathrm{Re_p}/24$. Schiller and Naumann [107] introduced the correlation correction factor f_{SN}

$$C_D = \frac{\mathrm{Re_p}}{24} \, f_{SN} \qquad \text{with} \qquad f_{SN} = 1 + 0.15 \, \mathrm{Re_p}^{0.687} \, . \tag{3.25}$$

From the net drag on an isolated (spherical) particle

$$\mathscr{F}_D^{(iso)} = 3\pi\mu_c \, D_p \, f_{SN} \, (u_p - u_c) \tag{3.26}$$

the total drag force per unit volume may be calculated (with the particle number density n_p and the particle mass per unit volume m_p)

$$\mathscr{F}_D = n_p \, \mathscr{F}_D^{(iso)} = m_p \, \frac{18 \, \mu_f \, f_{SN}}{\rho_p \, D_p^2} \, (u_p - u_c) \, . \tag{3.27}$$

The fraction in equation (3.27) characterizes a relaxation time

$$\tau_p = \frac{\rho_p \, D_p^2}{18 \, \mu_c \, f_{SN}} \tag{3.28}$$

for the relaxation of the velocity of an isolated particle in an undisturbed carrier phase environment

$$\frac{\partial u_p}{\partial t} = \frac{1}{\tau_p}(u_c - u_p) \, . \tag{3.29}$$

Turbulent dispersion

Turbulent fluctuations within the carrier phase cause small perturbations to the individual particle paths. As a consequence, sharp gradients in the dispersed phase concentration profile relax due to a mean (turbulent) diffusion flux.

In the present CFD model, this effect is modeled based on the Favre averaged inter-phase drag force [24] and depends on the momentum transfer (drag) coefficient C_D and the turbulent carrier phase Schmidt number Sc_c

$$\mathscr{F}_D^{(TD)} = C_D \frac{\nu_c}{Sc_c} \left(\frac{\nabla \alpha_p}{\alpha_p} - \frac{\nabla \alpha_c}{\alpha_c} \right) \, . \tag{3.30}$$

Viscosity

Based on kinetic theory for ideal gases it may be derived [8] that the dynamic viscosity of an ideal gas

$$\mu = \frac{1}{3} \lambda \, \bar{c} \, m \, n \tag{3.31}$$

is dependent on the molecule mass m, the molecular number density n, the mean free path between molecules λ and the velocity $\bar{c}$ characterizing the kinetic energy of the molecules[‡]. With increasing gas pressure, the mean free path λ decreases while the molecular number

---

[‡] Likewise, the thermal conductivity

$$\kappa_{th} = \frac{1}{3} \lambda \, \bar{c} \, C_v \, [A] \tag{3.32}$$

density *n* increases

$$\lambda \sim \frac{1}{p} \qquad \text{and} \qquad n \sim p \,. \tag{3.34}$$

As a consequence, the dynamic viscosity is independent of density to first order of accuracy [27]. By contrast, the mean kinetic energy and thus the dynamic viscosity is proportional to the gas temperature

$$\mu \sim T^{1/2} \tag{3.35}$$

which may also be obtained from the Sutherland formula

$$\frac{\mu}{\mu_0} = \frac{T_0 + C}{T + C} \left(\frac{T}{T_0} \right)^{\frac{3}{2}} \tag{3.36}$$

with the gas specific Sutherland constant *C* (which for air approximately is $C = 120\,\text{K}$).

3.1.4 CFD setup

The CFD model is validated based on measurements of the cold flow only so that the effect of evaporation is not included in the present CFD model.
Spatial velocity gradients in the vicinity of the dense spray are to be resolved so that consequentially a comparatively fine grid resolution is chosen. Because of the effects related to the statistical description of the Lagrangian dispersed phase description discussed in section 2.3, results from the Eulerian (two-fluid) method are predominantly pre-

---

depends on the heat capacity C_v and the molecular concentration $[A]$. In a similar fashion, the mass diffusivity

$$\mathscr{D} = \frac{1}{3} \lambda \, \bar{c} \tag{3.33}$$

is obtained.

sented in this section.

The standard Schiller-Naumann drag law [107] is applied. The shear stress transport model [88] is adopted to the carrier phase while the dispersed phase continuum is modeled to be laminar. The effect of turbulent fluctuations within the carrier phase on the mean transport of dispersed phase is neglected here[§].

Numerical settings

Because of the circumferential symmetry of the injector design, only a circumferential section of the full geometry is resolved. In comparison to the penetration length which is reached by the dispersed phase during injection, a large (cylindrical) geometry is assigned as glob-
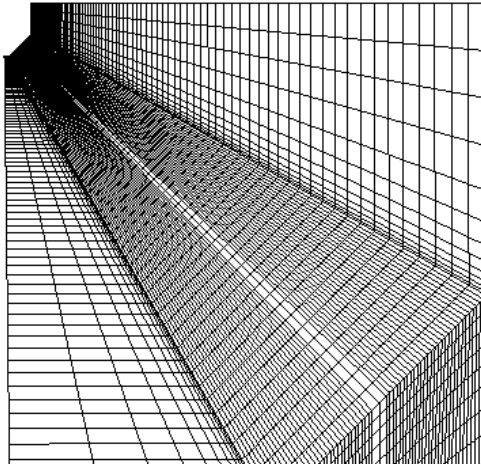
Figure 3.2: 2D axis-symmetric mesh topology

[§] The inclusion of turbulence effects acting on the dispersed phase – both the application of a dispersed phase turbulence model as well as a dispersed phase source term due to turbulent fluctuations within the carrier phase – is assessed in appendix 3.2.2.

ally bounding geometry (figure 3.2) so that an interaction between the chamber walls and the spray may be neglected.

Based on the Courant-Friedrichs-Levy criterion [63]

$$(\Delta t)_{CFL} = \text{CFL} \, \frac{(\Delta x)_{min}}{c_s} \, , \quad (3.37)$$

a time step for the baseline mesh quality of $\Delta t = 10^{-6}$ s is chosen.

Boundary and initial conditions

The CFD investigation is carried out using the commercially available CFD code Ansys CFX [5]. The applied numerical settings are listed in table 3.1.

Within the domain, the minimum volume fractions are $\alpha_p^{(min)} = 10^{-9}$ for the dispersed phase and $\alpha_c^{(min)} = 10^{-3}$ for the carrier phase respectively.

One major challenge in the context of CFD investigations is to prescribe adequate boundary conditions for the dispersed phase. Measurements of the particle characteristics (diameter and velocity) within the dense spray close to the injector are difficult to obtain and especially the overall effect of breakup in a dense spray environment (four-way coupling, see sec. 2.1) is not fully understood and subject to current research. For this reason, the application of a breakup model is

		Continuous	**Dispersed**
Volume fraction	–	$(1 - 10^{-9})$	10^{-9}
Velocity	m/s	0	0
Temperature	K	300	300
Turbulence degree	–	5%	–

Table 3.1: Initial conditions

discarded here and a representative mean droplet diameter is applied. For an approximate estimation of the droplet size distribution, the Malvern technique [82] yields reliable results up to certain maximum droplet number concentrations (maximum liquid volume fractions). For this reason, the droplet size spectrum close to the injector exit in general may not be measured. Only the size distribution at a location further downstream is accessible.

For a steady state operating condition (injection pressure $p_{inj} = 180\,\text{bar}$ and maximum injector opening), the particle size distribution of the modeled injector was measured at a distance 75 mm along injector axis [35]. Figure 3.3 shows the resulting discrete normalized distribution representing the normalized volume fraction of the corresponding size class (from here onwards referred to as the volume frequency [34]).

Particles of diameters between 10 and 20 μm represent approximately 60 % of the liquid volume. About 15 % of the liquid volume consists of particles larger than 20 μm and consequently about 20 % of the liquid volume is composed of particles of diameter smaller than 10 μm.

The second major input parameter to the CFD model is the velocity at which the liquid phase exits the injector outlet. Experimentally, this velocity may be evaluated from photographic images taken at the very beginning of the injection process (shortly after the injector opens). By contrast, it may not be measured when the injector is fully opened: At this flow condition, only the *apparent* spray front velocity is accessible from data obtained through photography.

The injector exit velocity may be approximated from the static mass flow rate $\dot{m}_{inj}$ which is supplied to the injector. Conservation of mass then yields (liquid density ρ_l, injector exit velocity v_{inj})

$$\dot{m}_{inj} = \rho_p\, A_{inj}\, v_{inj}. \tag{3.38}$$

In general, the effective cross section A_{inj} is smaller than the geomet-

ric cross section defined by the injector design. An outward opening injector is designed to inject the liquid as a liquid film. Due to the operating conditions (especially for small needle lifts and high injection pressures), the structure of the liquid phase close to the injector exit may differ considerably from a smooth liquid film. As a consequence of the injector internal flow and depending on the actual operating condition, the film is already heavily disturbed. Possible reasons are:

- separation of the injector internal flow from the injector walls and consequential formation of vortices rotating around an axis parallel to the main flow direction

- operation with gasoline: cavitation of light composites

Photographic images indeed suggest that such streaks are present depending on the operation condition.

To assume the effective cross section to be equal to the geometric cross section ($A_{inj} = A_{geo}$) thus yields an lower bound for the injector exit
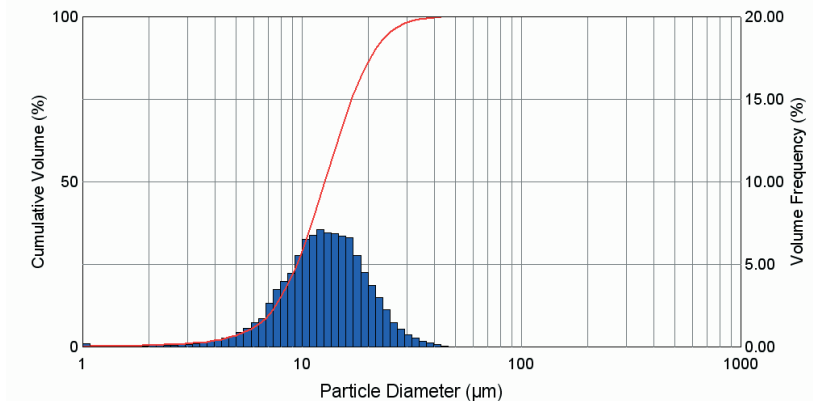
Figure 3.3: Particle diameter distribution, cumulated volume fraction (left axis, continuous line), volume frequency per particle size class (right axis, discrete bars) [35]

| Fuel density	kg/m^3	765
Mass flow rate	kg/s	$29 \cdot 10^{-3}$
Injection velocity	m/s	200
Droplet diameter	m	$15 \cdot 10^{-6}$

Table 3.2: Injection boundary condition

velocity.

On the other hand, the theoretical maximum velocity is obtained from the Bernoulli relation

$$p_0 = p_c + \frac{1}{2} \rho_p v_{inj}^2, \tag{3.39}$$

where p_0 and p_c are the static pressures in the injector reservoir and the pressure chamber into which the liquid is injected.

For the condition of maximum mass flow rate ($p_0 = 180$ bar, $p_c = 15$ bar, and maximum opening of 21 μm), the real *mean* velocity at the injector exit is bounded between

(Continuity) $165 \, m/s < v_{inj} < 207 \, m/s$ (Bernoulli) . (3.40)
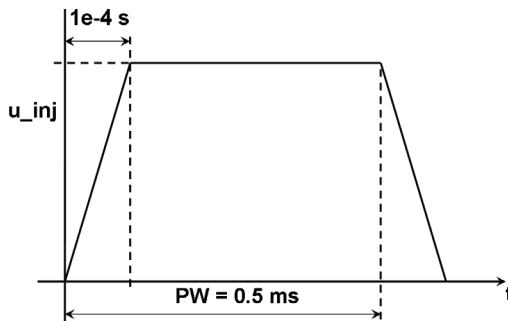
Figure 3.4: Injection profile

Based on the preceding assessment, the representative droplet diameter and injection velocity assigned to the dispersed phase are $D_p = 15\,\mu\text{m}$ and $v_{inj} = 200\,\text{m/s}$ unless indicated otherwise.

The mean mass flow rate through the injector is measured at steady state operating conditions. After "start of injection" (SOI), the injection profiles of both mass flow rate as well as injection velocity are modeled to increase linearly until the corresponding maximum values are reached within 0.1 ms. The injector driver signal ("pulse width" PW) causing the opening of the injector is 0.5 ms long. After this time, the injection is assumed to close in a similar fashion to the opening event, i.e. linearly within 0.1 ms.

3.2 Hollow cone injection induced two-phase flow

A CFD model of the hollow cone spray is employed in order to characterize the injection induced two-phase flow. On the basis of carrier phase velocity fields measured by means of PIV (section 3.2.1), exemplary results from the CFD model validation are given in section 3.2.2. The results from CFD investigation (subsequent sections) then focus on the characterization of the inter-phase momentum exchange and the injection induced carrier phase flow.

3.2.1 Experimental data

The most reliable way of validation of CFD models is to compare the solution to experimental data. The range of methods to generate data from experiments is discussed in the methodology section (section 2). For the present investigation, the carrier phase velocity field is compared to measurements applying particle image velocimetry (PIV).

Experimental data overview

This investigation utilizes data obtained from PIV measurements performed by Prosperi [97] on a constant pressure chamber. Different carrier phase pressures are investigated while the carrier phase temperature was set constant ($T_g = 300\,\mathrm{K}$) [¶]. The focus of the CFD investigation lies on comparatively short injection times to that only data resulting from injection pulse widths of $0.5\,\mathrm{ms}$ is considered. For the

---

[¶] For the mentioned measurement campaign, the focus lay on the interaction of the dispersed phase with "pure" air. Evaporation of liquid phase and the formation of air-fuel vapour mixture was deliberately suppressed. For this as well as for safety reasons, the experiments presented in the subsequent sections were carried out with a gas called CF4 which yields a larger density. The pressures referred to in this section (e.g. in table 3.3) indicate pressures air exhibits if charged to the density (and temperature) level at which the experiments with CF4 are carried out.

validation process, only statistical averages of the velocity are compared (i.e. turbulent fluctuations are not evaluated).

Particle image velocimetry

The particle image velocimetry (PIV) measurement technique provides access to carrier phase velocity fields by tracking the path of tracer particles through a plane which is defined by a laser sheet [34]. The tracer particles are considered to be very small so that their response time to alterations in the carrier flow field may be considered to tend towards zero (i.e. their Stokes number tends towards zero). If a tracer particle is located in the influence zone of the laser sheet, its surface reflects light. The reflections are recorded by a CCD camera with a fast exposure time at two consecutive times. The exposure time has to be much shorter than the characteristic time of the flow that is to be investigated. With the help of special software analyzing the digital data, the positions of individual particles are identified and allocated to one another on both images. Measuring the distance Δx_p one particle has traveled during the time span Δt between two subsequent exposures, the (mean) velocity of the particle at the investigated time (span) may be calculated ($v_p = \Delta x_p / \Delta t$). In the process of obtaining PIV data, multiple samples of the flow field tracer particles are recorded at a certain location area and during a certain time span. From this magnitude of data, both mean and fluctuating components of the velocity may be extracted.

Performing PIV measurements of the carrier phase during an injec-

p_g	T_g	PW	m_{inj}	t
6, 10, and 20 bar	300 K	0.5 ms	14.5 mg	0.3, 0.5, 0.8, and 1.0 ms

Table 3.3: Operating conditions of PIV measurement data utilized for CFD model validation [97]

tion process requires additional care: Due to the presence of liquid phase, the velocity field may not be measured at every location for two reasons: First, the intensity of the laser sheet may locally reduce to a level which does not produce a reliable signal intensity of the reflected light. Also, the intensity of the reflected light at the location of the CCD camera might fall below a certain limit due to the presence of liquid phase. Another effect special to PIV in gas-liquid flows is the fact that tracer particles may be attached to liquid phase elements during the injection process. In this case, obviously, the dispersed phase velocity is measured and not the carrier phase velocity in the vicinity of those elements.

For these reasons, the PIV data is revised while recording by the measurement software. Because the elemination of local velocity vectors was conducted in a less stringent manner originally, the data delivered by the measurement is still spurious to some extent due to the presence of not negligible concentrations of dispersed phase, especially close to
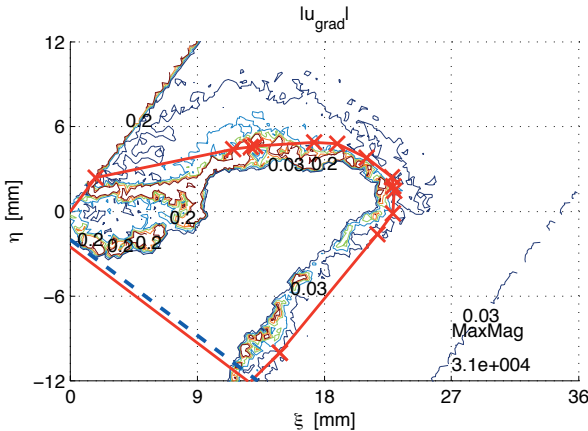
Figure 3.5: Carrier phase velocity gradient magnitude from experiment and prescribed filter contour, $p_{gas} = 10\,\text{bar}$, $t = 0.5\,\text{ms}$

the spray front region, where unphysical structures of the velocity profiles (high velocity gradients) were recorded. So for the present comparison, an additional revision of the PIV data was carried out based on the gray level of a corresponding Mie scattering image. From the Mie intensity isoline (figure 3.5), a convex structure is identified as the front of the dense spray zone.

Representation in conical coordinates

The usage of cone specific coordinates ξ and η (see section 2.4.1 and figure on page 61) is introduced in detail in appendix A. In order to shortly revise the data representation in conical coordinates, figure 3.6 displays normalized velocity vector fields from both experiment (on the left) and simulation (on the right). In the top row figures, the y-axis coincides with the injector axis where $y = 0$-line cuts the injector outlet at $x \approx 2.1$ mm. The diagonal dash-dotted line indicates the (presumed) dispersed phase cone jet center line.
In cone coordinates (bottom row figures), the ξ-axis corresponds to the spray cone center line and η is the coordinate normal to ξ. Positive values of η indicate the region outside and negative values the inside of the hollow cone. The diagonal dashed line now indicates the injector axis. In the following, conical coordinates are used, except indicated otherwise.

From figure 3.6 it becomes evident that the PIV measurement of the injection process only allows to access the carrier phase velocity field at locations comparatively far away from the dense spray zones (left hand side figures). Moreover, the velocity information in the region close to the injector outlet at $(\xi = 0,\ \eta = 0)$ is considered to be not reliable for $\eta \leq 0$ since at the displayed instant in time, liquid is still injected at full flow rate so that a good quality of the laser signal is not to be expected in this region (which is also supported by the fact that the experimental data does not yield a predominant flow direction in this region).

By contrast, detailed information on the flow behavior close to and inside the dense spray zone and consequently on the boundary conditions for the dispersed phase dynamics may be obtained form the validated CFD model (e.g. the right hand side plots in figure 3.6).

3.2.2 CFD model validation

Before the results of the CFD analysis are utilized for modeling purposes, the reliability of the solution has to be evaluated: The CFD
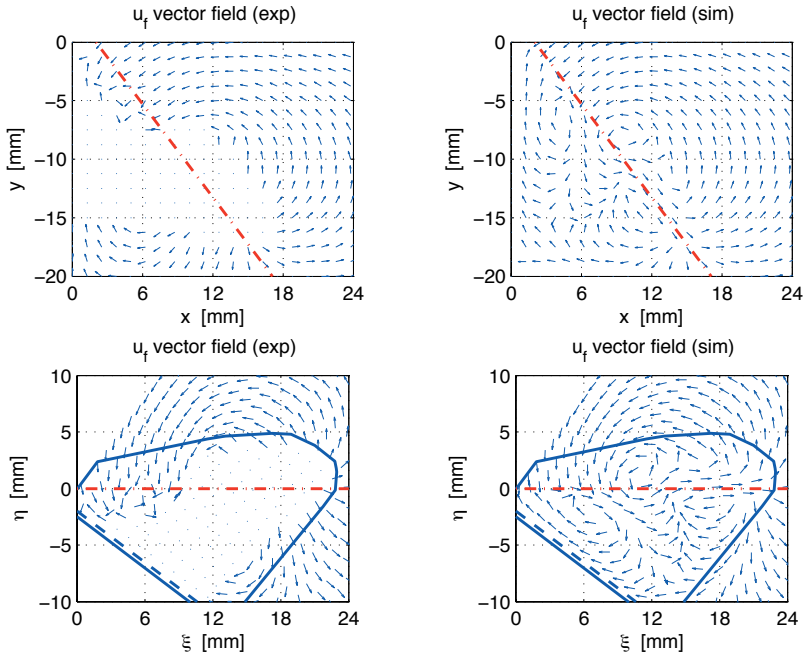
Figure 3.6: Comparison of carrier phase velocity fields, $p_{gas} = 10\,\text{bar}$, $t = 0.5\,\text{ms}$, velocity vector fields; cylinder coordinates (top), cone coordinates (bottom)

model has to be validated. The validation procedure has two main objectives: First, elements of the results obtained from CFD have to compare to data obtained in an alternate way – e.g. by means of an experiment (level of *accuracy* of the solution). Secondly, the response of the model to alterations in the input parameters has to be evaluated (*robustness* of the solution). For both validation criteria, levels of the desired solution quality have to be defined.

The experimental (PIV) data listed in table 3.3 is used for validation in two ways:
Because the spacial distribution of carrier phase momentum (or velocity) and its development over time characterizes the volume of carrier phase which is affected by the injection process, the comparison of the gas phase velocity field is applied as the primary indicator for the quality of the CFD model.
Since preceding the comparison, a spray front is identified from the PIV measurements (see figure 3.5), a penetration length of the dispersed phase into the pressure chamber may be compared.

As discussed in the methodology section, the focus of the CFD investigation lies on the usage of the Eulerian representation of the dispersed phase. Therefore, only results from this setup are presented here in order to quantitatively verify the injection induced carrier phase velocity field (*accuracy* validation). The sensitivity of the CFD solution to an altered dispersed phase representation (namely the Lagrangian formulation) and to changes in numerical parameters is examined in the subsequent sections (*robustness* validation).

Carrier phase velocity fields

In general, the comparison of experimental and simulated velocity data reveals a satisfactory quality of the CFD model. This impression is amplified by identical locations of the displayed vectors in both plots and their normalized representation. Because of this and the complexity of the vector data representation mentioned above, the two velocity

components are compared individually from here onwards.

The grid resolution of the simulation is orders of magnitude higher than the spatial resolution of the PIV measurement. Therefore the velocity resulting from CFD is examined at the locations where experimental data are available. (The high grid resolution of the CFD model makes an interpolation superfluous – the data is simply copied from the nearest neighbor location.) Isolines of velocity component magnitudes are depicted in figure 3.7. In order to emphasize the distance from the injector outlet into the pressure chamber along the main flow direction ξ at which carrier phase is set into motion due to the injection, the corresponding figures obtained from experiment and simulation are placed above each other.

The contours of the streamwise velocity component u (positive along the main flow direction ξ) as well as the cross-stream velocity component v (positive along the coordinate η normal to the main flow direction) both exhibit a comparatively good agreement. The four explicitly labeled contours $u = -3\,\text{m/s}$, $u = 1\,\text{m/s}$, $v = -5\,\text{m/s}$, and $v = 1\,\text{m/s}$ indicate that approximately the same volume of carrier phase mass is set into motion due to the injection process – both measured along and normal to the main injection direction. (Note that the straight diagonal lines in the figures resulting from the experiment do not indicate a flow pattern but stem from the choice of the measurement plane boundary.)

In summary, the temporal development both during (at 0.3 and $0.5\,\text{ms}$) and after injection (at 0.8 and $1.0\,\text{ms}$) match well over the whole chamber pressure range investigated here. Recall that two-phase flow sensitive input parameters to the CFD model such as particle diameter and maximum injection velocity are kept constant for varying time and chamber pressure. This result supports the reasoning presented in the context of the methodology section: To first order of accuracy, the superimposing effects of poly-dispersion, particle breakup and coalescence in volumes with high particle loading, and segregation of different size particles due to interaction with the (locally constant)

carrier phase velocity are negligible when studying the mean carrier phase flow field induced by the injection.

Spray penetration depth

A more compact representation of the CFD model accuracy based on experimental results is to investigate more integral flow quantities. For
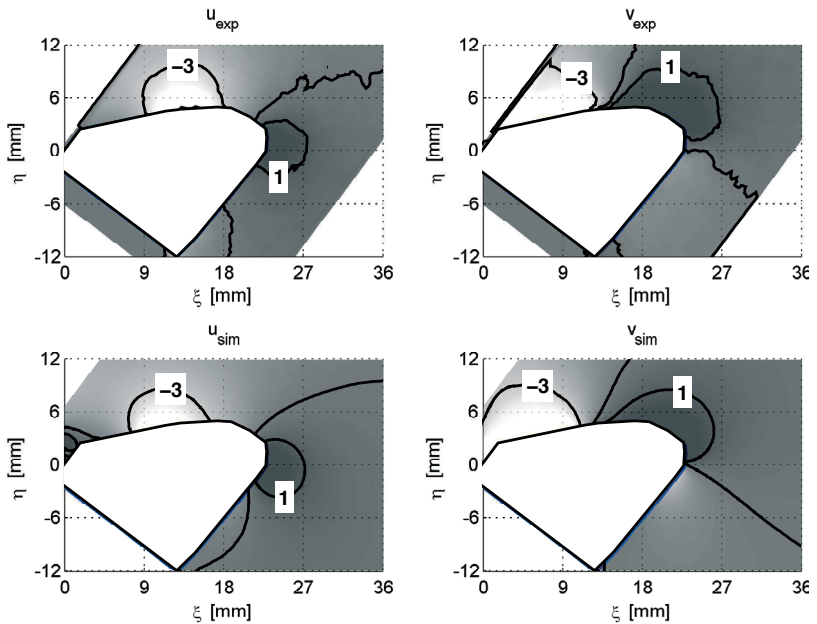
Figure 3.7: Comparison of carrier phase velocity fields, $p_{gas} = 10\,$bar, $t = 0.5\,$ms; results from experiment (top) [97] and CFD (bottom), streamwise velocity u (left) and cross-stream velocity v (right). In each plot one negative and one positive level is labeled – the contour line in between those levels corresponds to the zero level.

injection processes, the penetration depth of liquid phase and its temporal development is of special interest. It determines the carrier phase volume affected due to the injection process in two ways: First, with the *penetration depth* – the maximum distance of dispersed phase elements from the injector outlet *along* the main injection direction – obviously also the volume of carrier phase mass, which is directly influenced by the presence of dispersed phase, increases (as long as the carrier phase volume is a simply connected volume, i.e. the dispersed phase concentration distribution in space does not yield any carrier phase inclusions). In a similar fashion, more carrier phase volume is affected *normal* to the main injection direction (e.g. by shearing forces and consequential vortex formation) if the corresponding penetration depth is reached at earlier times.

The penetration depth *s* in figure 3.8 resulting from the PIV data is obtained by extracting a convex spray contour according to figure 3.5 and measuring its maximum distance from the origin ($\xi = 0$, $\eta = 0$). The corresponding values originating from simulation are obtained from the concentration contour of the dispersed phase volume fraction level $\alpha_p = 0.01$ (see e.g. the left plot in figure 3.10).
As suggested by the streamwise location of the carrier phase velocity components, also the inducing dispersed phase concentration distribution and respectively its maximum distance from the injection outlet (penetration depth) correspond well with experimental data.
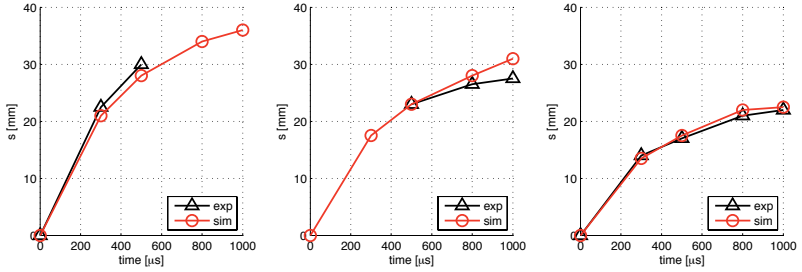
Sensitivity analysis

The sensitivity of the CFD model to changes of

- the dispersed phase representation,

- turbulence effects,

- numerical parameters (such as the resolution of the numerical grid and the temporal integration time step), as well as

Figure 3.8: Comparison of spray front penetration depth ξ at 6 (left), 10 (middle), and 20 bar chamber pressure (right)

- physical parameter (such as the mean droplet diameter and the mean injection velocity)

was assessed.

Because of their principal differences, the CFD solution of the two-phase flow induced by the hollow cone injection yields differences when the mathematical *description of the dispersed phase* is altered: The cross-stream width of the dispersed phase volume fraction field is more slender when the Lagrangian description is applied. The diffusive term in the Eulerian momentum equation (3.13) causes the dispersed phase volume fraction field to take on broader shapes than the Lagrangian results. The consequentially broader boundary layer thickness of the carrier phase jet causes smaller magnitudes of shear stresses, so that larger magnitudes of streamwise carrier phase velocity are obtained.

Because the total momentum (which is supplied to the flow domain by the injection boundary condition) needs to be conserved within the flow domain, increased carrier phase velocities correspond to smaller penetration depths of the dispersed phase mass: The total momentum carried by the carrier phase increases, while the total dispersed phase momentum within the flow domain decreases. Consequentially, the smaller velocity magnitudes resulting from the Lagrangian dispersed

phase representation correspond to a larger penetration depth of the liquid jet and vice versa.

The standard model coefficients of the carrier phase *turbulence model* were not changed in this investigation.

The application of a *turbulent dispersion force* generally leads to broader cross-stream profiles of the dispersed phase mass. As a consequence, the dispersed phase interacts with a larger volume (i.e. a larger amount of mass) of carrier phase and the penetration depth of the liquid jet decreases. The strong influence of this model indicates that the calibration of this sub-model is critical to the overall performance of the two-phase flow CFD model. Because the data available for the calibration of a mean turbulent dispersion force (both experimental and numerical) is limited in the case of a transient hollow cone flow resulting from high pressure injection as investigated here, the turbulent dispersion force model is omitted in the quantitative description presented in the remainder of section 3.2.

The presence of particles of finite Stokes number introduces additional disturbances to the carrier phase flow and thereby enhances the intensity of its turbulent fluctuations. The influence of a *turbulence enhancement* model [104] was found to be of minor influence in the context of the hollow cone injection. The production of turbulent kinetic energy, which is proportial to the square of the cross-stream velocity gradients within the carrier phase, exhibits much larger magnitudes than the turbulence enhancement source term which is proportional to the slip velocity.

Both the spatial and temporal resolution sensitivity was investigated. With increasing *mesh quality*, additional small scale vortex structures become visible as expected.

At the highest investigated spatial resolution, especially the Eulerian representation of the dispersed phase causes small scale artifacts in the dispersed phase volume fraction field, which are not physically plausible.

An important result from the sensitivity analysis of the mesh quality is that – for the set of investigated mesh qualities – the penetration depth of the dispersed phase jet is approximately independent from the resolution of the numerical grid: In the context of the Lagrangian description, increased dispersed phase volume fractions occur when the mesh quality is increased. But the cumulative effect of increased dispersed phase volume fractions on the local drag force does not change the global penetration depth. The cross-stream profiles of the dispersed phase volume fraction field resulting from the Eulerian description are more slender in shape when the mesh quality is increased while like in the Lagrangian case, the global penetration depth does not change with varying mesh quality. This result indicates that cross-stream gradients are sufficiently resolved even when the nominal mesh quality is decreased.

The CFD model result responds in a robust manner to variations in *time step size* which suggests that the chosen time step based on the CFL criterion at the injection boundary condition sufficiently resolves the flow dynamics.

The *number of computational parcels* employed for the Lagrangian description does not influence the global penetration behavior. When more computational parcels are tracked, slight differences in the front region of the two-phase jet may be observed.

Because of the square dependence of the drag force on the particle diameter, the flow solution responds rather sensitive to variations in particle diameter. The sensitivity of the flow to variations in the momentum which is supplied by the injection boundary condition (injection velocity) is found to have less influence than the particle diameter.

3.2.3 Inter-phase momentum exchange

The penetration behavior of the dispersed phase mass into the carrier phase environment depends on the momentum which is introduced to the flow via the boundary condition, i.e. the mass and momentum fluxes supplied by the injector. However with increasing distance from the injector outlet, the link between the momentum flux supplied at the boundary and the penetration behavior of the spray front within the domain becomes weaker. In the later flow condition, initial slip velocities have relaxed and secondary effects like the injection induced carrier phase flow dominate the propagation of the dispersed liquid.

One example for a two-phase flow condition which is primarily dominated by the injection boundary condition is the penetration behavior of an isolated particle into a gaseous carrier phase. With the definition of the particle relaxation time τ_p according to equation (3.28), the differential equation for the particle velocity (3.29) may be solved analytically to obtain the path of an isolated particle. If the carrier phase flow is not confined – i.e. a large carrier phase reservoir exists around the isolated particle – the carrier phase flow may be assumed to be not influenced by the presence of an isolated particle (one-way coupling,
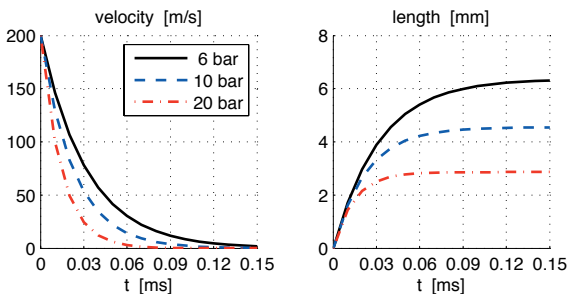
Figure 3.9: Isolated particle velocities (left) and particle paths (right) for different levels of gas pressure

$\frac{\partial u_c}{\partial t} = 0$). Then the particle velocity is

$$u_p(t) = u_p^{(0)} e^{-t/\tau_p} \tag{3.41}$$

and the particle path is described by

$$x_p(t) = u_p^{(0)} \tau_p \left(1 - e^{-t/\tau_p}\right) . \tag{3.42}$$

For the injection boundary conditions listed in table 3.2 (page 56), the analytical solution of isolated particle paths is presented in figure 3.9 for different values of gas pressure. An increased gas density (pressure) results in a faster decrease in particle velocity and consequentially a smaller penetration depth.

The comparison of individual particle paths with the penetration behavior of the spray front presented in figure 3.8 again illustrates that the movement of individual particles differs considerably from the dynamics within and at the front of a particle cloud: While individual particles initially travel at large velocities, they loose their momentum within a comparatively short distance from the injection outlet and yield a smaller penetration length than a spray front (cyclist effect).

The additional mechanisms occurring due to the injection of a dense particle cloud and due to the hollow cone geometry are discussed in detail in the methodology section (section 2.4). The two main aspects are:

- High dispersed phase volume fractions cause *two-way coupling* and the formation of a carrier phase boundary layer.

- Due to the hollow cone geometry, the carrier phase (boundary layer) flow is *not symmetrical* with respect to the dense spray sheet.

The momentum exchange between the gaseous carrier phase and the dispersed liquid is crucial for the estimation of the penetration behavior of the hollow cone spray into the gas phase. In order to model the

inter-phase exchange of momentum in an integral manner (see section 4), the evolution of the hollow cone spray in time and space has to be characterized. This characterization is presented in this section and answers the following guiding questions:

- How does the *injection induced carrier phase boundary layer* influence the penetration of dispersed phase into the gas phase (two-phase jet dynamics)?

- What is the effect of the *non-symmetry* on the hollow cone structure within the flow domain?

The characterization in this section is presented on the basis of sample results from the CFD model. Only results from the Eulerian dispersed phase representation are presented. A short summary is given at the end of the section.

Momentum exchange mechanism

The computed density fields of both dispersed phase volume fraction and streamwise momentum corresponding to a flow state during injection are presented in figure 3.10. Much like the volume density
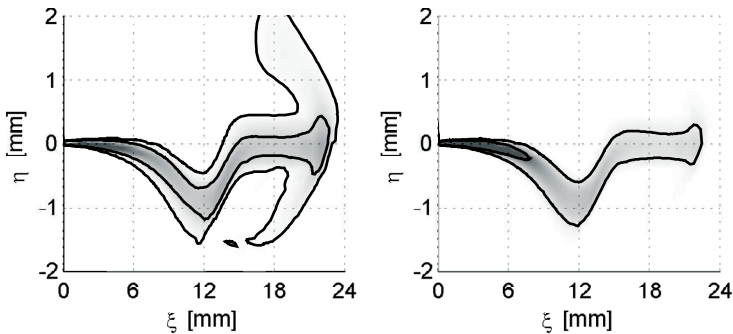
Figure 3.10: Dispersed phase volume fraction (left) and streamwise momentum (right); $p_{gas} = 10\,\text{bar}$, $t = 0.5\,\text{ms}$

field, the dispersed phase streamwise momentum density is highest in magnitude close to the injection outlet and decreases with increasing penetration depth (which in terms of conservation equations is due to the radial terms in equations (2.3) for mass and (2.4) for momentum). Because momentum is transfered from the dispersed towards the carrier phase, the velocity of the particles decreases with increasing distance from the injection outlet. As a consequence, dispersed phase mass and momentum accumulates within the flow domain. Because the injection boundary condition only introduces streamwise momentum to the system, the redirection of dispersed phase mass normal to the injection direction at the streamwise position around $\xi = 12\,$mm needs to be caused by the injection induced cross-stream movement of the carrier phase.

How is the cross-stream flux component of dispersed phase mass in the direction away from the hollow cone symmetry line $\eta = 0$ generated?
The carrier phase in the direct vicinity of the dense dispersed phase region (at $\eta \approx 0$ and especially close to the injection outlet) is strongly accelerated by the injected liquid. Due to the high bulk material density ratio ($\overline{\rho}_p/\overline{\rho}_c \gg 1$), the initially quiescent gas should be accelerated almost instantaneously to the dispersed phase velocity (initial slip velocities should reduce almost instantaneously). This is not the case even when the flow is in equilibrium conditions such as at the time 0.5 ms after begin of injection in the region close to the injector (figure 3.11). Instead, a non-negligible amount of slip velocity is maintained within the flow domain: Between the first two streamwise positions (at $\xi = 3$ and $\xi = 6\,$mm), the maximum streamwise slip velocity even rises with increasing streamwise position.
High slip velocities are maintained within the flow domain because adjacent to the dense spray regions, a *carrier phase boundary layer* is induced. Opposed to single phase jet profiles, the streamwise carrier phase velocity (figure 3.12) does not yield an s-shape profile in

either direction from the jet center position (the location where the maximum velocity is reached). By contrast, the profile – especially at $\xi = 3\,\text{mm}$ – exposes more similarity with a "moving wall" boundary layer where the center velocity is imposed by the no-slip condition at the wall. The consequential shear stresses counteract the acceleration of gas phase mass due to drag. Also, the (limited) acceleration of carrier phase mass induced by drag causes entrainment towards the dense spray zone. In order to emphasize the fact that this entraining mass flux stems from drag with the injected liquid, it is referred to as *excess entrainment*. This drag induced entrainment again leads to smaller
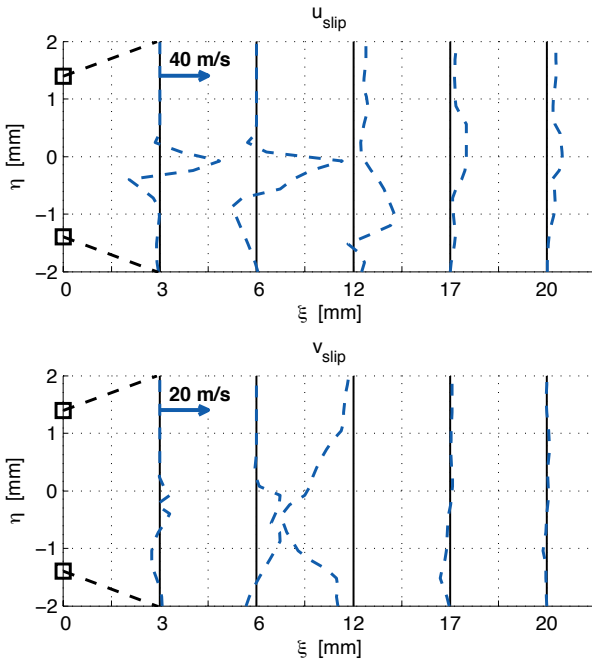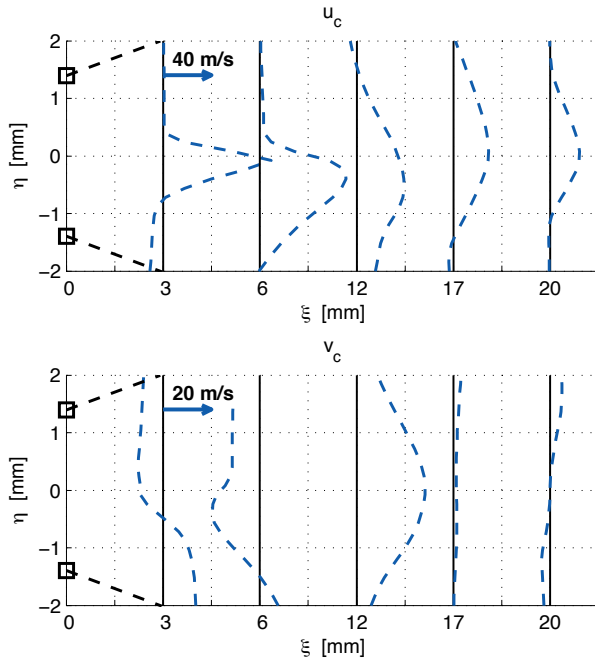

Figure 3.11: Slip velocity $u_{slip} = u_p - u_c$, streamwise (top) and cross-stream components (bottom); $p_{gas} = 10\,\text{bar}$, $t = 0.5\,\text{ms}$

widths of the boundary layer profiles.

The resulting forces of drag and shear locally form an equilibrium. It determines the locally maintained slip velocity and thus the amount of momentum which is transferred between both phases.

To first order of accuracy, the diffusive transport of carrier phase momentum away from the dense spray zone depends only on the cross-stream velocity gradient and is independent from the size of the area normal to the diffusion flux (here the area of the hollow cone sheet). Because outside of the hollow cone sheet, a larger area is available for both diffusion and entrainment, also a larger amount of carrier phase


Figure 3.12: Carrier phase velocity, streamwise (top) and cross-stream components (bottom); $p_{gas} = 10\,\text{bar}$, $t = 0.5\,\text{ms}$

mass is affected by the two-phase jet at the outside of the hollow cone sheet. As a consequence, the larger portion of gas phase mass which is entrained into the two-phase jet due to drag stems from the outside of the hollow cone. The thereby induced larger carrier phase momentum flux towards the dense spray zone from the outside of the hollow cone redirects both the carrier phase boundary layer and the dispersed phase mass towards the inside of the hollow cone (figure 3.10). This gives the reason for the non-symmetry of the hollow cone two-phase flow with respect to the hollow cone sheet.

In general, the dispersed phase mass and momentum density profiles
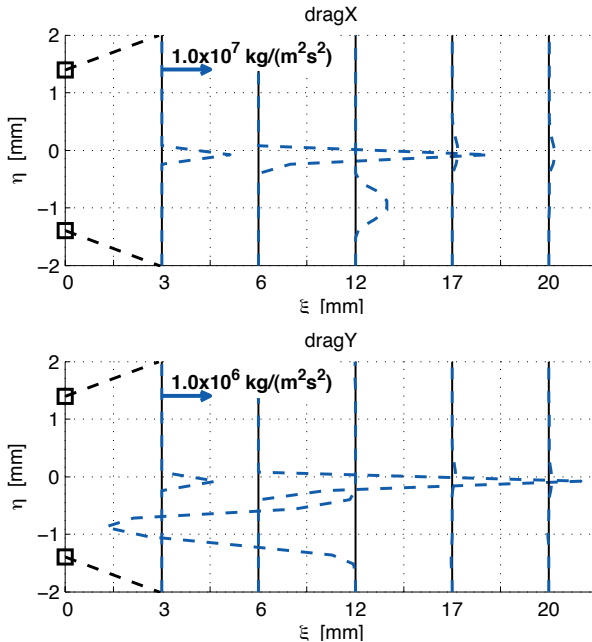
Figure 3.13: Inter-phase drag force, streamwise (top) and cross-stream components (bottom); $p_{gas} = 10$ bar, $t = 0.5$ ms

are more slender than the ones of the carrier phase. Nevertheless, also the dispersed phase cross-stream profiles become broader with increasing penetration due to momentum diffusion (figure 3.10). Consequentially, the cross-stream width which is occupied by high dispersed phase momentum densities and which is available for inter-phase momentum exchange increases with increasing penetration depth. Within broader dense spray zones, also higher maximum streamwise slip velocities occur (figure 3.11) and as a consequence, drag forces of higher magnitude are exchanged (3.13 at $\xi = 6$ versus $\xi = 3$ mm).

From figure 3.13, the dominance of the injection direction is clearly visible at the first two streamwise positions: The streamwise drag force component is one order of magnitude higher than its cross-stream component. At $\xi = 12$ mm by contrast, both components are of the same order of magnitude. This indicates that from this position onwards in the downstream direction, the two-phase jet may be characterized as a homogeneous mixture with regards to the momentum equation. The kinematic mixture property of the downstream flow is also supported by the face that the streamwise carrier phase velocity profile displays a typical jet shape, which is not deformed by injection induced drag.

Temporal evolution

In order to characterize the temporal evolution of the inter-phase momentum exchange in more detail, profiles extracted from the presumed spray center line ($\eta = 0$) at two instances in time $t = 0.3$ and $t = 0.5$ ms are investigated.

The almost identical profiles indicate that the flow is in a steady state condition while the injection is in progress (figure 3.14). The dispersed phase momentum maintained within the domain decreases with increasing distance from the momentum supply position (the injector exit). The intermediate drop of the dispersed phase velocity (e.g. for $8 < \xi < 11$ mm at $t = 0.5$ ms) and the subsequent rise of the carrier

phase velocity at the centerline are caused by the redirection of the jet normal to the main injection direction due to the non-symmetrical entrainment (see the dispersed phase mass and momentum concentration contours in figure 3.10).

Altogether, the dispersed phase centerline profiles exhibit a strong decrease in both momentum and velocity along the injection direction close to the injection outlet. This is due to the radial widening of the hollow cone. In spite of the injection induced carrier phase cross-flow it may be concluded from figure 3.14 in combination with figure 3.10, that the cross-stream maximum of the dispersed phase velocity adopts a streamwise profile of the shape $u_p^{(center)} \sim 1/\xi$ (which is in accordance to the preliminary characterization in section 2.4).

In figure 3.15, the previously described dynamics of the inter-phase momentum exchange is presented with the focus on the temporal de-
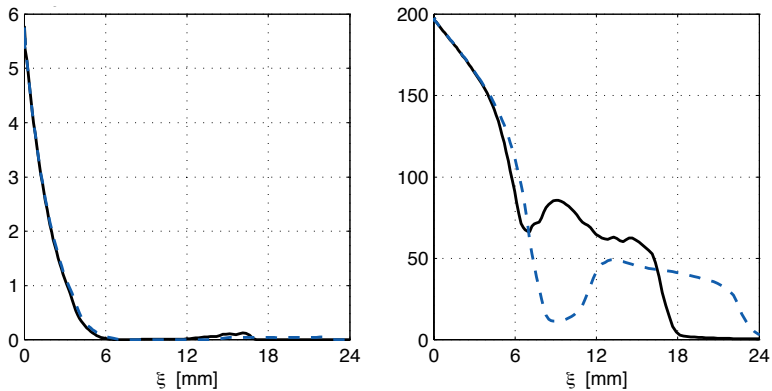
Figure 3.14: Dispersed phase centerline profiles during injection; streamwise momentum density $(\overline{\rho}_p u_p)$ (left) and streamwise velocity u_p (right); $p_{gas} = 10\,\text{bar}$, $t = 0.3\,\text{ms}$ (cont. line) and $0.5\,\text{ms}$ (dashed line)
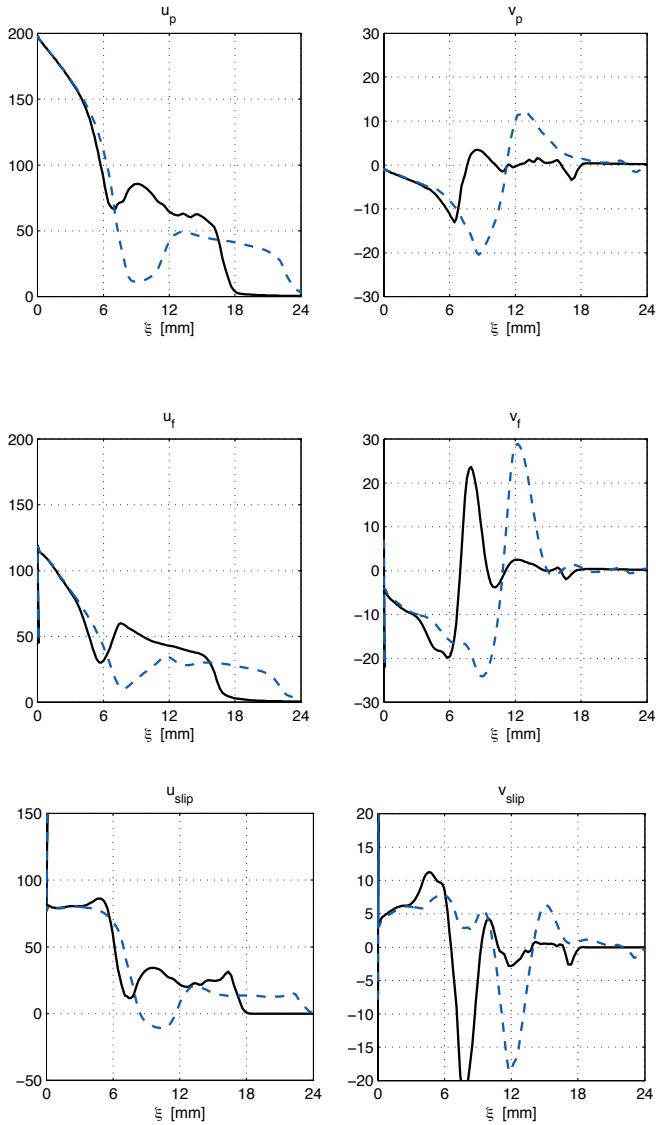
Figure 3.15: Centerline velocities, streamwise *u* and cross-stream components *v* of dispersed (index "p") and carrier phase (index "f") and slip velocity; $p_{gas} = 10$ bar, $t = 0.3$ ms (cont. line) and 0.5 ms (dashed line)

velopment: The velocities of both the dispersed and carrier phase velocities as well as the slip velocity – the excess velocity of the dispersed over the carrier phase's – are displayed for two instances in time during injection. In the region of high dispersed phase momentum density close to the injector ($\xi < 6\,$mm), a steady state is reached already at $t = 0.3\,$ms. In spite of the high material density ratio $\rho_p/\rho_f \approx 100$, the carrier phase close to the injector is not accelerated at once but a significant slip velocity (of about $u_{slip} = 80\,$m/s at an injection speed of u_{inj} $200\,$m/s) is maintained. The carrier phase cross-stream velocity indicates a vortex which is induced by the injection process. The vortex center is redirected downstream. The induced carrier phase vortex again causes the dispersed phase field to rotate.

Orders of magnitude

The drag force results from the inter-phase slip velocity. The resulting acceleration of both phases depends on the respective bulk densities: Due to its comparatively low bulk density, the gaseous carrier phase experiences a larger acceleration within the dense spray zone than the dispersed phase. The radial widening of the hollow cone jet with increasing penetration depth leads to a decrease in mass and momentum density of the dispersed phase. The deceleration of liquid phase due to drag leads to a local accumulation of dispersed phase mass (and

Equation component	**Carrier-** stream- wise	**phase** cross- stream	**Dispersed** stream- wise	**phase** cross- stream
Bulk mass density	$\mathscr{O}\left(\bar{\rho}u\right) = \mathbf{3}$	$\mathscr{O}\left(\bar{\rho}v\right) = 2$	$\mathscr{O}\left(\bar{\rho}u\right) = \mathbf{4}$	$\mathscr{O}\left(\bar{\rho}v\right) = 2$
Streamwise mom.	$\mathscr{O}\left(\bar{\rho}u^2\right) = \mathbf{5}$	$\mathscr{O}\left(\bar{\rho}uv\right) = 4$	$\mathscr{O}\left(\bar{\rho}u^2\right) = \mathbf{6}$	$\mathscr{O}\left(\bar{\rho}uv\right) = 4$
Cross-stream mom.	$\mathscr{O}\left(\bar{\rho}uv\right) = 4$	$\mathscr{O}\left(\bar{\rho}v^2\right) = 4$	$\mathscr{O}\left(\bar{\rho}uv\right) = 4$	$\mathscr{O}\left(\bar{\rho}v^2\right) = 4$

Table 3.4: Mass and momentum bulk density fluxes during injection; $p_{gas} = 10\,$bar, $t = 0.5\,$ms; characteristic orders of magnitude

thus momentum) and thereby compensates the rarefaction due to the radial widening: Even though spatially dispersed, the bulk momentum density of the liquid droplets within the dense spray zone is one order of magnitude higher than the carrier phase (bulk) density during the forcing period (i.e. while injection proceeds, see table 3.4).

Also in preparation of the derivation of a simplified model for the hollow cone penetration behavior it is helpful to compare fluxes occuring in the individual conservation equations of mass and momentum with respect to their orders of magnitude. The overview over the fluxes of mass and momentum equations is given in table 3.4. The comparison reflects the dominance of the streamwise over the cross-stream components and among them the dispersed phase over the carrier phase fluxes: For example in the carrier phase streamwise momentum equation, the streamwise component ($\mathcal{O}\left(\overline{\rho}u^2\right) = 5$) dominates the cross-stream component ($\mathcal{O}\left(\overline{\rho}uv\right) = 4$).

By contrast, the fluxes of cross-stream momentum (last row in table 3.4) are of the same order of magnitude for both phases and both components.

The contributions of the *gradients* of the fluxes within the individual conservation equations are contrasted in section 3.2.5.

3.2.4 Carrier phase transport

The injection of dispersed liquid into a gas pressure chamber constitutes a spatially distributed source of momentum to the carrier phase gas. Comparing the carrier phase velocity (figure 3.12) with its corresponding momentum distribution (figure 3.16) reveals that with regards to the carrier phase, compressibility effects – both due to compression of the carrier phase itself as well as due to bulk effects (carrier phase mass rarefaction resulting from increased dispersed phase mass concentration) – play a minor role in the present flow configuration.

Shear stresses

During injection, the acceleration of the carrier phase within the dense spray zone is limited by the viscous momentum transport within the gas phase (see e.g. figure 3.15). As a result, the cross-stream profiles of the streamwise carrier phase momentum yield a "moving wall" type shape close to the injector (e.g. at $\xi = 3$ and $\xi = 6\,\text{mm}$ in figure 3.16). This is explained in detail in section 3.2.3.
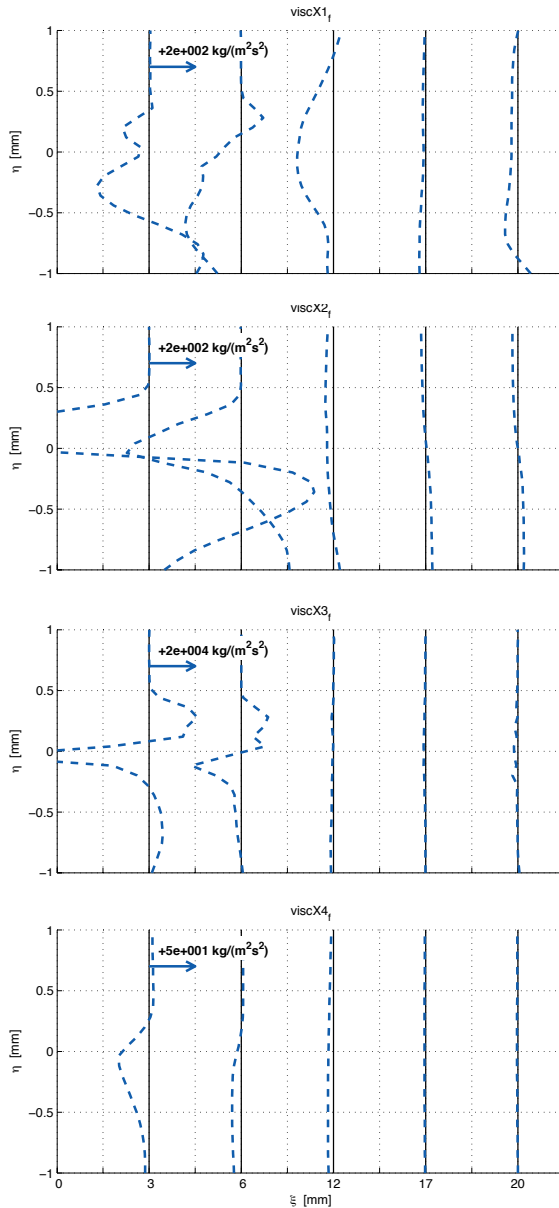
With regards to modeling, the dominant terms among the viscous ones
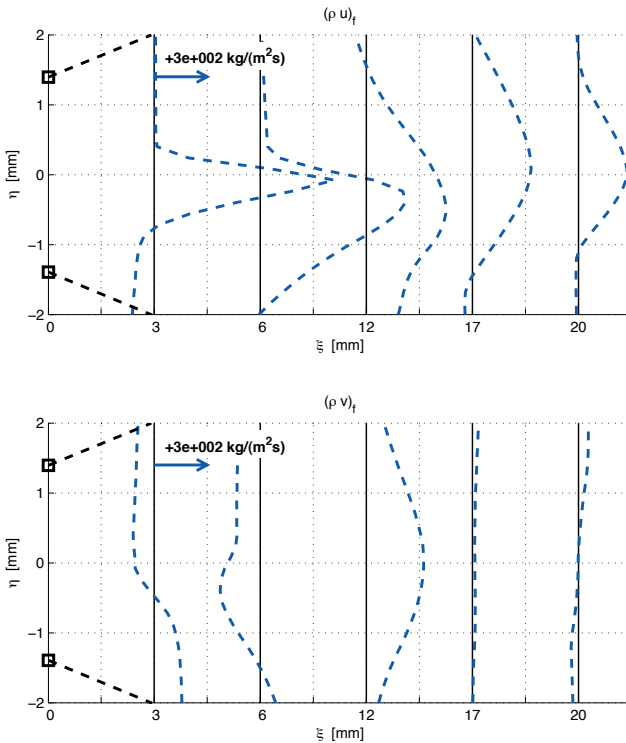
**Figure 3.16:** Carrier phase momentum distribution

Figure 3.17: Carrier phase viscous terms *viscX*1 (top), *viscX*2 (upper center), *viscX*3 (lower center), and *viscX*4 (bottom); $p_{gas} = 10$ bar and $t = 0.5$ ms

have to be determined. The preliminary assessment of the hollow cone flow in section 2.4.1 revealed the term incorporating the second cross-stream gradient $\frac{\partial^2 (*)}{\partial \eta^2}$ to be dominant. For the streamwise carrier phase momentum conservation equation, this corresponds to the term $viscX3$ ($\frac{\partial^2 u_f}{\partial \eta^2}$) in figure 3.17 [||]. It is strong on either side of the jet in the region of massive carrier phase entrainment (e.g. in figure 3.17 at $\xi = 3$ mm and $\xi = 6$ mm). Second in magnitude is the term $viscX2$ due to the first cross-stream gradient $\frac{\partial u_f}{\partial \eta}$. Due to the square exponent of the radial distance from the symmetry axis ($r = \xi \, \sin\theta + \eta \, \cos\theta$) in the denominator of equations (2.4) and (2.5), the fourth viscous term in general is negligible (except for locations very close to the symmetry
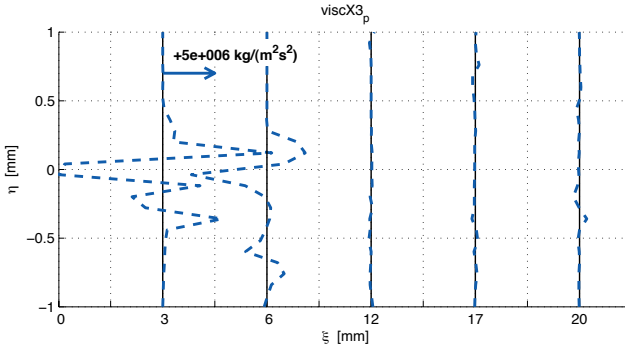
Figure 3.18: Dispersed phase viscous term $viscX3$; $p_{gas} = 10 \, \text{bar}$ and $t = 0.5 \, \text{ms}$

[||] Due to software restrictions, the terms are not obtained from the solver directly. Instead, the second order derivatives are recalculated by means of centered finite differences of second order of accuracy mapping the unstructured data onto a structured grid. The structured grid is of coarser quality than the unstructured grid so that the magnitudes resulting from the finite differences depend on the structured grid resolution. The magnitudes referenced in this section stem from a grid with spatial resolution $\Delta x = 83 \mu m$.

axis).

In the context of the Eulerian continuum representation, a viscous momentum diffusion is assigned also to the dispersed phase. For the carrier phase state referred to in figure 3.17 (p = 10 bar, t = 0.5 ms), profiles of the the third viscous term of the dispersed phase are presented in figure 3.18 in order to illustrate the volume affected by the dispersed phase shear force during the injection process. The viscous terms of the dispersed phase are larger in magnitude than those of the carrier phase, but their profiles exhibit a more narrow cross-stream width.

Vortex formation

The two-phase jet is spatially confined: Inside the hollow cone, the flow is restricted by the injector symmetry axis. At the outside of the hollow cone sheet, both the injector walls (in the region close to the injection boundary condition) and the pressure chamber walls (at the streamwise positions further away from the injector outlet) delimit the two-phase flow induced by the injection. As a consequence, a back-flow compensates downstream carrier phase movement in the dense spray zone. Between the back-flow and the carrier phase boundary layers on either side of the hollow cone sheet, carrier phase vortices are induced. Due to the non-symmetrical carrier phase flow pattern, the vortex structure is also non-symmetric with respect to the hollow cone sheet.

The characterization of the carrier phase vortex structure is of multiple importance: The location and strength of the shear induced vortices influence the carrier phase velocity as boundary condition to drag with the dispersed phase elements and to possible breakup mechanisms due to velocity differences between the two phases. The necessity of vortex characterization becomes even more obvious when the evaporation of the liquid phase is investigated: The convective transport of carrier phase mass between the dense spray zone and the regions of fresh air further away from the dense spray zone heavily influences the quality of the local evaporation environment (gas composition) at the surface of liquid phase elements. It thus dominates the diffusive transport of heat towards and air-fuel mixture away from droplets positioned close to vortices and thus accelerates the evaporation process.

The identification and characterization of a vortex is a challenging task. Based on the field of carrier phase vorticity

$$\omega = \nabla \times u \qquad (3.43)$$

(which in two dimensions is a scalar $\omega = \frac{\partial v}{\partial x} - \frac{\partial u}{\partial y}$), vorticity is induced

in shear layers. The local (macroscopic) accumulation of rotating fluid elements (microscopic vorticity) leads to the formation of a vortex (if the formation is not restricted, e.g. by the channel geometry in Couette flow).

The vorticity field resulting from the present flow configuration exhibits a rather complex structure (figure 3.19). On either side of the dense spray zone, vortices are formed. Due to the continuing momentum supply within the dense spray zone during injection as well as due to the carrier phase entrainment, vortices are strained in the main injection direction. Due to the injection induced global downstream movement of the flow structure, also the vortices are redirected downstream in the course of the injection. If a certain length of the vortex (identified by the region of high vorticity concentration around a point of maximum vorticity magnitude) is exceeded, the vortex separates into a part which travels further downstream and a part which stays connected to the region of highest velocity gradients close to the injector outlet.
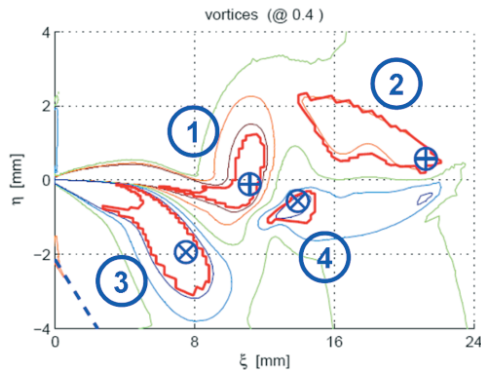
Figure 3.19: Carrier phase vorticity field isolines and vortex contours; $p_{gas} = 10\,\text{bar}$ and $t = 0.5\,\text{ms}$

In general it is not trivial to locate the position of a vortex. Reliable re-
sults have been obtained with vortex criteria like the Q-criterion [67]
(first introduced by [64]). Because in the present investigation, in-
formation about the rotational direction of the vortex movement is
sought, the intensity of local vorticity was adopted to quantitatively
describe vortex contours and the contained strength. In figure 3.19,
vortex contours are obtained by locating a local extremum of vorticity
(with a mathematically positive sense of rotation identified by a "+"
sign in a circle, and a negative sense of rotation indicated by an "x"
sign inside a circle). Two vortices on either side of the dense spray
zone are characterized where the indices "1" and "2" label the two
vortices outside the hollow cone and "3" and "4" identify the corre-
sponding vortices inside the hollow cone. From the extrema location, a
simply connected contour is defined to be bounded by elements which
still carry 40% of the extremal vorticity. This procedure in generally
leads to non-convex contour lines, especially close to the location of
momentum supply (the injection outlet) where the strong inter-phase
momentum exchange and the consequential shear and strong entrain-
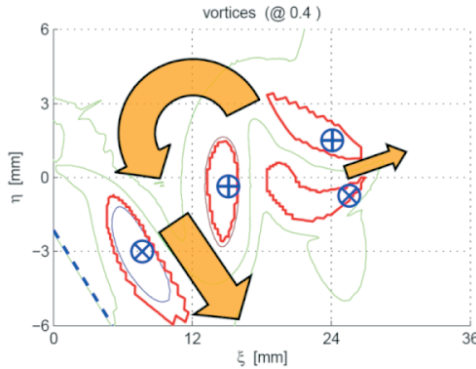
Figure 3.20: Late carrier phase vortex system at $t = 0.8\,\mathrm{ms}$ and $p_{gas} = 10\,\mathrm{bar}$
("vortex induced secondary jet")

ing mass flux prevent the vortex fluid elements from rearranging in the most compact form, namely a circular cross-section, corresponding to a torus shape.

An elaborate characterization of the vortex system induced by the hollow cone injection has been conducted. The investigation reveals that the vortex at the outside of the hollow cone at the downstream position (number "2" in figure 3.19) exhibits the greatest cross-section. It acquires a greater amount of rotational energy from the injection carrier phase flow in the streamwise direction during injection than the other vortices.

After end of injection, the total flow is dominated by the energy contained in this vortex: Its (in figure 3.19 counter-clockwise) sense of rotation causes vortex "1" to move in between the vortex pair originating from the inside of the hollow cone (figure 3.20). Each of the two induced vortex pairs causes an ejection of material present between each pair: A smaller ejection flow is caused in the original injection direction while a stronger ejection flow is induced in the direction parallel to the injector axis. The later explains why in comparatively cold conditions (limited evaporation), a cloud of liquid droplets is ejected from the inside of the hollow cone along the injector axis shortly after end of injection.

3.2.5 Temporal evolution

In the previous two sections, the mechanism of momentum transfer from the injected to the carrier phase as well as the induced carrier phase boundary layer and resulting vortex system was discussed. In a simplified but fast model, as it is aimed for in this work (section 4), details of the three-dimensional formulation need to be dropped so that dominant effects (manifesting in dominant conservation equation terms) may be identified.

In general, the fields representing individual conservation equation terms exhibit a more complex structure than the fields of the conserved variables themselves because, not only the conserved variables, but also their spatial gradients are involved (see e.g. figure 3.21).

A space integral information on a given flow field is the maximum order of magnitude occurring within the field (as specified for the plots in figure 3.21 in their lower right corner). Because of the strong coupling of the velocity components by the local pressure term, maximum fluxes of both main velocity components (along ξ and η) generally emerge at similar locations in space. As a consequence, the extraction of maximum terms characterizes approximately the same location in space while this location may change over time.

The two-phase flow depends strongly on the injection boundary condition applied. For this reason, the distinction between the forced system (flow states during injection) and the free system (flow states after injection) is again applied in the following.
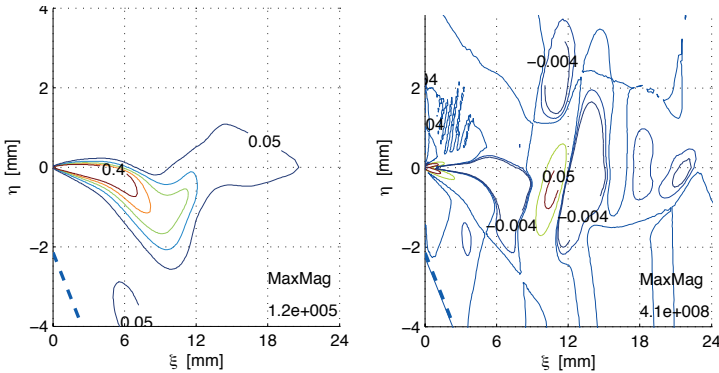
Figure 3.21: Conserved variable $(\overline{\rho}_c u_c^2)$ (left) and the resulting flux gradient $\frac{\partial(\overline{\rho}_c u_c^2)}{\partial \xi}$ in conservation equation (2.3) (right); at $p_{gas} = 10\,\text{bar}$ and $t = 0.5\,\text{ms}$ (forced system)

Forced system

In tables 3.5 and 3.6, orders of magnitudes of the conservation equations of mass (eq. (2.3)) and both streamwise (eq. (2.4)) and cross-stream momentum (eq. (2.5)) are listed. The columns correspond the the individual term within each equation.

During injection, the terms of the streamwise momentum equations dominate the ones of the conservation equation for cross-stream mo-

	eq.	stream-wise	cross-stream	radial	drag force
Continuity	(2.3)	6	6	5	-
Stream-wise mom.	(2.4)	8	**9**	8	8
Cross-stream mom.	(2.5)	7	7	7	7

(a) Dispersed phase terms

	eq.	stream-wise	cross-stream	radial	drag force
Continuity	(2.3)	5	**6**	5	-
Stream-wise mom.	(2.4)	7	**8**	7	**8**
Cross-stream mom.	(2.5)	7	7	6	7

(b) Carrier phase non-viscous terms

	eq.	visc1	visc2	visc3	visc4
Stream-wise mom.	(2.4)	2	3	**4**	2
Cross-stream mom.	(2.5)	2	2	**3**	2

(c) Carrier phase viscous terms

Table 3.5: Conservation equation contributions; orders of magnitude; forced system

mentum. This applies to both phases and corresponds to the momentum fluxes listed earlier (see table 3.4).

The terms contributing to the streamwise momentum conservation of dispersed phase are of comparable orders of magnitude. Only the cross-stream flux is slightly increased because within the term $\frac{\partial(\bar{\rho}_p\, u_p\, v_p)}{\partial \eta}$, the dispersed phase volume fraction cross-stream gradient $\frac{\partial \alpha_p}{\partial \eta}$ is large.

For the carrier phase streamwise momentum equation, the cross-stream term (i.e. the term containing the cross-stream gradient) dominates which supports the preliminary investigation in section 2.4.1.
The dominance of the cross-stream gradients in carrier phase conservation equations of both streamwise momentum and continuity reflects the effect of excess entrainment which is induced by drag with the dispersed phase: The drag force and the cross-stream gradient in the streamwise carrier phase momentum equation are of the same order.

During the total of the injection period, the terms accounting for the radial widening of the two-phase jet are non-negligible but about one order of magnitude smaller than the streamwise and cross-stream contributions.

Due to the large cross-stream gradients appearing in the streamwise momentum equation, a strong shear force is induced. Unfortunately, the solver does not provide direct access to the second order spatial gradient of each velocity component in the result files, so that it is calculated in a post-processing step. For this reason, the velocity components are first projected onto a equidistant mesh which is coarser than the computational mesh on which CFD results are available ($\Delta x = 83 \mu m$). In a second step, the second spatial gradient (of first order of accuracy) is calculated and the viscous terms are composed. Note that because of the projection procedure, the orders of magnitude obtained for the viscous terms (table 3.22c) are only comparable among themselves but not to the fluxes presented above.

	eq.	stream-wise	cross-stream	radial	drag force
Continuity	(2.3)	5	5	4	-
Stream-wise mom.	(2.4)	6	6	5	5
Cross-stream mom.	(2.5)	6	6	5	5

Table 3.6: Carrier and dispersed phase conservation equation contributions; orders of magnitude; free system

Among the carrier phase viscous terms, the third term incorporating the second order cross-stream gradients $\frac{\partial^2 \hat{u}}{\partial \eta^2}$ and $\frac{\partial^2 \hat{v}}{\partial \eta^2}$ provide the strongest contributions. The maximum viscous shear term appears in the streamwise momentum conservation equation which again agrees with the findings in section 2.4.1.

Free system

After injection has ended, the conservation equation terms are generally one order of magnitude smaller. A dominant flux direction is not observable anymore. In comparison to the forced system, the viscous terms are negligible. Although no additional momentum is supplied to the system, the inter-phase drag force is only one order of magnitude smaller than the momentum equation fluxes.

3.3 Summary

A CFD model of the two-phase flow for a hollow cone injection process has been validated based on carrier phase velocity field measurements (PIV) and global spray front propagation over time. Its sensitivity both to physical and numerical characteristics has been assessed and has been found to support the validity of the model results presented here.

The effect of spatially distributed acceleration of gas phase due to the injection of liquid fuel has been studied. The inter-phase momentum exchange due to the injection of a dispersed liquid phase into a gaseous carrier phase exhibits fundamentally different dynamics than a single phase jet in the region close to the injection boundary condition. In the dense spray zones, the injected liquid causes a strong acceleration of carrier phase mass. The streamwise acceleration of gas locally causes additional ("excess") entrainment in regions of high momentum fluxes within the dispersed phase, i.e. close to the injection outlet. The later causes the width of the local boundary layer thickness to decrease thereby increasing momentum diffusion normal to the injection direction. The induced boundary layer in the carrier phase counteracts the acceleration due to drag so that considerable magnitudes of slip velocity are maintained within the flow domain.

A secondary carrier phase flow pattern is induced by the injection. Due to the hollow cone geometry, it is not symmetric with respect to the hollow cone sheet. It causes a redirection of the dispersed phase normal to the main injection direction and thereby induces a non-symmetric vortex system around the liquid sheet.

During injection, two main region are observed within the dispersed phase: Near the injection outlet, the flow is in steady state conditions. The spray front, by contrast, is influenced by the secondary flow pattern within the carrier phase.

In order to support the modeling steps taken in the following section, the maximum occurring orders of magnitude corresponding to the field of the conservation equation terms were analyzed. The terms of the streamwise momentum equation dominate those of the cross-stream momentum equation. Among the convective and the viscous fluxes within the streamwise momentum equations, the cross-stream components are larger in magnitude than the streamwise terms for both phases.

4 Integral modeling

In this section, major features of the hollow cone two-phase jet elucidated in the previous sections are exploited for modeling purposes. The main targets and essential properties of the proposed model are shortly outlined in section 4.1. The main results are presented in two sections: Section 4.2 introduces the concept of a cross-stream length scale, which characterizes the boundary layer of the dense two-phase flow. Section 4.3 contains the modeling of the inter-phase momentum exchange and defines proper boundary conditions (section 4.3.5). The boundary layer concept is applied to evaporation in section 4.4. A simple turbulence model is applied in section 4.5. The model is summarized in section 4.6.

## 4.1 Spray model motivation and outline

Target definition

The main intention of the simplified spray model developed in the following is to provide an estimate of the local dispersed phase mass concentration and the gas phase air fuel mixture quality resulting from evaporation. Based on the validated CFD model results (section 3.2) and especially inspired by the characteristics obtained from cross-stream averaging (section 4.2), the model is designed to meet three major characteristics:

- Spatial changes are resolved along the main injection direction. For this reason, a *one-dimensional* description is sought.

- The model is to provide a dynamic response to transient boundary conditions such as injection conditions (mean mass and momentum fluxes) and global carrier phase conditions (such as carrier phase pressure and temperature). Hence, a *transient* description is derived. (A steady state description is found to be not applicable to model the high-pressure hollow-cone injection process.)

- The temporal evolution of the overall penetration behavior of the two-phase jet and the local air fuel mixture quality results from the local inter-phase exchange of mass, momentum and thermal energy (kinematic and thermal inhomogeneity). The description of the strong interaction between both phases during injection necessitates a *two-phase* description (i.e. no mixture model is applied).

Model outline

During injection, the width of the cross-stream distribution of dispersed phase characteristics such as mass, momentum and thermal
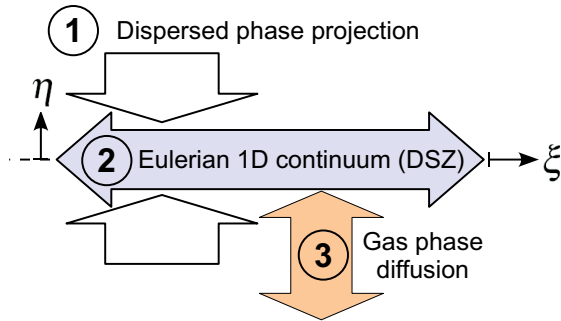
Figure 4.1: Dispersed phase projection onto a "dense spray zone" (DSZ); sketch
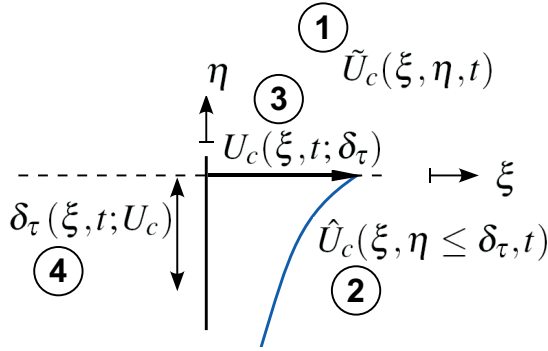
Figure 4.2: Gas phase approximation in the vicinity of the DSZ; sketch

energy concentration is small where the velocity difference between phases is high and vice versa. Therefore, the effect of the dispersed phase on the carrier phase is modeled to result from an infinitesimally thin sheet of dispersed phase mass. This is illustrated in figure 4.1 as a cross-stream projection of dispersed phase mass (number "1") onto a "dense spray zone" (DSZ).

The thin sheet exclusively contains dispersed phase and all liquid dispersed phase is contained within the thin sheet, so that liquid volume loading within the sheet is equal to one. Therefore, the liquid phase is treated as an Eulerian continuum (number "2" in figure 4.1).

The exchange of momentum, energy and fuel species mass between both phases is modeled to happen at the interface of the thin sheet. In the one-dimensional model, only streamwise gradients along the coordinate ξ are explicitly resolved. So transport processes within the carrier phase in the direction normal to the main injection direction along the coordinate η are modeled as diffusion processes (number "3" in figure 4.1).

The cross-stream diffusion is characterized by means of a cross-stream length scale δ_τ. The major part of section 4.3 covers the deriva-

tion of a transient description of δ_τ depending on the streamwise gas phase velocity U_c at the DSZ (figure 4.2). Starting from the time dependent field $\tilde{U}_c(\xi, \eta, t)$ (number "1"), the approximate velocity $\hat{U}_c(\xi, \eta \leq \delta_\tau, t)$ (number "2") describes the gas phase velocity field in the vicinity of the "dense spray zone" (DSZ). It depends only on the streamwise velocity $U_c(\xi, t; \delta_\tau)$ within the DSZ (number "3") and the local cross-stream length scale $\delta_\tau(\xi, t; U_c)$ (number "4"). The dependency of the gas phase characteristics on the cross-stream coordinate η is eliminated.

4.2 Cross-stream length scales

In the one-dimensional transport equations derived in this section, the dependency of the transported variables on the coordinate η normal to the main injection direction is to be eliminated. As a consequence, physics corresponding to cross-stream length scales need to be modeled. In the following, four cross-stream length scales are discussed.

Firstly, there are flow dependent cross-stream length scales: The jet width $\mathscr{L}_{DSZ}^{(c)}$ is defined by the volume occupied by the liquid drops (figure 4.3). The length scale $\mathscr{L}_{BL}^{(c)}$ describes the carrier phase boundary layer thickness which is induced by the injection.
Secondly, there are length scales which do not depend on the flow: Each line between the injector axis and the chamber walls, which is

Two-dimensional field	$\tilde{U}_c(\xi, \eta, t)$
Approximation for the DSZ vicinity (two-dimensional)	$\hat{U}_c(\xi, \eta \leq \delta_\tau, t)$
DSZ field (one-dimensional)	$U_c(\xi, t; \delta_\tau)$

Table 4.1: Field nomenclature on the example of the streamwise carrier phase velocity, see figure 4.2
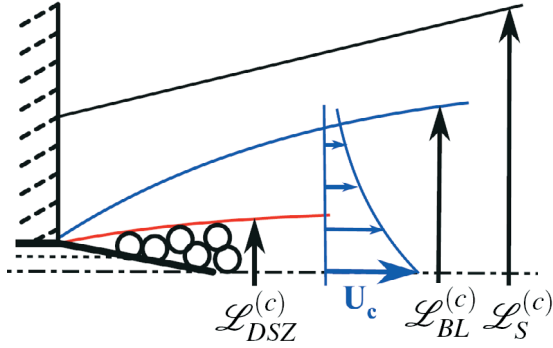
Figure 4.3: Main cross-stream length scales

normal to the hollow cone sheet characterizes a length scale. Its length is constant in time, but variable in space and thus depends on the chamber geometry. A more robust cross-stream length scale results from the definition of an arbitrary but spatially fixed geometry like the one indicated by $\mathscr{L}_S^{(c)}$ in figure 4.3.

Cross-stream volume averages

In order to motivate the spray model, cross-stream volume averages of the experimentally validated flow fields obtained in section 3.2 are analyzed here. A sector width $\mathscr{L}_S^{(c)}$ (figure 4.3) should be chosen such that the major part of the dispersed phase mass (respectively momentum, see figure 3.10 on page 72) and also the induced carrier phase vortex structures (see figue 3.19 on page 87) are contained. The vectors at the sector boundary in figure 4.4 indicate the carrier phase velocity, which is comparatively small in magnitude.
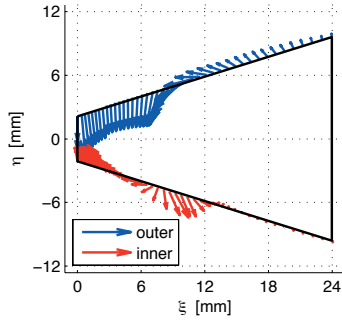
Figure 4.4: Sector geometry definition with carrier phase velocity vectors at $t = 0.5$ ms and $p = 10$ bar
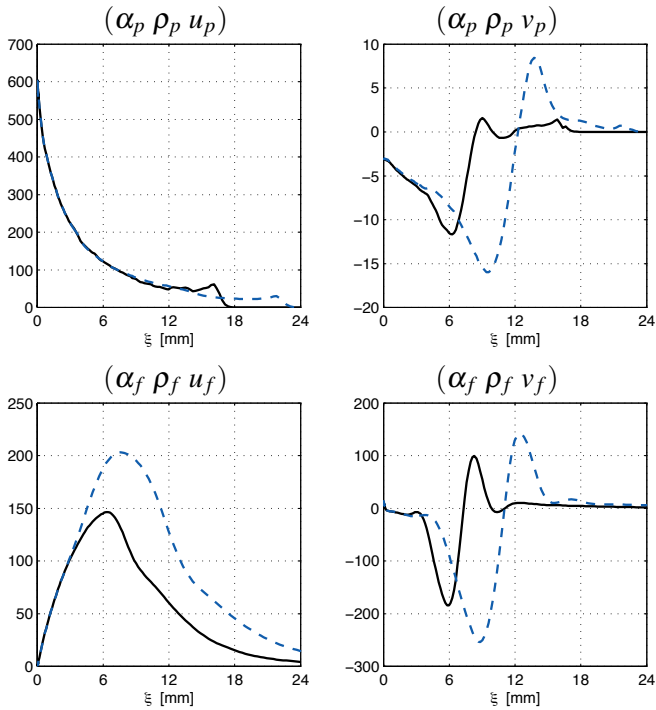
Figure 4.5: Sector averaged dispersed phase (top) and carrier phase momentum (bottom); $p = 10$ bar; streamwise (left) and cross-stream component (right); $t = 0.3$ ms (solid line) and $t = 0.5$ ms (dashed line)
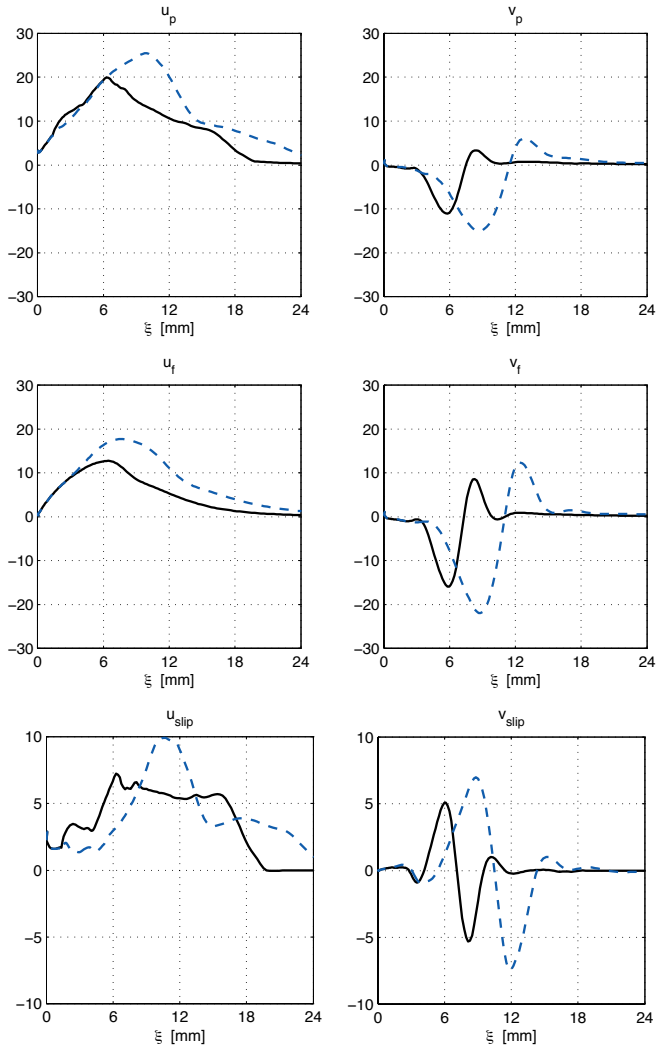
Figure 4.6: Sector averaged velocities: streamwise u and cross-stream components v of dispersed (index "p") and carrier phase (index "f") and slip velocity; $p = 10\,\text{bar}$, $t = 0.3\,\text{ms}$ (cont. line) and $0.5\,\text{ms}$ (dashed line)

The volume average

$$\overline{\Phi} = \int \Phi \, dV \Big/ \int dV \tag{4.1}$$

of quantity Φ is calculated based on cross-stream volume averaging over the sector geometry.

The mean dispersed phase streamwise momentum ($\Phi = \alpha_p \rho_p u_p$) is large close to the injection outlet and almost constant in time during injection (figure 4.5). The cross-stream component ($\Phi = \alpha_p \rho_p v_p$) is orders of magnitude smaller. This evaluation supports the assumption of the dominance of the injection direction introduced earlier.
Despite of the density ratio $\rho_p/\rho_f \approx 100 \gg 1$, the mean streamwise momentum of the gas phase within the sector acquires larger values than the liquid droplets. This reflects the observation of $\mathscr{L}_{DSZ}^{(c)} \ll \mathscr{L}_{BL}^{(c)}$. The mean velocities of both phases as well as the slip velocity $v_{slip} = v_p - v_f$ are displayed in figure 4.6. Maximum mean streamwise velocities are of the order of $20 \, m/s$ with corresponding slip velocities of about $5 \, m/s$.

Between the two time steps considered in figure 4.6, a steady state for the sector volume averaged quantities is reached by the dispersed phase for $\xi < 6 \, mm$ and by the carrier phase for $\xi < 4 \, mm$ at $t = 0.3 \, ms$. Since at this instant in time, the dispersed phase penetration depth is approximately $\xi = 17 \, mm$ (figure 4.5), the major streamwise portion of the flow is in transient conditions.

Although $\mathscr{L}_S^{(c)}$ represents a larger length scale than the liquid sheet scale $\mathscr{L}_{DSZ}^{(c)}$ and even the gas phase boundary layer width $\mathscr{L}_{BL}^{(c)}$, no invariants may be deduced from the volume averaged momentum fluxes or velocities. Thus it is not feasible to base the one-dimensional model on averaging over a large sector.

4.3 Momentum conservation

The primary physical effect controlling the injection process is the momentum exchange; it determines the propagation of the spray front. Momentum is supplied to the system by the injection of liquid mass through the injector outlet. Within the flow domain, the liquid phase exhibits a slip velocity with regards to the carrier phase. Therefore, momentum is exchanged between both phases.

A locally high slip velocity (and the corresponding inter-phase momentum exchange) experiences changes with respect to:

- *time* (especially during injection) and

- *space* (especially close to the injection outlet).

The appropriate modeling of these flow conditions is the basis for the flow evolution in regions further away from the injection outlet and at times after injection.

A *presumed spray center line* is identified as the primary direction of momentum exchange [*]: Due to the injector mounting position and geometry – namely the angle θ between injector axis and the presumed spray symmetry line (see figure 3.2.1 on page 61) – , the direction of the dispersed phase mass and momentum flux dominates the flow structure in the region close to the injector exit (dominance of the cone geometry). The injector is assumed to provide a rotationally perfectly symmetrical spray, so that circumferential gradients may be neglected. In order to account for changes along the dominant flow direction while neglecting gradients both normal to the main injection direction and along the circumferential direction, a *one-dimensional* description is sought.

---

[*]This is also supported by the dominance of the streamwise drag force magnitude acting along the main injection direction, see figure 3.13 on page 76

4.3.1 Dispersed phase and dense spray zone

This section covers the modeling of the dispersed phase. The shape of its cross-stream distribution as well as the region where momentum is exchanged with the carrier phase are specified. Space-integral conservation equations for the dispersed phase mass and momentum are presented.

Thin dense spray zone (DSZ)

The dispersed phase is modeled to occupy a smaller volume than the carrier phase. At any streamwise location ξ, the cross-stream characteristic length scale $\mathcal{L}_{DSZ}^{(c)}$ of the volume occupied by the major part of the dispersed phase is smaller than the characteristic length scale of the carrier phase shear boundary layer $\mathcal{L}_{BL}^{(c)}$ (figures 4.3 and 4.7). Therefore with regards to the carrier phase, the DSZ is modeled to yield a *zero cross-stream width* ($\mathcal{L}_{DSZ}^{(c)} = 0$), i.e. the DSZ carries no carrier phase mass ($\alpha_p^{(DSZ)} = 1$).

Due to streamwise velocity gradients within the DSZ, dispersed phase mass may locally accumulate. Streamwise accumulation of dispersed phase mass is accounted for by the dispersed phase continuity equation (see eq. (2.3)). In a finite volume approach, the transport of dispersed phase bulk density $\overline{\rho}_p$ is described by

$$\frac{\partial \overline{\rho}_p}{\partial t} + \frac{\partial (\overline{\rho}_p \, u_p)}{\partial \xi} + \overline{\rho}_p \frac{u_p \, \sin\theta + v_p \, \cos\theta}{\xi \, \sin\theta + \eta \, \cos\theta} = \overline{\Gamma}_p \,. \tag{4.2}$$

The dependency on the cross-stream coordinate η in equation (4.2) has been eliminated by means of a modeling step: With regards to the carrier phase, dispersed phase mass is projected onto the presumed hollow cone sheet (see the assumption of a "thin dense spray zone" above). Mathematically, the projection corresponds to a spatial integration with respect to the cross-stream coordinate η. Within the DSZ,

the (projected) dispersed phase mass

$$M_p(\xi) \equiv \int\limits_{\eta=-\xi/\tan\theta}^{\infty} \overline{\rho}_p(\xi,\,\eta)\,d\eta \,\bigg/\, \mathscr{L} \qquad (4.3)$$

is transported. The lower bound of the integral results from the injector symmetry axis so that in the case of $\theta \to \pi/2$ (a hollow-cone opening angle of 180°), $\eta \to -\infty$. Additionally, both the upper and lower bounds may be restricted by the chamber geometry. The length scale $\mathscr{L}$ in the denominator of equation (4.3) ensures that formally, a volume specific formulation may be maintained when covering for the carrier phase[†] so that the projected dispersed phase mass concentration M_p still yields units kg/m³. The length scale $\mathscr{L}$ is assumed to be constant in time and space.

Due to the dominance of the streamwise dispersed phase flow during injection, the maximum streamwise velocity of the cross-stream profiles $U_p(\eta)$ occurs at the presumed spray center line. As a consequence from the strong streamwise velocity component, the cross-stream velocity $V_p = 0$ at the presumed spray center line $\eta = 0$.

The cross-stream integrated conservation equation of the dispersed phase mass M_p (units kg/m³) therefore reads

$$\frac{\partial M_p}{\partial t} + \frac{\partial(M_p\,U_p)}{\partial\xi} + \frac{M_p\,U_p}{\xi} = \Gamma_p\,. \qquad (4.4)$$

Inter-phase momentum exchange

Inter-phase momentum exchange is modelled to occur *at the interface of the DSZ.*

[†] Note that in equation (4.3), division by the length integral $\int d\eta$ instead of the length scale $\mathscr{L}$ produces a cross-stream *average* of the dispersed phase mass distribution. This is not aimed for in the modeling of the dense hollow cone sheet spray.

The drag force $\mathscr{F}_D$ acting between the two phases is determined from the dispersed phase characteristics *within* the DSZ (namely the dispersed phase velocity U_p) and the carrier phase characteristics *adjacent* to the DSZ (namely the continuous phase velocity U_c, see figure 4.7). Although the DSZ spatially separates a region of high dispersed phase mass concentration, its zero width with regards to the carrier phase allows to treat the carrier phase velocity field as continuous. Nevertheless, only an infinitesimally thin sheet of the carrier phase mass interacts with the dispersed phase (which results in jumps in the corresponding spatial derivatives of the carrier phase velocity normal to the DSZ).

The drag force $\mathscr{F}_D$ acting on the dispersed phase is modeled by means of the isolated particle drag law (*dilute* dispersed two-phase flow assumption). It results from the dispersed phase particle diameter D_p and velocity U_p as well as from the carrier phase velocity U_c adjacent
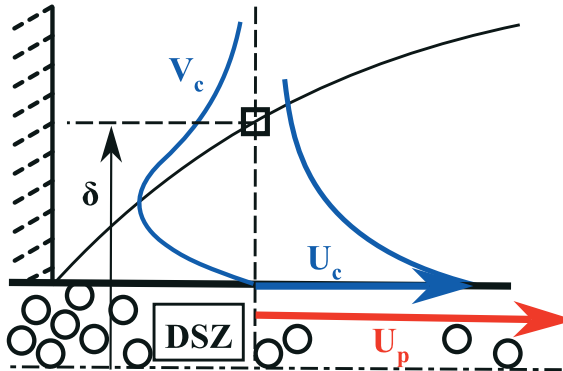
Figure 4.7: Dense spray zone with induced carrier phase boundary layer and entrainment; sketch

to the DSZ and its dynamic viscosity μ_c (see eq. (3.26))[‡]

$$\mathscr{F}_D^{(iso)} = 3\pi\mu_c \, D_p \, f_{SN} \, (U_p - U_c) \, . \qquad (4.5)$$

The total drag force

$$\mathscr{F}_D = N_p \, \mathscr{F}_D^{(iso)} = M_p \, \frac{18 \, \mu_c \, f_{SN}}{\rho_p \, D_p^2} \, (U_p - U_c) \qquad (4.6)$$

results from the number of particles per unit volume N_p. The development of the dispersed phase streamwise momentum within the DSZ is described by a momentum conservation equation (see eq. (2.4)) for the product $(M_p U_p)$ (which yields units $\mathrm{N/m^3}$)

$$\frac{\partial (M_p \, U_p)}{\partial t} + \frac{\partial (M_p \, U_p^2)}{\partial \xi} + \frac{M_p \, U_p^2}{\xi} = -\mathscr{F}_D \, . \qquad (4.7)$$

Negligible dispersed phase turbulence and collisions

In section 2.1, the effects of droplet collision and coalescence were mentioned. Likewise, the dispersed phase elements within a certain computational volume may locally exhibit a non-homogeneous distribution in droplet size, velocity and temperature. In the conditions

---

[‡] Depending on the local slip velocity, the carrier phase experiences high drag forces for short periods of time until the dispersed phase velocity is reached. The relaxation of slip velocities of isolated particles (at low dispersed phase loading)

$$\frac{\partial u_{sl}}{\partial t} = \frac{\partial (u_p - u_c)}{\partial t} = \frac{1}{\mathscr{T}_p} \, (u_p - u_c)$$

resulting from drag between both phases may also be characterized by the so called particle relaxation time

$$\mathscr{T}_p = \frac{\rho_p \, D_p^2}{18 \, \mu_c \, f_{SN}} \, .$$

For small particle Reynolds numbers (Stokes flow: $Re_p = \rho_c u_{sl} D_p / \mu_c \ll 1$), the drag correlation factor of Schiller and Naumann [107] reduces to $f_{SN} = 1$.

named above (especially the high transients, high dispersed phase volume loading and high cross-stream gradients), these effects are hard to model both on an individual droplet level and in an integral manner. The model proposed here is supposed to provide an estimate of the *mean* rates of inter-phase momentum and energy transfer. As a consequence, the effects of droplet collision and coalescence are considered to be of secondary importance and therefore neglected in the present level of modeling.

Although the presence of particles within a shear layer is known to influence both shear layer characteristics as well as the evolution of the dispersed phase concentration itself [19, 33, 126], these interactions are not incorporated in the model.

Eulerian dispersed phase continuum

According to the discussion in the dispersed phase modeling section 3.1.2 and the CFD section 3.1.4, the local dispersion in dispersed phase characteristics such as particle diameter or temperature is identified as a secondary effect as well. Consequentially, the dispersed phase is modeled to exhibit locally homogeneous velocity and temperature. Moreover, the size of the dispersed phase elements is characterized by one globally homogeneous diameter, assumed to be representative of the overall behavior of the two-phase flow (mono-dispersion).

4.3.2 Carrier phase integral boundary layer description

In this section, a cross-stream length scale characteristic to the carrier phase is identified and employed for the modeling of cross-stream shear stresses.

Carrier phase incompressibility

A mean injection velocity of about $u_p^{(inj)} = 200\,\mathrm{m/s}$ has been estimated in section 3.1.4. At $p_c = 10\,\mathrm{bar}$ and $T_c = 300\,\mathrm{K}$, the speed of sound of

the carrier phase is approximately

$$c_s = \sqrt{\kappa R T} = \left(1.4 \cdot \frac{8.3143}{28 \cdot 10^{-3}} \cdot 300 \right)^{\frac{1}{2}} m/s \approx 350 \, m/s \, . \quad (4.8)$$

Due to the density ratio of about $\rho_p/\rho_c \approx 100$ it may be assumed that in the vicinity of the injector outlet and during injection, the dispersed phase elements ejected from the injector locally impose a carrier phase velocity of the order of the dispersed phase velocity. In the vicinity of the injector outlet, a Mach number of about $\text{Ma} = \frac{u_c}{c_s} \approx 0.57$ may be expected. This increased Mach number suggests that compressibility effects have to be taken into account close to the injector outlet.

On the other hand, a similar spatial position of individual particles may result from different particle's "histories" (i.e. particle paths): Dispersed phase elements injected early during injection may already be exposed to drag with the carrier phase for a comparatively long period of time. By contrast, recently injected particles may have traveled through an already accelerated carrier phase environment and may still carry a larger amount of momentum at the same position in space (dispersed phase velocity dispersion). For this reason, the front of the two-phase jet consists of ever changing particles constantly overtaking each other ("cyclist effect"). The high momentum of recently injected particles is reduced very fast as soon as they reach the spray front. As a consequence, the propagation velocity of the two-phase jet front is considerably smaller than the velocity of individual particles within the two-phase jet. The mean spray front penetration velocity at 10 bar chamber pressure displayed in figure 3.8 (page 67) up to the time of 0.3 ms after begin of injection is of the order of $u_{front} = 60$ m/s. The corresponding Mach number $\text{Ma} = 0.17$ indicates that compressibility has a comparatively small influence at the level of the spray front propagation.

In the direction normal to the injection direction, the streamwise car-

rier phase velocity reduces within a smaller length than the spray penetration length so that local Mach numbers decrease. On the other hand, a locally occurring carrier phase velocity of e.g. $u_c = 200\,\text{m/s}$ at $p_c = 10\,\text{bar}$ ($\rho_c \approx 10\,kg/m^3$) corresponds to a dynamic pressure of $p_{dyn} = \rho_c/2 \cdot u_c^2 \approx 2\,\text{bar}$. As a result, the carrier phase density at the position of such high convective velocity is about 20% smaller than the pressure condition far away from the dense two-phase jet, and consequentially, a non-negligible pressure gradient $\frac{\partial p_c}{\partial \eta}$ contributes to the cross-stream momentum conservation equation.

Since both phases are modeled to be spatially separated, bulk effects due to gradients in volume fractions do not occur.

In summary, pressure fluctuations within the carrier phase are assumed to propagate faster than the local convective velocities ($Ma \ll 1$) and the carrier phase is modeled to be not compressible.

Limited DSZ carrier phase capacity

The zone of strong dispersed phase volume loading (dense spray zone *DSZ*, see figure 4.7) is assumed to be much thinner than the carrier phase boundary layer thickness. Consequently, the dispersed phase is modeled to directly interact with only a very small amount of carrier phase mass. Due to the high density ratio $\rho_p/\rho_c \gg 1$ (e.g. at $10\,\text{bar}$ gas pressure and $300\,\text{K}$ gas temperature, $\rho_p/\rho_c = \mathscr{O}\left(10^2\right)$), the drag force resulting from local slip between both phases leads to an acceleration of the carrier phase: If the carrier phase mass exchanges momentum directly with dispersed phase, it would almost instantaneously be accelerated to the dispersed phase velocity [§].

[§] Because of the locally high bulk density ratio between dispersed and carrier phase $\overline{\rho}_p/\overline{\rho}_c = (\alpha_p\rho_p)/(\alpha_f\rho_f)$, the drag force (eq. (4.6)) primarily acts on the carrier phase. The time scale

$$\mathscr{T}^{(c)}_{drag} = \frac{U_p - U_c}{\frac{\partial (U_p - U_c)}{\partial t}} \tag{4.9}$$

As a consequence, the amount of carrier phase mass directly exposed to exchange of mass, momentum, and thermal energy with the dispersed phase (which is supposed to happen at the boundary of the DSZ) is negligible. In other words: In comparison to the carrier phase fluxes occurring outside the DSZ, the ability of the carrier phase to store mass, momentum and thermal energy within the DSZ is negligible. Consequentially, the ability of the carrier phase to exchange e.g. momentum with the dispersed phase depends on momentum diffusion normal to the main injection direction.

Diffusion normal to the main injection direction is defined by the cross-stream velocity profile.

Carrier phase velocity profile

As a consequence from the dominant dispersed phase momentum flux during injection, the carrier phase is strongly accelerated near the spray center line, which in turn causes strong entrainment: The width of the carrier phase boundary layer thickness is limited and an "accelerated wall" type profile develops (see section 3.2.3, e.g. figure 3.12 on page 75).
Further downstream, a single phase jet like S-profile develops. Nevertheless, streamwise slip velocities are of the same order of magnitude as in the region of the upstream "accelerated wall" boundary layer (see figure 3.11). Also, the cross-stream width occupied by the dis-

---

at which carrier phase is exposed to acceleration resulting from drag at high dispersed phase concentrations (as it is the case within/close to the DSZ) relates the current slip velocity $U_{sl} = U_p - U_c$ to its rate of change.

With the help of Newtons law $\mathscr{F}_D = \rho_c \, \frac{\partial (U_p - U_c)}{\partial t}$, the continuous phase acceleration time scale

$$\mathscr{T}_{drag,\,c}^{(c)} = \frac{\rho_c \, (U_p - U_c)}{\mathscr{F}_D} \tag{4.10}$$

is obtained. In the limit of the DSZ assumption ($\alpha_c \to 0 \Leftrightarrow \overline{\rho}_p / \overline{\rho}_c \to \infty$), the carrier phase acceleration time scale tends towards $\mathscr{T}_{drag,\,c}^{(c)} \to 0$.

persed phase mass is still smaller than the boundary layer thickness of the carrier phase (figure 3.11 left).

From the identification of the dominance of the dispersed phase momentum flux direction and the induced "accelerated wall" type boundary layer, two major properties of the carrier phase flow during injection may be deduced:

- The cross-stream maximum of the streamwise velocity occurs at the presumed spray center line (the "accelerated wall").

- The drag induced acceleration of carrier phase at the presumed spray center line causes the entrainment of additional gas phase towards the spray center line ("excess entrainment") so that the cross-stream component of the carrier phase velocity tends towards zero at the spray center line.

Cross-stream length scale

The carrier phase momentum is diffusively transported away from the DSZ due to cross-stream gradients of the carrier phase streamwise velocity: A carrier phase boundary layer is formed close to the DSZ (figure 4.7). Because the velocity normal to the main injection direction is not spatially resolved, a cross-stream gradient cannot be estimated and a length scale characterizing the shearing motion close to the DSZ δ_τ has to be modeled.

The carrier phase velocity within the shear layer is large (especially close to the DSZ), thus the carrier phase far away from the DSZ may be modeled as quiescent. The length scale δ_τ characterizing the maximum shear stress (occurring in the vicinity of the DSZ) is modeled as the length scale of the maximum cross-stream velocity gradient $\frac{\partial U_c}{\partial \eta}$ adjacent to the DSZ (see figure 4.8):

$$\frac{\partial U_c}{\partial \eta} = -\frac{U_c}{\delta_\tau}.$$ (4.11)

4.3.3 Cross-stream length scale dynamics

In the previous section, δ_τ was defined as the cross-stream length scale characterizing the shear force within the gas phase adjacent to the DSZ (equation (4.11)). This section focuses on the modeling of the *transients* occurring within the two-phase flow.

Because also the cross-stream length scale is supposed to exhibit a transient behavior, it should characterize the immediate vicinity of the DSZ. The model is intended to resolve small time scale transients. Since information about flow transients is transported at finite speed, a small length scale is needed to ensure a sufficient temporal response of the model. Because the length scale δ_τ characterizing the cross-stream gradient at the DSZ interface is smaller than e.g. the mass defect δ_1 or the momentum thickness δ_2 (see figure 4.8), it constitutes a good choice with respect to a transient description.

In order to describe the dynamics of the carrier phase shear layer adjacent to the DSZ, the rate of change of the boundary layer thickness δ_τ characterizing the carrier phase gradient adjacent to the DSZ
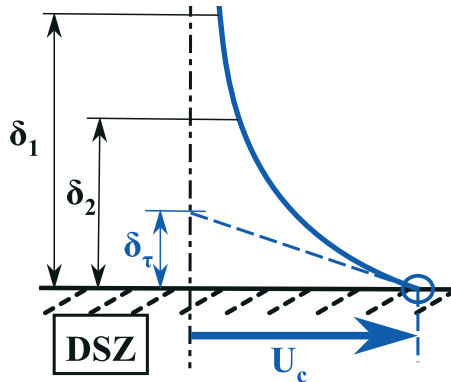
Figure 4.8: Injection induced carrier phase boundary layer length scales and maximum shear stress; sketch

(see eq. (4.11)) needs to be quantified. In total, the time rate of change of the local two-phase jet boundary layer thickness length scale

$$\left(\frac{\partial \delta_\tau}{\partial t}\right)^{(TPF)} = \left(\frac{\partial \delta_\tau}{\partial t}\right)^{(conv)} + \left(\frac{\partial \delta_\tau}{\partial t}\right)^{(\mu)} \tag{4.12}$$

is composed of contributions due to changes due to convective fluxes and due to gradient diffusion of momentum.

The convective term

$$\left(\frac{\partial \delta_\tau}{\partial t}\right)^{(conv)} = \left(\frac{\partial \delta_\tau}{\partial t}\right)^{\left(\frac{\partial U_c}{\partial \xi}\right)} + \left(\frac{\partial \delta_\tau}{\partial t}\right)^{(cone)} + \left(\frac{\partial \delta_\tau}{\partial t}\right)^{(exen)} \tag{4.13}$$

is composed of a contribution resulting from streamwise velocity gradients within the carrier phase and of the additional effect of local carrier phase acceleration due to drag with the dispersed phase and consequential excess entrainment (superscript "exen") [¶]. The convective part accounting for the carrier phase flux $\left(\frac{\partial \delta_\tau}{\partial t}\right)^{\left(\frac{\partial U_c}{\partial \xi}\right)}$ may be understood as the "usual" entrainment phenomenon occurring in single phase jets, where momentum is only supplied at the injection outlet and no additional momentum is introduced to the (carrier phase) jet within the flow domain.

Due to the cone geometry, a contribution $\left(\frac{\partial \delta_\tau}{\partial t}\right)^{(cone)}$ accounting for the radial widening is expected.

[¶] The speed of local excess entrainment due to local drag with the carrier phase and consequential contraction of the boundary layer may be characterized by means of an entrainment time scale $\mathscr{T}_{entr}^{(c)}$.

$$\mathscr{T}_{entr}^{(c)} = \frac{\delta_\tau}{\bar{V}_c}$$

Cross-stream length scale transport

In the following, a transport equation for the cross-stream length scale δ_τ is developed. The derivation starts from the two-dimensional stream-wise momentum conservation equation of the carrier phase (super-script "tilde"). Its terms are approximated in the vicinity of the DSZ by means of a Taylor series expansion (super-script "hat"). Derivatives of the cross-stream velocity component are substituted by means of the incompressible continuity equation. In order to drop the explicit dependence on the cross-stream coordinate η, the approximated streamwise momentum equation is integrated over the (comparatively small) cross-stream length scale δ_τ. With this choice, only the portion of the boundary layer in the direct vicinity of the DSZ is taken into account of the integration and a transient boundary layer description is obtained.

For the derivation of a transient description of the cross-stream length scale δ_τ, the streamwise momentum conservation equation for the carrier phase velocity field $\tilde{U}_c(\xi, \eta, t)$ in conical coordinates (see eq. (A.9) in the appendix)

$$
\frac{\partial \tilde{U}_c}{\partial t} + \tilde{U}_c \frac{\partial \tilde{U}_c}{\partial \xi} + \tilde{V}_c \frac{\partial \tilde{U}_c}{\partial \eta}
$$
$$
= \nu \left(\frac{\partial^2 \tilde{U}_c}{\partial \xi^2} + \frac{\sin\theta \frac{\partial \tilde{U}_c}{\partial \xi} + \cos\theta \frac{\partial \tilde{U}_c}{\partial \eta}}{\xi \, \sin\theta + \eta \, \cos\theta} + \frac{\partial^2 \tilde{U}_c}{\partial \eta^2} - \sin\theta \, \frac{\tilde{U}_c \, \sin\theta + \tilde{V}_c \, \cos\theta}{(\xi \, \sin\theta + \eta \, \cos\theta)^2} \right)
$$
$$
\tag{4.14}
$$

is employed for the carrier phase. In section 3.2.4, the second order cross-stream derivatives $\frac{\partial^2 (*)}{\partial \eta^2}$ (figure 3.18) were verified to be dominant among the viscous terms. So if the conventional boundary layer assumption

$$
\frac{\partial^2 (*)}{\partial \xi^2} \ll \frac{\partial^2 (*)}{\partial \eta^2}
\tag{4.15}
$$

is applied, then the streamwise momentum conservation equation reads

$$\frac{\partial \tilde{U}_c}{\partial t} + \tilde{U}_c \frac{\partial \tilde{U}_c}{\partial \xi} + \tilde{V}_c \frac{\partial \tilde{U}_c}{\partial \eta} = \nu \frac{\partial^2 \tilde{U}_c}{\partial \eta^2} \,. \tag{4.16}$$

Due to negligible compressibility effects within the carrier phase, the average density is $\rho_c^{(DSZ)} = const.$ and the continuity equation

$$\frac{\partial \overline{\rho}_c}{\partial t} + \frac{\partial (\overline{\rho}_c \tilde{U}_c)}{\partial \xi} + \frac{\partial (\overline{\rho}_c \tilde{V}_c)}{\partial \eta} + \overline{\rho}_c \frac{\tilde{U}_c \sin\theta + \tilde{V}_c \cos\theta}{\xi \sin\theta + \eta \cos\theta} = 0 \tag{4.17}$$

simplifies to

$$\frac{\partial \tilde{U}_c}{\partial \xi} + \frac{\partial \tilde{V}_c}{\partial \eta} + \frac{\tilde{U}_c \sin\theta + \tilde{V}_c \cos\theta}{\xi \sin\theta + \eta \cos\theta} = 0 \,. \tag{4.18}$$

The assumption of an incompressible carrier phase is used to approximate the first

$$\frac{\partial \tilde{V}_c}{\partial \eta} = -\frac{\partial \tilde{U}_c}{\partial \xi} - \frac{\tilde{U}_c \sin\theta + \tilde{V}_c \cos\theta}{\xi \sin\theta + \eta \cos\theta} \tag{4.19}$$

and second order derivatives based on the continuity equation (4.18)

$$\frac{\partial^2 \tilde{V}_c}{\partial \eta^2} = -\frac{\partial}{\partial \xi}\left(\frac{\partial \tilde{U}_c}{\partial \eta}\right) - \frac{\frac{\partial \tilde{U}_c}{\partial \eta} \sin\theta + \frac{\partial \tilde{V}_c}{\partial \eta} \cos\theta}{\xi \sin\theta + \eta \cos\theta} + \cos\theta \frac{\tilde{U}_c \sin\theta + \tilde{V}_c \cos\theta}{(\xi \sin\theta + \eta \cos\theta)^2} \,.$$
$$\tag{4.20}$$

Presumed center line

The cross-stream maximum of the streamwise velocity is defined as $U_c(\xi) = \tilde{U}_c(\xi, \eta)\big|_{\eta=0}$ and analogously $V_c(\xi) = \tilde{V}_c(\xi, \eta)\big|_{\eta=0}$. At the presumed center position $\eta = 0$, $V_c \approx 0$ due to a presumed flow symmetry. In two-phase flow, the carrier phase exchanges momentum with the dispersed phase so that a drag source term Φ_D is introduced to the

streamwise momentum equation (4.16)

$$\frac{\partial U_c}{\partial t} + U_c \frac{\partial U_c}{\partial \xi} = 2 \, v \, \frac{\partial^2 U_c}{\partial \eta^2} + \Phi_D \, . \tag{4.21}$$

The factor 2 in front of the diffusive part of equation (4.21) accounts for the fact that the hollow cone sheet is surrounded by two adjacent boundary layers.
With the approximation of the cross-stream gradient (equation (4.31) presented later in this section), the carrier phase momentum equation is

$$\frac{\partial U_c}{\partial t} + U_c \frac{\partial U_c}{\partial \xi} = \Phi_D - 2 \, v \, \frac{U_c}{\delta_\tau^2} \, . \tag{4.22}$$

Due to the primitive representation of the carrier phase momentum in equation (4.22), the momentum source term reads

$$\Phi_D = \frac{\mathscr{F}_D}{\rho_c} \, . \tag{4.23}$$

The sum of the RHS terms in equation (4.22) represents an effective specific drag force

$$\Phi_D^{(eff)} = \frac{\mathscr{F}_D}{\rho_c} - 2 \, v \, \frac{U_c}{\delta_\tau^2} \, , \tag{4.24}$$

which is experienced by the carrier phase at the presumed center line position. The final version of the carrier phase momentum conservation equation is

$$\frac{\partial U_c}{\partial t} + U_c \frac{\partial U_c}{\partial \xi} = \frac{\mathscr{F}_D}{\rho_c} - 2 \, v \, \frac{U_c}{\delta_\tau^2} = \Phi_D^{(eff)} \, . \tag{4.25}$$

The derivatives of equations (4.19) and (4.20) are

$$\frac{\partial V_c}{\partial \eta} = -\frac{\partial U_c}{\partial \xi} - \frac{U_c}{\xi} \ .$$

(4.26)

and [||]

$$\frac{\partial^2 V_c}{\partial \eta^2} = -\frac{\partial}{\partial \xi}\left(\frac{\partial U_c}{\partial \eta}\right) - \frac{1}{\xi}\left(\frac{\partial U_c}{\partial \eta} + \frac{1}{\tan\theta}\frac{\partial V_c}{\partial \eta}\right) + \frac{1}{\xi^2 \tan\theta} U_c \ .$$

(4.27)

Employing the continuity equation (4.19), the gradient $\frac{\partial V_c}{\partial \eta}$ and thus the dependency on the cross-stream velocity is eliminated

$$\frac{\partial^2 V_c}{\partial \eta^2} = -\frac{\partial}{\partial \xi}\left(\frac{\partial U_c}{\partial \eta}\right) - \frac{1}{\xi}\frac{\partial U_c}{\partial \eta} + \frac{1}{\xi \tan\theta}\frac{\partial U_c}{\partial \xi} + \frac{2}{\xi^2 \tan\theta} U_c \ .$$

(4.28)

Boundary layer approximation

The boundary layer thickness scale δ_τ as it is characterized in figure 4.8 is a flow property which *characterizes gas phase flow conditions at the presumed center line* (at $\eta = 0$). The temporal evolution of the local boundary layer length scale depends on the carrier phase momentum transport at the position at which it characterizes the cross stream gradient, namely at the presumed spray center line $\eta = 0$. A relation between the temporal and spatial gradients of U_c is given by equation (4.21) which covers also for the diffusive loss of streamwise momentum normal to the main flow direction. Note that an assumption on the cross-stream profile $U_c(\eta)$ is *not* needed for the description of the streamwise momentum transport at the presumed spray center

---

[||] Note that if the second derivative at the center line position directly derived from (4.26)

$$\frac{\partial^2 V_c}{\partial \eta^2} = -\frac{\partial}{\partial \xi}\left(\frac{\partial U_c}{\partial \eta}\right) - \frac{1}{\xi}\frac{\partial U_c}{\partial \eta} \ ,$$

a dependency on the cone opening angle θ may not be maintained.

line.

By contrast, the temporal development of δ_τ due to (see eq. (4.13))

- local acceleration of carrier phase mass due to drag with the dispersed phase and consequential excess entrainment (local contraction of the boundary layer cross-stream width) and

- streamwise gradients in δ_τ and U_c

remains to be modeled. Because convection of carrier phase mass towards the presumed center line needs to be modeled, an assumption on the velocity profile *in the vicinity of the DSZ* becomes inevitable.

Not the whole of the cross-stream profile needs to be modeled since the major influence of the flow at the presumed center line stems from the evolution of the flow in the vicinity of $\eta = 0$. Therefore, the cross-stream profile *in the vicinity* of the DSZ is approximated by means of the cross-stream length scale δ_τ in terms of the gradients *at* the DSZ, i.e. by means of a Taylor series expansion. In that fashion, e.g. the streamwise carrier phase velocity $\hat{U}_c(\eta)$ resulting from a Taylor expansion approximates the "exact" velocity field $\tilde{U}_c(\eta)$.

The procedure of deriving a relation for the local rate of change of the cross-stream length scale δ_τ is presented in the following. It depends on streamwise gradients of both that very length scale δ_τ and the streamwise carrier phase velocity at the DSZ $U_c = \tilde{U}_c(\eta = 0)$. The velocity profile $\hat{U}_c$ is approximated by a second order polynomial function.

The Taylor expansions of the streamwise and cross-stream velocity profiles read

$$\hat{U}_c(\eta) = U_c|_{\eta=0} + \eta \left. \frac{\partial U_c}{\partial \eta} \right|_{\eta=0} + \frac{\eta^2}{2} \left. \frac{\partial^2 U_c}{\partial \eta^2} \right|_{\eta=0} \qquad (4.29)$$

and

$$\hat{V}_c(\eta) = V_c|_{\eta=0} + \eta \left.\frac{\partial V_c}{\partial \eta}\right|_{\eta=0} + \frac{\eta^2}{2} \left.\frac{\partial^2 V_c}{\partial \eta^2}\right|_{\eta=0}. \tag{4.30}$$

When a cross-stream profile is defined by means of a second order approximating function (three fitting coefficients), three boundary conditions need to be applied in order to uniquely define the velocity profile. The cross-stream gradients are approximated by means of the cross-stream length scale δ_τ

$$\tilde{U}_c|_{\eta=0} = U_c, \quad \left.\frac{\partial \tilde{U}_c}{\partial \eta}\right|_{\eta=0} = \frac{\partial U_c}{\partial \eta} = -\frac{U_c}{\delta_\tau} \text{ and } \left.\frac{\partial^2 \tilde{U}_c}{\partial \eta^2}\right|_{\eta=0} = \frac{\partial^2 U_c}{\partial \eta^2} = \frac{U_c}{\delta_\tau^2} \tag{4.31}$$

so that the Taylor approximation of the cross-stream profile of the streamwise carrier phase velocity may be described by

$$\hat{U}_c(\eta) = U_c \left(1 - \frac{\eta}{\delta_\tau} + \frac{\eta^2}{2\,\delta_\tau^2}\right). \tag{4.32}$$

With the continuity assumption utilized in equations (4.26) and (4.28), the approximated cross-stream velocity close to the DSZ ($|\eta| \le \delta_\tau$)

$$\begin{aligned}
\hat{V}_c(\eta) = 0 - \eta \left(\frac{\partial U_c}{\partial \xi} + \frac{U_c}{\xi}\right) \\
- \frac{\eta^2}{2} \left[\frac{\partial(\frac{U_c}{\delta_\tau})}{\partial \xi} + \frac{1}{\xi}\frac{\partial U_c}{\partial \eta} - \frac{1}{\xi \tan \theta}\left(\frac{\partial U_c}{\partial \xi} + \frac{2\,U_c}{\xi \tan \theta}\right)\right]
\end{aligned} \tag{4.33}$$

may be expressed by means of the center line streamwise velocity

$$
\hat{V}_c(\eta) = -\eta \, \frac{\partial U_c}{\partial \xi} \left[1 - \frac{\eta}{2} \left(\frac{1}{\delta_\tau} + \frac{1}{\xi \, \tan \theta} \right) \right]
$$
$$
- \frac{\eta}{\xi} \, U_c \left[1 - \eta \left(\frac{1}{2\delta_\tau} + \frac{1}{\xi \, \tan \theta} \right) \right] - \frac{\eta^2}{2 \, \delta_\tau^2} \, U_c \, \frac{\partial \delta_\tau}{\partial \xi} \, .
$$

(4.34)

Integrated momentum equation

The Taylor approximation $\hat{U}_c$ (eq.(4.32)) is now inserted into the individual terms of eq. (4.16)

$$
\frac{\partial \hat{U}_c}{\partial t} = \frac{\partial U_c}{\partial t} \left(1 - \frac{\eta}{\delta_\tau} + \frac{\eta^2}{2 \, \delta_\tau^2} \right) + U_c \, \frac{\eta}{\delta_\tau^2} \left(1 - \frac{\eta}{\delta_\tau} \right) \frac{\partial \delta_\tau}{\partial t} \quad (4.35)
$$

$$
\frac{\partial \hat{U}_c}{\partial \xi} = \frac{\partial U_c}{\partial \xi} \left(1 - \frac{\eta}{\delta_\tau} + \frac{\eta^2}{2 \, \delta_\tau^2} \right) + U_c \, \frac{\eta}{\delta_\tau^2} \left(1 - \frac{\eta}{\delta_\tau} \right) \frac{\partial \delta_\tau}{\partial \xi} \quad (4.36)
$$

$$
\frac{\partial \hat{U}_c}{\partial \eta} = -\frac{U_c}{\delta_\tau} \left(1 - \frac{\eta}{\delta_\tau} \right) \quad (4.37)
$$

$$
\frac{\partial^2 \hat{U}_c}{\partial \eta^2} = \frac{U_c}{\delta_\tau^2} \quad (4.38)
$$

and the corresponding products of eq. (4.16) are formed.

$$
\hat{U}_c \, \frac{\partial \hat{U}_c}{\partial \xi} = U_c \left\{ \frac{\partial U_c}{\partial \xi} \left[1 - 2 \, \frac{\eta}{\delta_\tau} + 2 \left(\frac{\eta}{\delta_\tau} \right)^2 - \left(\frac{\eta}{\delta_\tau} \right)^3 + \frac{1}{4} \left(\frac{\eta}{\delta_\tau} \right)^4 \right] \right.
$$
$$
\left. + \frac{U_c}{\delta_\tau} \, \frac{\eta}{\delta_\tau} \, \frac{\partial \delta_\tau}{\partial \xi} \left[1 - 2 \, \frac{\eta}{\delta_\tau} + \frac{3}{2} \left(\frac{\eta}{\delta_\tau} \right)^2 - \frac{1}{2} \left(\frac{\eta}{\delta_\tau} \right)^3 \right] \right\}
$$

(4.39)

$$\hat{V}_c \frac{\partial \hat{U}_c}{\partial \eta} = U_c \frac{\eta}{\delta_\tau} \left(\frac{\partial U_c}{\partial \xi} + \frac{U_c}{\xi} \right) \left[1 - \frac{3}{2} \frac{\eta}{\delta_\tau} + \frac{1}{2} \left(\frac{\eta}{\delta_\tau} \right)^2 - \frac{\eta}{\xi \tan \theta} \left(1 - \frac{\eta}{\delta_\tau} \right) \right]$$

$$- \frac{\eta^2}{2\xi \delta_\tau \tan \theta} U_c \frac{\partial U_c}{\partial \xi} \left(1 - \frac{\eta}{\delta_\tau} \right) + \frac{\eta^2}{2\delta_\tau^3} U_c^2 \frac{\partial \delta_\tau}{\partial \xi} \left(1 - \frac{\eta}{\delta_\tau} \right)$$

$$(4.40)$$

As a result of the Taylor approximation, the gradients at the DSZ boundary $\frac{\partial U_c}{\partial t}$, $\frac{\partial U_c}{\partial \xi}$ and U_c are expressed independent from the η coordinate in the vicinity of the DSZ.

The dependence of the terms contributing to the streamwise momentum equation (4.16) on the cross-stream coordinate η is eliminated by integration over the cross-stream direction.

$$\int_0^{\delta_\tau} \frac{\partial \hat{U}_c}{\partial t} \, d\eta = \frac{2}{3} \delta_\tau \frac{\partial U_c}{\partial t} + \frac{1}{6} U_c \frac{\partial \delta_\tau}{\partial t} \qquad (4.41)$$

$$\int_0^{\delta_\tau} \left(\hat{U}_c \frac{\partial \hat{U}_c}{\partial \xi} \right) d\eta = \frac{7}{15} \delta_\tau U_c \frac{\partial U_c}{\partial \xi} + \frac{13}{120} U_c^2 \frac{\partial \delta_\tau}{\partial \xi} \qquad (4.42)$$

$$\int_0^{\delta_\tau} \left(\hat{V}_c \frac{\partial \hat{U}_c}{\partial \eta} \right) d\eta = \delta_\tau U_c \left(\frac{\partial U_c}{\partial \xi} + \frac{U_c}{\xi} \right) \left(\frac{1}{8} - \frac{1}{12} \frac{\delta_\tau}{\xi \tan \theta} \right)$$

$$- \frac{1}{24} \frac{\delta_\tau^2}{\xi \tan \theta} U_c \frac{\partial U_c}{\partial \xi} + \frac{1}{24} U_c^2 \frac{\partial \delta_\tau}{\partial \xi}$$

$$(4.43)$$

$$\int_0^{\delta_\tau} \left(\nu \frac{\partial^2 \hat{U}_c}{\partial \eta^2} \right) d\eta = \frac{U_c \nu}{\delta_\tau} \qquad (4.44)$$

Transient two-phase boundary layer (ttBL)

Insertion of the above terms into the integrated form of the streamwise momentum equation (4.16) leads to

$$
\delta_\tau \, \frac{\partial U_c}{\partial t} + \frac{1}{4} \, U_c \, \frac{\partial \delta_\tau}{\partial t} + \delta_\tau \, U_c \, \frac{\partial U_c}{\partial \xi} \left(\frac{71}{80} - \frac{3}{16} \frac{\delta_\tau}{\xi \, \tan \theta} \right)
$$
$$
+ \delta_\tau \, \frac{U_c^2}{\xi} \left(\frac{3}{16} - \frac{1}{8} \frac{\delta_\tau}{\xi \, \tan \theta} \right) + \frac{9}{40} \, U_c^2 \, \frac{\partial \delta_\tau}{\partial \xi} = \frac{3}{2} \, \frac{U_c \, \nu}{\delta_\tau}
$$

(4.45)

or (solved for $\frac{\partial \delta_\tau}{\partial t}$)

$$
\frac{\partial \delta_\tau}{\partial t} + \frac{4 \, \delta_\tau}{U_c} \, \frac{\partial U_c}{\partial t} + \delta_\tau \, \frac{\partial U_c}{\partial \xi} \left(\frac{71}{20} - \frac{3}{4} \frac{\delta_\tau}{\xi \, \tan \theta} \right)
$$
$$
+ \delta_\tau \, \frac{U_c}{\xi} \left(\frac{3}{4} - \frac{1}{2} \frac{\delta_\tau}{\xi \, \tan \theta} \right) + \frac{9}{10} \, U_c \, \frac{\partial \delta_\tau}{\partial \xi} = \frac{6 \, \nu}{\delta_\tau} \, .
$$

(4.46)

This is an equation quantifying the local rate of change $\frac{\partial \delta_\tau(\xi,t)}{\partial t}$ and therefore constitutes a transient, one-dimensional transport equation for the cross-stream length scale. The individual contributions introduced in equations (4.12) and (4.13) may now be identified. By means of the opening angle θ, it accounts for the geometry of a hollow cone. It covers for streamwise gradients in both the length scale measure δ_τ and the velocity U_c as well as for the acceleration due to drag with the dispersed phase.

The contributions of the overall rate of change of local length scale initially described in equations (4.12) and (4.13) may now be identi-

fied:

$$\left(\frac{\partial \delta_\tau}{\partial t}\right)^{(exen)} = -\frac{4}{U_c} \frac{\delta_\tau}{\partial t} \frac{\partial U_c}{\partial t} , \tag{4.47}$$

$$\left(\frac{\partial \delta_\tau}{\partial t}\right)^{\left(\frac{\partial U_c}{\partial \xi}\right)} = -\frac{71}{20} \delta_\tau \frac{\partial U_c}{\partial \xi} - \frac{9}{10} U_c \frac{\partial \delta_\tau}{\partial \xi} , \tag{4.48}$$

$$\left(\frac{\partial \delta_\tau}{\partial t}\right)^{(cone)} = -\delta_\tau \frac{U_c}{\xi} \left(\frac{3}{4} - \frac{1}{2} \frac{\delta_\tau}{\xi \tan \theta}\right) + \frac{3}{4} \frac{\partial U_c}{\partial \xi} \frac{\delta_\tau^2}{\xi \tan \theta} , \tag{4.49}$$

$$\left(\frac{\partial \delta_\tau}{\partial t}\right)^{(\mu)} = \frac{6 \nu}{\delta_\tau} . \tag{4.50}$$

4.3.4 ttBL model assessment

The proposed boundary layer model is designed to describe the transient response of the two-phase jet resulting from the injection of liquid fuel into air. The physical validity of the derived model equations is assessed in this section.

Analogies

At first sight, the proposed model shows similarities to classical boundary layer models as summarized in [108]: It is derived by cross-stream integration and it contains a boundary layer thickness in the resulting transport equation.

On the other hand, it shows clear differences to the classical integral methods: First of all, it does not exploit *self-similarity*, neither in space nor time. It describes the transient response of the local length scale δ_τ to boundary condition changes. Also, no boundary layer integral momentum or mass flux is transported by means of a conservation equation. Only the transport equation for the evolution of the local length

scale is described. The integral over the approximated streamwise momentum equation is only utilized in the course of its derivation.

In order to compare the proposed model to the classical boundary layer method, the integrals of mass and momentum based on the assumed velocity profile are derived in appendix B: For the plane 2D case, integral equations of mass and momentum contained within a boundary layer of thickness δ and with a presumed cross-stream velocity profile according to equation B.12 are assessed. The form and discussion of both the steady state integrals (equations B.14 and B.15) as well as their transient contributions (equations B.20 and B.21) support the validity of the proposed transport equation of the cross-stream length scale δ_τ (equation 4.46).

Variable local length scale

An other challenge of the model is to accept the concept of *transporting a non-sensible and non-conserved quantity* such as a local length scale as opposed to conserved variables like mass or energy. Nevertheless, the transport of non-conserved quantities is well accepted in other fields of fluid mechanics, e.g. the transport of a rate of dissipation of turbulent kinetic energy in the k-ε turbulence model.

The feasibility of the proposed transport equation (4.46) is discussed in the following section.

Presumed cross-stream velocity profile

The carrier phase velocity in the vicinity of the dense spray zone (DSZ) is modeled as a function of the flow characteristics inside the dense spray zone: The carrier phase velocity $\hat{U}_c(\eta)$ in the vicinity of the DSZ is approximated in terms of the DSZ carrier phase velocity U_c.

$$\hat{U}_c(\eta) = U_c \left(1 - \frac{\eta}{\delta_\tau} + \frac{\eta^2}{2\,\delta_\tau^2} \right) \tag{4.32}$$

For the approximation of the cross-stream velocity profile $\hat{U}(\eta)$, three boundary conditions at the presumed center line position are applied, see eq. (4.31).

At the position $\eta = \delta_\tau$, the approximated (modeled) cross-stream velocity profile $\hat{U}(\eta)$ according to eq. (4.32) produces the velocity $\hat{U}_c(\eta = \delta_\tau) = U_c/2$ and the velocity gradient $\frac{\partial \hat{U}_c(\eta = \delta_\tau)}{\partial \eta} = 0$. The same velocity profile is obtained if in eq. (4.31), the third boundary condition $\frac{\partial^2 \tilde{U}_c}{\partial \eta^2}\big|_{\eta=0} = \frac{\partial^2 U_c}{\partial \eta^2} = \frac{U_c}{\delta_\tau^2}$ is substituted by $\frac{\partial \tilde{U}_c}{\partial \eta}\big|_{\eta=\delta_\tau} = 0$.

So in terms of the 2D streamwise momentum equation

$$\frac{\partial \tilde{U}_c}{\partial t} + \tilde{U}_c \frac{\partial \tilde{U}_c}{\partial \xi} + \tilde{V}_c \frac{\partial \tilde{U}_c}{\partial \eta} = \nu \frac{\partial^2 \tilde{U}_c}{\partial \eta^2} \,, \qquad (4.16)$$

the approximated velocity profile $\hat{U}(\eta)$ (eq. (4.32)) has two major characteristics:

- Because $\frac{\partial \tilde{U}_c}{\partial \eta}\big|_{\eta=\delta_\tau} = 0$, the streamwise momentum transport at the boundary $\eta = \delta_\tau$ is independent from the magnitude of the approximated cross-stream velocity $\hat{V}(\eta = \delta_\tau)$: $(\hat{V} \frac{\partial \hat{U}}{\partial \eta})\big|_{\eta=\delta_\tau} = 0$

- As a consequence from the choice of a second order approximation, the cross-stream diffusion rate of the approximated streamwise momentum is modeled to be constant throughout the boundary layer: $\frac{\partial \hat{U}_c}{\partial \eta} = U_c/\delta_\tau$. Its magnitude is solely determined by the local boundary layer thickness δ_τ and the DSZ velocity U_c.

The two major properties mentioned above indicate that the choice of the presumed cross-stream velocity profile according to eq. (4.32) is well suited for cross-stream integration as presented in section 4.3.3.

Hollow cone geometry

Due to the hollow cone geometry, $\tan\theta$ may only take on values within the bounds $0 < \tan\theta \le \pi/2$. Because θ appears in the denominator, $\theta \to 0$ has to be excluded from the scope of validity of equation (4.46). In the context of the flow induced by the hollow cone injection, generally $\theta \approx 40^o$.

The cone opening angle θ only influences the cross-stream length scale transport when the boundary layer length scale δ_τ is of the order of the streamwise coordinate ξ. This condition is fulfilled only for comparatively small values of ξ, i.e. the influence of the cone opening angle θ is restricted to regions very close to the injector symmetry line. Far away from the injector symmetry line ($\xi \gg \delta_\tau$), the terms containing the cone opening angle θ may be neglected and equation (4.46) simplifies to

$$\frac{\partial\delta_\tau}{\partial t} + 4\frac{\delta_\tau}{U_c}\frac{\partial U_c}{\partial t} + \frac{71}{20}\delta_\tau\frac{\partial U_c}{\partial\xi} + \frac{3}{4}\frac{\delta_\tau\,U_c}{\xi} + \frac{9}{10}U_c\frac{\partial\delta_\tau}{\partial\xi} = 6\frac{\nu}{\delta_\tau}\,.$$
(4.51)

In regions very far away from the injector symmetry line ($\xi \to \infty$, where consequentially also $\xi \gg \delta_\tau$), the flux due to the cone term $(\delta_\tau\,U_c)/\xi$ may be neglected too and equation (4.51) reduces to

$$\frac{\partial\delta_\tau}{\partial t} + 4\frac{\delta_\tau}{U_c}\frac{\partial U_c}{\partial t} + \frac{71}{20}\delta_\tau\frac{\partial U_c}{\partial\xi} + \frac{9}{10}U_c\frac{\partial\delta_\tau}{\partial\xi} = 6\frac{\nu}{\delta_\tau}$$
(4.52)

which corresponds to the plane 2D case.

If in equation (4.52), the center line velocity U_c is in a steady state condition ($\frac{\partial U_c}{\partial t} = 0$) and streamwise gradients of both streamwise velocity U_c and boundary layer thickness δ_τ are negligible ($\frac{\partial(*)}{\partial\xi} = 0$), then the local boundary layer length scale grows only due to diffusion effects characterized by the momentum diffusion coefficient ν.

The terms in equation (4.52) containing streamwise gradients $\frac{\partial(*)}{\partial\xi}$ lead

to a local increase in cross-stream length scale when they are negative. Because δ_τ is positive by definition and generally due to the definition of the streamwise velocity U_c (see figure 4.8), also $U_c \geq 0$, negative streamwise gradients $\frac{\partial(*)}{\partial \xi} < 0$ cause the local boundary layer to grow. According to (4.52), a local carrier phase acceleration – e.g. due to drag with an injected dispersed phase – causes the cross-stream length scale to shrink.**

In the case of negligible diffusion and in globally steady state conditions $(\frac{\partial(*)}{\partial t})$, equation (4.52) may be integrated to yield a relation of $\delta_\tau(\xi)$ and $U_c(\xi)$ within the field depending on their prescibed boundary conditions $\delta_\tau^{(inj)} = \delta_\tau(\xi_0)$ and $U_c^{(inj)} = U_c(\xi_0)$, e.g at the injector exit location

$$U(\xi) = U^{(inj)} \left(\frac{\delta_\tau(\xi)}{\delta_\tau^{(inj)}} \right)^{-\frac{18}{71}} . \qquad (4.53)$$

Condition	δ_τ	U_c	M_p	U_p
Initial	500 μm	0.1 m/s	0.001 g	0.1 m/s
Injection	20 μm	n/a	16.67 g/s	200 m/s

Table 4.2: Initial and injection boundary conditions

4.3.5 Numerical scheme and boundary conditions

For the implementation of the proposed model, a finite-difference description is applied. The one-dimensional space is resolved by a computational grid with a non-equidistant distribution of points. Spatial gradients are calculated as centered differences of second order of accuracy with the help of Fornberg's formulas [54, 55]. Temporal integration is conducted with an simple Euler forward method.

The injection velocity $U^{(inj)}$ as well as temperature $T^{(inj)}$ are specified directly. The dispersed phase mass density $M_p^{(inj)}$ present at the injection node is calculated from the injected fuel mass flow rate $\dot{m}^{(inj)}$. During a time increment δt, a mass increment $\delta m_p^{(inj)} = \dot{m}^{(inj)} \, \delta t$ is injected. At the prescribed injection velocity $U_p^{(inj)}$, it will be transported over a length increment $\delta \xi = U_p^{(inj)} \, \delta t$. The resulting dispersed phase mass concentration present at the injection inlet is thereby defined as

$$M_p = \frac{\delta m_p^{(inj)}}{\delta \xi} = \frac{\dot{m}_p^{(inj)}}{U_p^{(inj)}} \ . \tag{4.54}$$

Initial and boundary conditions are listed in table 4.2. If not stated otherwise, the "injection" boundary conditions for the carrier phase are equal to the initialization state. At the downstream boundary, a zero gradient boundary condition is applied.

For the characteristic cross-steam length scale δ_τ, the condition at the

---

** If $\frac{\partial U_c}{\partial t}$ from equation (4.21) is inserted into (4.46), an alternative conservation equation for the cross-stream length scale δ_τ is obtained.

$$\frac{\partial \delta_\tau}{\partial t} + \frac{9}{10} U_c \frac{\partial \delta_\tau}{\partial \xi} = \delta_\tau \frac{\partial U_c}{\partial \xi} \left(\frac{9}{20} + \frac{3}{4} \frac{\delta_\tau}{\xi \tan \theta} \right)$$
$$+ \delta_\tau \frac{U_c}{\xi} \left(\frac{13}{4} + \frac{1}{2} \frac{\delta_\tau}{\xi \tan \theta} \right) + \frac{2\nu}{\delta_\tau}$$

injector position is assumed to be of the scale of the injector maximum opening of approximately 20 μm, see page 56. Initially, velocity gradients are negligible. This corresponds to a large cross-stream length scale. The value in table 4.2 is chosen arbitrarily. The development of the two-phase boundary layer is not sensitive to the initialization value for the cross-stream length scale.

4.3.6 Results

In order to distinguish carrier phase internal effects from two-phase effects, the model assessment is subdivided into different sections: Changes in boundary layer thickness due to *momentum conservation within the carrier phase* are discussed in section 4.3.6.1. The influence of *carrier phase acceleration due to drag* with the dispersed phase is assessed in section 4.3.6.2. Moreover, the influence of *global carrier phase density* on spray penetration and boundary layer thickness is outlined in section 4.3.6.3. The temporal development of the two-phase boundary layer (ttBL) model is evaluated applying constant global thermodynamic conditions for the gas phase, i.e. constant carrier phase density during injection and constant temperature and pressure in the far field environment of the DSZ.

4.3.6.1 Transient *single* phase boundary layer (tBL)

In this section, the temporal development of the boundary layer length scale due to the *convective and diffusive terms* in equation (4.46) is investigated.

Several injection and boundary conditions are applied in order to explore different physical effects. Appropriate values for δ_τ at the injection outlet are given in section 4.3.5.

The model accurately describes a shear layer induced by a wall sud-
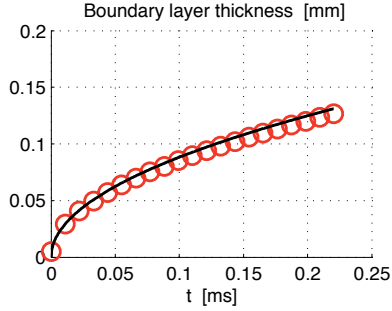
Figure 4.9: Temporal evolution of the boundary layer thickness of a wall suddenly set into motion; analytical (continuous line) and numerical solution from the ttBL model (circles)
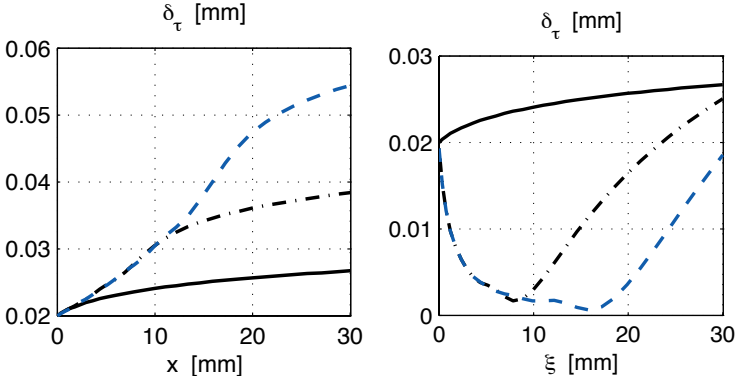

Figure 4.10: Single phase boundary layer evolution due to a fixed negative streamwise velocity gradient $\frac{\partial U_c}{\partial \xi} = -10^3 \; 1/s = const.$: plane 2D flow (left) and hollow cone flow (right); initial state at $t_0 = 0\,s$ (continuous line), intermediate state at $t_1 = \Delta t$ (dash-dotted line), and final state at $t_2 = 2 \cdot \Delta t$ (dashed line); $\Delta t = 110\,\mu s$

denly set into motion: Due to momentum diffusion, the initially very small boundary layer thickness grows (figure 4.9). The numerically obtained values reproduce the analytical solution from eq. (2.16). A single phase injection may not be described with the presented model since the shape of the assumed gas phase velocity profile is not an S shape.

In order to study the effect of the *carrier phase velocity gradient* on the local rate of change of boundary layer thickness, acceleration of the carrier phase due to drag with the dispersed phase is completely suppressed here: A temporarily constant carrier phase velocity field $U_c(t) = const.$ is applied (single phase boundary layer). Also, the "injection" boundary condition for the carrier phase boundary layer thickness is set constant: $\delta_\tau^{(inj)}(\xi = 0, t) = \delta_\tau^{(inj)}(x = 0, t) = const.$ At the right boundary, the Neumann boundary condition $\frac{\partial \delta_\tau(\xi = max)}{\partial \xi} = 0$ is applied. Note that cross-stream diffusion is also neglected here.

The boundary layer of a steady single phase jet is illustrated in fig-
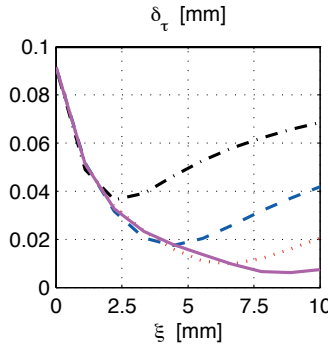
Figure 4.11: Hollow cone boundary layer thickness evolution in a constant velocity field $U_c = 100\,\text{m/s}$ starting from $\delta_\tau(t = 0) = 0.1\,\text{mm}$: Effect of the cone terms in equation (4.46); consecutive time steps of width $\Delta t = 28\,\mu\text{s}$

ure 4.10 for two successive instances in time starting from an initial flow state. The shape of the applied negative velocity gradient $\frac{\partial U_c}{\partial \xi} < 0$ corresponds to the widening of a single phase jet with increasing penetration depth (decrease of the cross-stream maximum velocity).

In the plane 2D case, the negative velocity gradient causes "transport"[††] of δ_τ towards the right and leads to local accumulation of δ_τ,
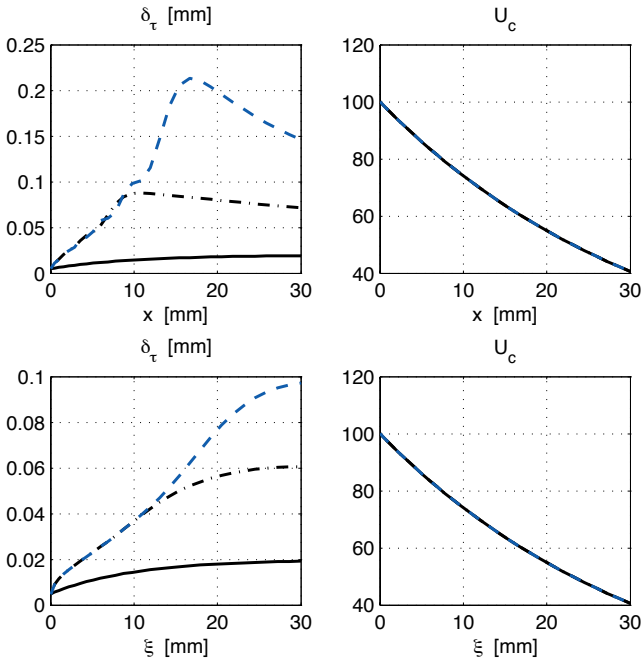
Figure 4.12: Boundary layer growth due to convection and diffusion: plane 2D flow (top) and hollow cone flow (bottom); consecutive time steps of width $\Delta t = 120\,\mu\text{s}$ (compare figure 4.10)

[††] Equation (4.46) describes the temporal rate of change due to convection and diffusion. Due to the averaging procedure applied while deriving the equation in section 4.3.3, the dependent variable δ_τ is *not conserved* and equation (4.46) does

e.g. at streamwise positions $x > 12\,\text{mm}$ at time t_2 (left plot in figure 4.10). In the region $x < 12\,\text{mm}$, the convective fluxes approximately cancel each other out ($|\frac{71}{20}\,\delta_\tau\,\frac{\partial U_c}{\partial \xi}| \approx |\frac{9}{10}\,U_c\,\frac{\partial \delta_\tau}{\partial \xi}|$) and consequentially, a local steady state $\frac{\partial \delta_\tau}{\partial t} = 0$ is reached.

For hollow cone flow, the plot of δ_τ in the right graph of figure 4.10 indicates that the cone terms in equation (4.46) cause a faster decrease in boundary layer thickness than the plane 2D case when the same velocity field is applied. The cone terms are particularly large in magnitude in the region close to the injection outlet ($\xi < 18\,\text{mm}$ at $t = t_2$), where $\xi \to 0$. Among the cone terms in equation (4.46), the term $(\frac{3}{4}\,\delta_\tau\,\frac{U_c}{\xi})$ is dominant because it is of the lowest order with respect to the cross-stream length scale δ_τ.

The contribution of the cone terms in equation (4.46) to the cross-stream length scale evolution for a conic 2D flow configuration is illustrated in figure 4.11. A constant gas velocity field $U_c(\xi, t) = 100\,\text{m/s}$ is applied. Starting from the global initial condition $\delta_\tau = 0.1\,\text{mm}$, the boundary layer thickness decreases in time. When a steady state is locally reached, the shape of the boundary layer thickness profile is proportional to $1/\xi$ (which is due to the portion of equation (4.46) termed "cone".

Up to now, diffusive growth of the boundary layer was suppressed. The contribution of the diffusive terms in equation (4.46) is presented in figure 4.12. The "injection" condition $\delta_\tau^{(inj)}(\xi = 0) = 5\,\mu\text{m}$ and the temporarily constant carrier phase velocity field $\frac{\partial U_c(t)}{\partial t} = const.$ are applied.

Strong diffusive fluxes occur due to the small boundary layer scale of order $\mathcal{O}(\delta_\tau) = 10$ to $100\,\mu\text{m}$. In the case of the hollow cone flow (bottom row of figure 4.12), they even outperform the local decrease of

---

not constitute a conservation equation for δ_τ. As a consequence, δ_τ is not transported in a conservative sense although obviously, δ_τ locally changes due to streamwise gradients in the flow direction.

δ_τ due to the radial terms in equation (4.46).

4.3.6.2 Transient *two-phase* boundary layer (ttBL)

In this section, the evolution of the cross-stream length scale due to the *two-phase* term in equation (4.46) resulting from carrier phase acceleration due to drag with the dispersed phase is investigated.

The initial and injection boundary conditions applied to the flow calculations presented in this section are listed in table 4.2 on page 128.

The dispersed phase mass is injected at $U_p^{(inj)} = 200\,\text{m/s}$ into initially quiescent air. The high slip velocities between both phases lead to strong momentum exchange. Consequentially, the carrier phase is accelerated and the injected dispersed phase is decelerated.
Due to the radial widening of the injected hollow cone sheet, the dispersed phase bulk density decreases with increasing penetration depth (increasing ξ). Because the particle velocity decreases along increas-
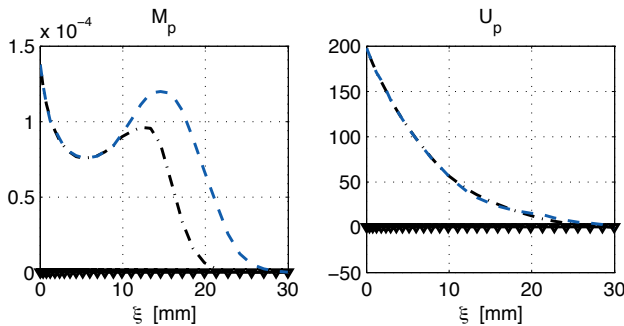
Figure 4.13: Evolution of dispersed phase mass (left) and velocity profiles (right) due to injection of a dispersed phase hollow cone sheet: flow states initially (triangles), at $t = 0.3\,\text{ms}$ (dash-dotted) and at $t = 0.5\,\text{ms}$ (dashed line); $p_c = 10\,\text{bar}$

ing ξ due to drag with the carrier phase, dispersed phase mass M_p is accumulated within the pressure chamber (figure 4.13 left).

The corresponding carrier phase profiles of boundary layer thickness δ_τ and velocity U_c are displayed in figure 4.14a. Inspite of the large density ratio $\rho_p/\rho_c \gg 1$, an acceleration of the carrier phase to values comparable to the dispersed phase velocity is prevented by the shear force acting on the carrier phase center line velocity, which is of the same order of magnitude as the inter-phase drag force (see figure 4.15[‡‡] and equation (4.25)).

When injected particles first accelerate the carrier phase, the initially broad carrier phase boundary layer shrinks considerably (figure 4.14a left). This is due to the acceleration term in equation (4.46). When carrier phase acceleration is not taken into account in equation (4.46), the boundary layer cross-stream length scale evolves as displayed in figure 4.14b (left): The positive velocity sign and the boundary condition $\delta_\tau^{(inj)}$ lead to a decrease close to the injection outlet ($\xi = 0$). The negative velocity gradient causes accumulation of δ_τ downstream of the injection outlet. And momentum diffusion initiates a small boundary layer growth in the region $20\,\text{mm} < \xi < 30\,\text{mm}$.

The injection induced two-phase flow states presented in this section indicate that the major part of the two-phase boundary layer is in a steady state flow condition as soon as the front of the injected dispersed phase has passed (as supported by the congruent profiles between the two presented flow states). Only the transported cross-stream length scale slightly increases after the spray front has passed (see e.g. figure 4.14a).

In figure 4.16, the liquid mass distribution during the injection process

---

[‡‡] Close to the injection outlet, the carrier phase velocity is prescribed by the boundary condition. Therefore the force equilibrium between drag and shear is not maintained here. So the mismatch at the injection position in figure 4.15 stems from the applied boundary condition.
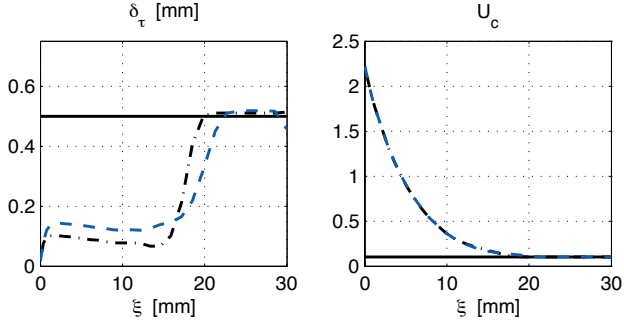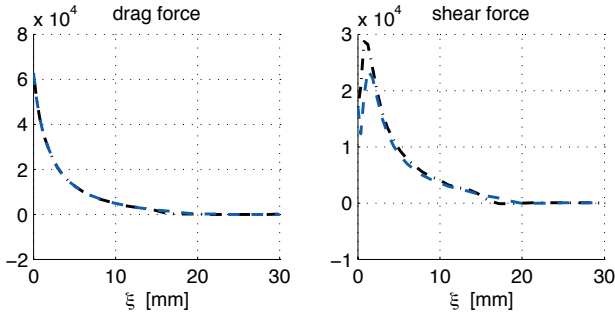
(a) with acceleration and cone terms
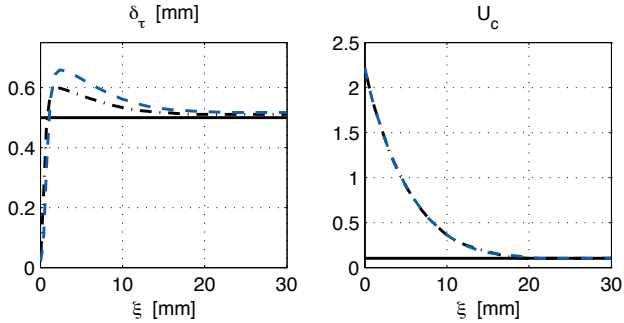
(b) without acceleration and with cone terms (corresponding to the dispersed phase profiles in figure 4.13)

Figure 4.14: Evolution of carrier phase boundary layer thickness field due to dispersed phase injection according to equation (4.46); $p_c = 10 \, \text{bar}$; $t = 0.3 \, \text{ms}$ (dash-dotted) and $0.5 \, \text{ms}$ (dashed line)

Figure 4.15: Evolution of drag and shear forces corresponding to the carrier phase flow states presented in figure 4.14a; $p_c = 10\,\text{bar}$; $t = 0.3\,\text{ms}$ (dash-dotted) and $0.5\,\text{ms}$ (dashed line)

resulting from the ttBL model is compared to the CFD results. The liquid volume fraction profiles both at the center line and the sector average are plotted along the injection direction. The profiles are nor-
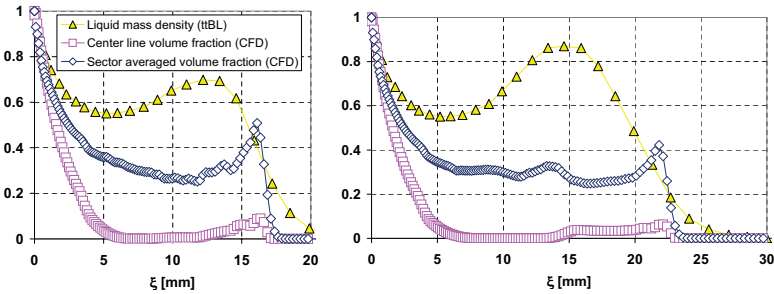
Figure 4.16: Comparison of CFD and ttBL model results: Normalized distribution of liquid mass density (triangles) according to figure 4.13, sector averaged volume fraction (diamonds) according to figure 4.5 and center line volume fraction (squares) according to figure 3.10 along the main injection direction ξ; $p_c = 10\,\text{bar}$; flow states at $t = 0.3\,\text{ms}$ (left) and $t = 0.5\,\text{ms}$ (right)

malized to their inlet value.

The penetration depth as the primary measure for the cold two-phase flow is predicted accurately by the ttBL model although the maximum gradient at the spray front is not as well captured as in the CFD case. Within the spray, more liquid mass accumulation may be observed with the ttBL model. The flatter profiles resulting from CFD are caused by the induced secondary vortices outside the dense spray zone, which support streamwise transport of liquid mass. This effect is not contained in the ttBL model.

4.3.6.3 Chamber pressure dependence

When the engine is operated in stratified mode, fuel is injected late during the compression stroke. Consequently, the injection induced two-phase flow experiences varying global thermodynamic conditions. Therefore, the behavior of the ttBL model at different (constant) levels of gas phase density is studied in this section.

The penetration behavior of the hollow cone fuel jet was measured experimentally at constant chamber temperature $T_{cyl} = 300\,\mathrm{K}$ at different pressure levels (see section 3.2.1 [98]). For these pressure levels, the flow states resulting from the ttBL model are displayed in figure 4.17. With increasing pressure, the penetration length of fuel decreases and consequently, a shorter streamwise portion of the carrier phase boundary layer is affected by the injection.

Because of the increased carrier phase density, momentum exchange is more intense per unit volume: The gas phase is able to take on higher amounts of momentum from the dispersed phase. As a consequence, the maximum equilibrium carrier phase velocities close to the injection outlet increase with increasing pressure. Note that among the forces acting on the gas phase, the inertial force is much smaller than the shear and drag forces during injection and thus negligible.
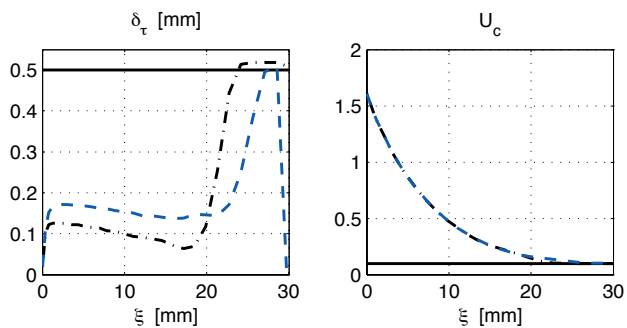
(a) $p_c = 6\,\mathrm{bar}$
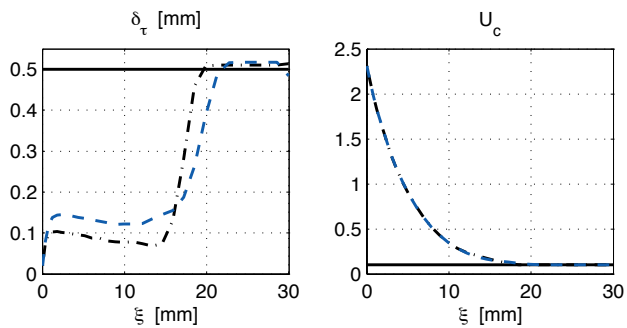
(b) $p_c = 10\,\mathrm{bar}$
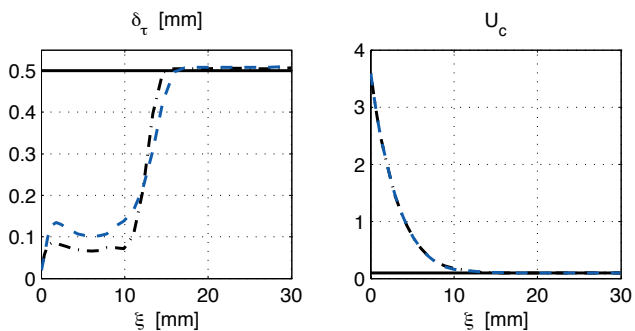
(c) $p_c = 20\,\mathrm{bar}$

Figure 4.17: Carrier phase cross-stream length scale and velocity fields depending on carrier phase pressure

4.4 Evaporation

In the previous section, the concept of a transient two-phase boundary layer (ttBL) was applied to a cold flow which results from injection of liquid fuel into air. The model was validated against experimental data of hollow cone injection process in cold conditions with negligible evaporating fuel mass.

The accuracy of the ttBL model describing cold transient two-phase flows (section 4.3) suggests to apply the concept also to evaporation. Neither experimental nor computational data of the hot transient two-phase boundary layer and the resulting evaporating mass flux are available for the hollow cone injection process. Nevertheless, the ttBL model theory for heat exchange and fuel species diffusion across the transient boundary layer is presented here and the plausibility of model results is assessed.
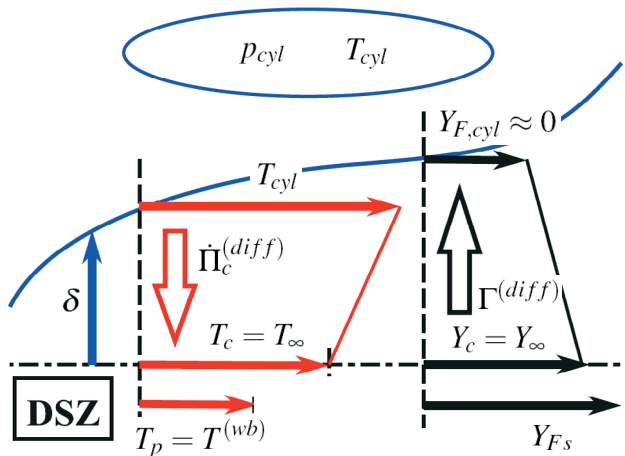
Figure 4.18: Diffusive transport of heat and fuel vapor mass across the DSZ boundary layer; sketch

Consider a boundary layer of thickness δ resulting from injection of liquid fuel into a combustion chamber according to figure 4.18:

The evaporation of the injected liquid fuel is determined by the average thermodynamic state of the gas within the cylinder (p_{cyl} and T_{cyl}). Across the DSZ boundary layer, both heat and fuel vapor mass are transported diffusively normal to the main injection direction. For the diffusive heat flux $\Pi_c^{(diff)}$, the driving potential is defined by the temperature difference between the mean gas temperature within the cylinder T_{cyl} and the gas phase temperature at the DSZ T_c. This temperature T_c is modeled to be identical to the far field temperature T_∞, which defines the diffusive transport of fuel species mass away from the saturated liquid droplet surface in Spalding's evaporation model. The liquid droplet temperature T_p equals the wet bulb temperature $T^{(wb)}$.

In the same manner, the diffusive mass flux $\Gamma^{(diff)}$ of fuel species mass across the boundary layer is approximated. The species concentration Y_c at the DSZ is again modeled to equal the far field species concentration Y_∞ at the droplet level. Fuel species diffusion across the DSZ boundary layer is defined by the difference between the average fuel vapor species concentration $Y_{F,cyl}$ within the cylinder and the fuel species mass fraction Y_c within the DSZ. Y_{Fs} is the saturated film mass fraction at the droplet surface. In this section, the cylinder thermodynamic state is kept constant and the average fuel species concentration within the cylinder $Y_{F,cyl}$ is assumed to be zero (i.e. the mass of air contained in the cylinder reservoir is assumed to be much larger than the injected fuel mass).

Fuel mass fraction transport & saturation state

Since the specific carrier phase mass within the DSZ is equal to the specific gas phase mass at the DSZ interface $\rho_c^{(DSZ)}$, the volume specific fuel vapor mass M_F within the DSZ carrier phase mass is defined

by the fuel species mass fraction

$$Y_F = \frac{M_F}{\rho_c^{(DSZ)}} \ .$$

(4.55)

The conservation of fuel vapor mass M_F is accounted for by a transport equation for the average fuel mass fraction Y_F adjacent to DSZ:

$$\frac{\partial Y_F}{\partial t} + \frac{\partial (Y_F U_c)}{\partial \xi} + \frac{Y_F U_c}{\xi} = \frac{1}{\rho_c^{(DSZ)}} \underbrace{\left(\Gamma^{(evap)} - 2 \cdot \Gamma^{(diff)} \right)}_{\Gamma^{(net)}} \ .$$

(4.56)

Note that the gas phase density within the dense spray zone $\rho_c^{(DSZ)}$ was assumed to be constant (see section 4.3.3). The factor in the RHS denominator accounts for the fact that the DSZ is surrounded by two adjacent carrier phase boundary layers.

According to the physics of evaporating isolated droplets and droplet clouds discussed in detail section 3.1.3, the source term $\Gamma^{(evap)}$ in eq. (4.56) accounting for evaporating of fuel mass is derived from the flow rate of evaporating fuel mass at the surface of an isolated droplet

$$\Gamma_{iso}^{(evap)} = -\rho_p \frac{\partial (\frac{\pi}{6} D_p^3)}{\partial t} = \frac{\pi}{4} \rho_p D_p \beta_{Spald} \ .$$

(3.18)

According to eq. (3.19), the mass flow rate $\Gamma^{(evap)}$ of N_p evaporating dispersed particles per unit volume is

$$\Gamma^{(evap)} = -\rho_p \frac{\partial \alpha_p}{\partial t} = \frac{3}{2} \frac{\beta_{Spald}}{D_p^2} M_p$$

(4.57)

where $\beta_{Spald} = 8 \frac{\rho_{Fs}}{\rho_p} \mathscr{D}_{Fs} \ln(1 + B_M)$ and $B_M = (Y_{Fs} - Y_F)/(1 - Y_{Fs})$. The saturation fuel vapor mass fraction is calculated from the partial pressure p_s of saturated fuel vapor mixture, which is obtained from

the Clausius-Clapeyron relation

$$Y_{Fs} = \frac{p_s M_s}{p_s M_s + (p_c - p_s)\rho_c^{(DSZ)}} \text{ and } p_s = p_{ref} \cdot \exp\left\{ \frac{\Delta h_v}{R_s} \left(\frac{1}{T_{ref}} - \frac{1}{T_p} \right) \right\} .$$
$$(3.17)$$

The source term $\Gamma^{(diff)}$ in eq. (4.56) accounts for the gross diffusive fuel vapor mass flux $\dot{M}_{F_\eta}$ normal to the main injection direction. For its approximation it is assumed that outside of the DSZ region, the fuel mass concentration is close to zero ($Y_{F\infty} = 0$) and that the density

$$\Gamma_F^{(diff)} = -\rho_c^{(DSZ)} \, \mathscr{D}_F \, \frac{\partial Y_F}{\partial \eta} \approx \rho_c^{(DSZ)} \, \mathscr{D}_F \, \frac{Y_F - Y_{F,cyl}}{\delta_\tau^{(spec)}} . \qquad (4.58)$$

The length scale $\delta_\tau^{(spec)}$ characterizing the cross-stream species gradient is assumed to be proportional to the momentum diffusion length scale δ_τ. The proportionality is approximated by means of the Schmidt number

$$\text{Sc} = \frac{\nu_c}{\mathscr{D}_F} \approx \frac{\delta_\tau}{\delta_\tau^{(spec)}} , \qquad (4.59)$$

so that the species diffusion source term is

$$\Gamma_F^{(diff)} \approx \rho_c^{(DSZ)} \, \text{Sc} \, \mathscr{D}_F \, \frac{Y_F - Y_{F,cyl}}{\delta_\tau} . \qquad (4.60)$$

The evaporating mass flow rate is limited by both the saturation state and the fuel species diffusion across the boundary layer. Therefore, the maximum source term for the effective fuel vapor mass flux is defined as

$$\Gamma^{(eff)} = \min \left\{ \Gamma^{(evap)} \quad ; \quad 2\,\Gamma_F^{(diff)} \right\} . \qquad (4.61)$$

The factor "2" stems from the fact that the hollow cone sheet is exposed to two adjacent boundary layers.

Energy conservation

The temperatures of both phases have to be estimated by the conservation of the volume specific internal energy ($e = \rho\, c_v\, T$)

$$\frac{\partial e}{\partial t} + \frac{\partial (e\, u)}{\partial \xi} + \frac{e\, u}{\xi} = -\frac{\partial}{\partial \xi}\left(\lambda_c\, \frac{\partial T}{\partial \xi}\right) + \Pi_e\,, \qquad (4.62)$$

with the source term Π_e accounting for energy consumption during evaporation. Because of the dominant convective effects occurring within the DSZ during the injection process, the streamwise diffusion of thermal energy is neglected. Also the thermal energy production due to viscous dissipation is assumed to be small and neglected in the following. Thus, if the heat capacities are assumed to be constant, the dispersed phase energy conservation equation reduces to a simple convection-diffusion equation for the temperature

$$\frac{\partial (M_p\, T_p)}{\partial t} + \frac{\partial (M_p\, T_p\, U_p)}{\partial \xi} + \frac{M_p\, T_p\, U_p}{\xi} = \frac{\Pi_p}{C_p}\,, \qquad (4.63)$$

The carrier phase energy conservation equation incorporates the temperature diffusive energy flux due to the difference between the DSZ (T_c) and the undisturbed cylinder environment (T_{cyl})

$$\frac{\partial T_c}{\partial t} + \frac{\partial (T_c\, U_c)}{\partial \xi} + \frac{T_c\, U_c}{\xi} = \frac{1}{\rho_c^{(DSZ)}\, C_{v,c}}\left(2\cdot \Pi_c^{(diff)} - \Pi_p\right)\,. \quad (4.64)$$

The heat instantaneously consumed from the evaporating mass flux $\Gamma^{(evap)}$ is

$$\Pi_p = \Gamma^{(evap)}\, \Delta h_v\,. \qquad (4.65)$$

The cross-stream diffusion flux of carrier phase energy close to the DSZ is approximated from the difference in carrier phase temperature

between the DSZ T_c and the reservoir outside of the DSZ T_{cyl}:

$$\Pi_c^{(diff)} = \lambda_c^{(eff)} \frac{\partial T_c}{\partial \eta} \approx \lambda_c^{(eff)} \frac{T_{cyl} - T_c}{\delta_\tau^{(th)}} \, . \tag{4.66}$$

The temperature gradient at the DSZ boundary is approximated by the thermal length scale $\delta_\tau^{(th)}$

$$\frac{\partial T_c}{\partial \eta} \approx \frac{T_{cyl} - T_c}{\delta_\tau^{(th)}} \, . \tag{4.67}$$

The thermal length scale $\delta_\tau^{(th)}$ characterizes the cross-stream temperature gradient. It is modeled to be proportional to the velocity gradient length scale δ_τ. As proportionality factor between the two length scales δ_τ and $\delta_\tau^{(th)}$, the proportionality between the diffusion coefficients of momentum v_c and thermal energy λ_c may be expressed by means of the Prandtl number

$$\text{Pr} = \frac{\rho_c \, C_p \, v_c}{\lambda_c} \approx \frac{\delta_\tau}{\delta_\tau^{(th)}} \, , \tag{4.68}$$

so that the diffusion source term reads

$$\Pi_c^{(diff)} \approx \text{Pr} \, \lambda_c^{(eff)} \frac{T_{cyl} - T_c}{\delta_\tau} \, . \tag{4.69}$$

Flux analysis and physical simplifications

In the following, the orders of magnitude of the source terms accounting for the conservation of species ($\Gamma^{(evap)}$ and $\Gamma_F^{(diff)}$) and energy ($\Pi_c^{(diff)}$ and Π_p) are assessed.

Starting from the fully transient description of the droplet heat-up and evaporation process, the dilute spray assumption is shortly discussed, and a third way accounting for the dense spray modeling approach is

presented.

If the complete transient behavior of the two-phase system is to be described, the energy exchange at the droplet surface has to be resolved [116]. Then, the heat transfer rate towards an isolated droplet

$$\dot{Q}_{HE}^{(iso)} = \frac{Nu\,\lambda}{D_p} \; \underbrace{\pi D_p^2 (T_c - T_p)}_{A_p}$$

leads to the total volume specific heat transfer rate (utilizing $M_p = N_p \frac{\pi}{6} D_p^3$)[§§]

$$\dot{Q}_{HE} = \dot{Q}_{HE}^{(iso)} \, N_p = \frac{6\,M_p\,Nu\,\lambda}{\rho_p D_p^2} \, (T_c - T_p) \; .$$

Because the specific enthalpy of liquid fuel is much smaller than its specific latent heat, the droplet heat-up process occurs much faster than the total evaporation process [73]. So for the total evaporation process, a thermal equilibrium within the DSZ may be assumed and transients in the heat transfer at the droplet surface are therefore neglected. If the two-phase mixture is locally in thermal equilibrium, the similarity assumption between heat and mass diffusion at the droplet surface is valid so that the temperature difference between both phases is given by the fuel vapor mass diffusion potential at the droplet sur-

---

[§§] For the non-dimensional heat transfer coefficient (Nusselt number) at the droplet surface, experimental correlations of spheres exposed to forced convective flow have been derived. For the present approximation, a simplified heat transfer law is adopted [99]:

$$Nu = 2 + \left(0.4\,Re_p^{\frac{1}{2}} + 0.06\,Re_p^{\frac{2}{3}} \right) \, Pr_c^{\frac{2}{5}} \; . \tag{4.70}$$

The carrier phase Prandtl number is set to $Pr_c = 0.7$.

face (see section 3.1.3)

$$T^{(wb)} = T_p = T_c - \frac{\Delta h_v}{C_v} B_M \ . \tag{3.22}$$

The amount at which the temperature of one phase is affected by evaporation process depends on the ratio of enthalpy densities $(\overline{\rho}_p C_p/(\overline{\rho}_c C_v)$ between dispersed and carrier phase. Since generally $C_p/C_v \ll \overline{\rho}_p/\overline{\rho}_c$, the mass density ratio $\overline{\rho}_p/\overline{\rho}_c$ is more relevant than the ratio of specific heats.

If e.g. the evaporation at the surface of an isolated droplet is investigated ($\overline{\rho}_p/\overline{\rho}_c \ll 1$, *"dilute spray assumption"*), the temperature change in the carrier phase environment may be assumed to be smaller than the temperature change of the droplet (corresponding to a comparatively big carrier phase internal energy capacity $\overline{\rho}_c C_v$ around the droplet). In that case, the carrier phase temperature far away from the droplet surface is assumed to be constant ($T_c = T_\infty = const.$, $\frac{\partial T_c}{\partial t} = 0$) and the mass diffusion potential (eq. (3.22)) defines the dispersed phase temperature T_p.

By contrast, a local mass loading $\overline{\rho}_p/\overline{\rho}_c \gg 1$ is observed within the DSZ (*"dense spray assumption"*). So the dispersed phase experiences a negligible temperature change ($T_p = T^{(wb)} = const.$, $\frac{\partial T_p}{\partial t} = 0$) and the mass diffusion potential (eq. (3.22)) defines the resulting carrier phase temperature T_c within the DSZ. This approach is adopted in the coarse of this work.

Peclet model

The temporal development of the carrier phase temperature adjacent to the DSZ depends on the ratio of the convective energy flux within the DSZ $\dot{E}^{(conv)}$ along the main injection direction ξ and the diffusive energy flux $\Pi_c^{(diff)}$ normal to the main injection direction. The

streamwise convective energy flux adjacent to the DSZ

$$\dot{E}^{(conv)} = \dot{I}_c \, C_{v,c} \, T_c = \rho_c \, U_c \, C_{v,c} \, T_c \tag{4.71}$$

corresponds to the carrier phase momentum flux $\dot{I}_c = \rho_c \, U_c$. The ratio of the area specific energy fluxes resulting from diffusion $\Pi_c^{(diff)}$ and convection $\dot{E}^{(conv)}$ is identified as a Peclet number for the carrier phase mass adjacent to the DSZ

$$Pe_\Pi = \frac{\dot{E}^{(conv)}}{\Pi_c^{(diff)}} = \frac{\delta_\tau \, \rho_c \, U_c \, C_{v,c}}{\lambda_c^{(eff)}} \, \frac{T_c}{T_{cyl} - T_c} \; . \tag{4.72}$$

Consider the limiting cases for a given temperature difference $(T_{cyl} - T_c) > 0$ and finite material properties $(C_{v,c})$. At finite flow properties $(\lambda_c^{(eff)})$, $Pe_\Pi \to 0$ for $U_c \to \infty$ (dominance of convective heat transfer). On the other hand at limited U_c and effective thermal diffusivity $\lambda_c^{(eff)} \to \infty$, $Pe_\Pi \to \infty$ (dominance of diffusive heat transfer). The effective thermal diffusion coefficient subsumes the effects of thermal diffusivity and mean convective transport due to turbulent fluctuations within the carrier phase adjacent to the DSZ.

$$\lambda_c^{(eff)} = \lambda_c + \rho_c \, C_{v,c} \, \nu_T \tag{4.73}$$

When the temporal development of dispersed phase temperature is characterized by small time scales, which are not intended to be resolved by the numerical integration scheme, the carrier phase temperature msy be modeled to result from the local ratio between convective and diffusive energy fluxes within the carrier phase as quantified by the

local carrier phase Peclet number (eq. (4.72)) [¶¶]

$$\frac{T_c - T_c^{(0)}}{T_{cyl} - T_c^{(0)}} = \frac{1}{1 + Pe_\Pi} \qquad \text{with} \qquad T_c^{(0)} = T^{(wb)} + \frac{\Delta h_v}{C_{v,c}} B_M \quad (4.74)$$

The original carrier phase temperature $T_c^{(0)}$ is the (apparent) carrier phase environment temperature corresponding to the current local saturation state within the DSZ in the case of zero convection (with the wet bulb temperature $T^{(wb)} = T_p$). Depending on the carrier phase Peclet number, T_c varies between $T_c^{(0)}$ (dominance of the heat and mass transfer equilibrium around the dispersed phase droplets, $Pe_c \rightarrow \infty$) and T_{cyl} (dominance of carrier phase energy convection adjacent to the DSZ, $Pe_c \rightarrow 0$).

The energy source term accounts for the gain due to the dispersed phase temperature change and the loss due to evaporating mass.

$$\Pi_p = M_p \, C_p \left(\frac{\partial T_p}{\partial t} \right)^{(HE)} - \Gamma^{(evap)} \, C_p \, T_p \qquad (4.75)$$

The carrier phase has to compensate both the dispersed phase temperature change and the latent heat of the evaporating dispersed phase

---

[¶¶] The utilization of a Peclet number to approximate the contribution of convective and diffusive fluxes can also be applied to the fuel species transport:

$$Pe_\Gamma = \frac{\dot{m}^{(conv)}}{\Gamma^{(diff)}} \approx \frac{U_c}{\mathscr{D}_F} \frac{\delta_\tau}{Y_F - Y_{F,cyl}}$$

with

$$\frac{Y_F - Y_F^{(0)}}{Y_{F,cyl} - Y_F^{(0)}} = \frac{1}{1 + Pe_\Gamma} \, .$$

mass flux $\Gamma^{(evap)}$.

$$\Pi_c = \rho_c^{(DSZ)} \, C_{v,c} \, \left(\frac{\partial T_c}{\partial t} \right)^{(HE)} - M_p \, C_p \, \left(\frac{\partial T_p}{\partial t} \right)^{(HE)} - \Gamma^{(evap)} \, \Delta h_v$$
(4.76)

This approach provides an alternative to the estimation of the carrier phase temperature T_c within the DSZ. Nevertheless, the dense spray assumption presented above is utilized in the following results section.

Results

In the following, the treatment of evaporation within the transient two-phase boundary layer (ttBL) model proposed above is assessed.

In a two-phase boundary layer, the diffusive rate of heat transfer towards and of evaporating fuel vapor species away from the jet center is dominated by the characteristic cross-stream length scale. During injection, the cross-stream length scale is predominantly the result of momentum exchange between both phases and consequential (excess) entrainment of carrier phase from the far field towards the jet center. By contrast, the influence of the magnitude of the energy and mass fluxes across the boundary layer on the development of the boundary layer thickness is smaller than the influence of the boundary layer thickness on the cross-stream diffusion fluxes. As a result, the interaction of streamwise momentum transport with mass and energy cross-stream transfer may be characterized as a one-way coupled system: Momentum exchange does influence the evaporation process, and the influence of evaporation on the local rates of momentum exchange is negligible. For this reason, transient droplet cloud heat-up and evaporation within the injection induced boundary layer is the focus of this section, while the reverse mechanism is neglected.

The transient response of liquid phase temperature and fuel vapor mass fraction (equations (4.56) and (4.63)) to the cross-stream diffusion fluxes is studied in the following. In order to separate the

diffusion contribution from fluxes due to temporal variations in the cross-stream length scale (which are primarily caused by injection induced momentum exchange), a constant streamwise profile of the cross-stream length scale

$$\delta_\tau(x,t) = 0.1\,\text{mm} + 0.002 \cdot x \qquad \text{and} \qquad U_c(x,t) = 100\,\text{m/s} \quad (4.77)$$

is assumed. The initial conditions for the temperatures of both phases and the fuel species mass fraction are

$$t = 0: \ T_p(t=0) = 20\,°\text{C}\,, \ T_c = T_c^\infty(x,t) = 300\,°\text{C}\,, \text{ and } Y_F = 0\,. \tag{4.78}$$

Figure 4.19 shows streamwise temperature profiles during evaporation due to thermal diffusion from the comparatively warm "cylinder infinity" environment towards the dense spray zone (DSZ). The saturation state at the liquid surface is defined by the dispersed phase temperature (infinite liquid conductivity model). Because of the zero gas phase capacity within the DSZ, the temperature T_c instantaneously decreases to the corresponding gas phase equilibrium temperature. Because of the large temperature difference between liquid phase and the environment (and the small cross-stream length scale which characterizes the temperature gradient), thermal energy is transfered towards the DSZ and the liquid phase starts warming up (figure 4.19a). The streamwise gradient in the cross-stream length scale profile causes the energy flux to be comparatively large in areas of small cross-stream length scale, i.e. for $x \to 0$.

As the liquid phase warms up, an equilibrium between thermal energy diffusion across the boundary layer and the evaporation process is approached (figure 4.19b): At this thermodynamic state, the energy flux diffusively transported towards the DSZ is equal to the latent heat flux consumed by the evaporating mass flux (which is again defined by the liquid phase temperature). Note that this state is dominated by the "cylinder infinity" temperature T_c^∞ and the influence of stream-

wise gradients within the DSZ on the streamwise temperature profiles ceases.
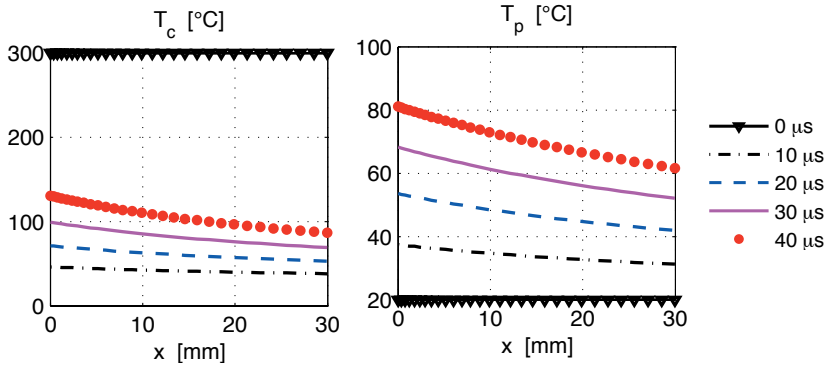

(a) Early development
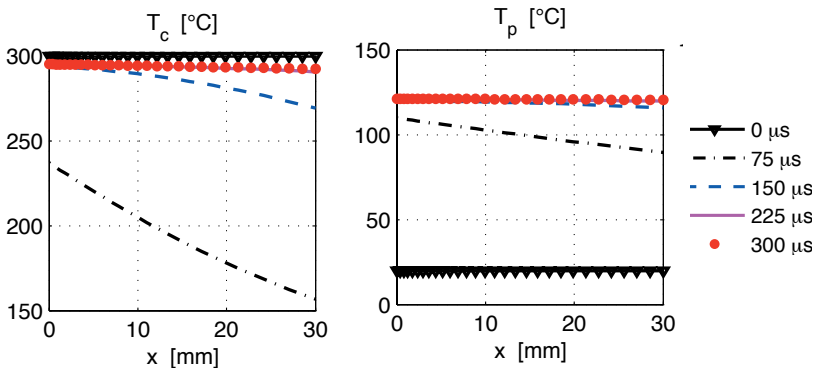
(b) Late development

Figure 4.19: Transient liquid phase warm-up and evaporation due to *thermal diffusion within the gas phase boundary layer*: carrier phase temperature (left) and liquid phase temperature (right); $p_g = 10\,\text{bar}$

Figure 4.20 gives profiles of the saturation state and fuel species mass fraction corresponding to the temperature profiles in figure 4.19b. Because of the exponential rise of the saturation pressure with the saturation (liquid phase) temperature, evaporation is slow during the first period of $\Delta t = 75\,\mu s$. The maximum evaporation rate is defined by the (maximum) saturation temperature which again depends on the global gas phase temperature .

In figure 4.21, the evaporation process from the same initial conditions but at a decreases cylinder pressure of $p_{cyl} = 1\,bar$ is depicted. In comparison to the two states presented in figures 4.19 and 4.20 ($p_{cyl} = 10\,bar$), the liquid phase warm-up is in an intermediate state after $300\,\mu s$: The temperature difference between liquid and carrier phase is larger because of the increased Spalding diffusion potential around the droplets. Even though the steady state saturated fuel vapor species mass fraction at the decreased global pressure is increased and the reached levels of $Y_f(t = 300\,\mu s)$ at both global pressures are comparable, the total evaporating mass flux is smaller at the lower pressure
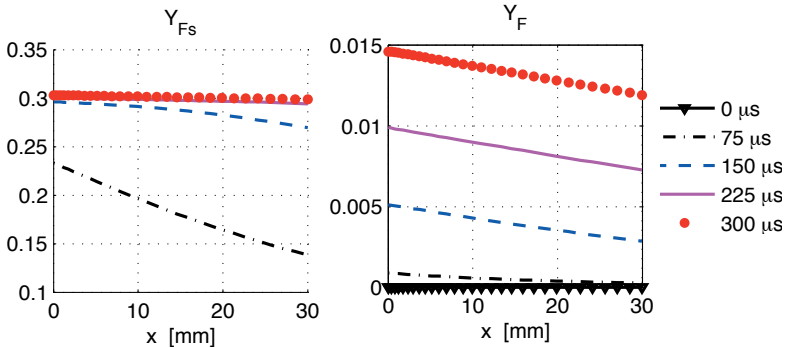
Figure 4.20: Resulting fuel species mass fractions of the saturated vapor Y_{Fs} (left) and DSZ mean Y_F (right) during liquid phase warm-up and evaporation according to figure 4.19 (no species diffusion); $p_g = 10\,bar$

level.

When thermal diffusion is neglected, the liquid phase temperature cannot increase. The consequentially slow evaporation process leads to low levels fuel species mass fraction within the time period of $300\,\mu s$. The effect of the prescribed cross-stream length scale profile

(a) Liquid phase (left) and gas phase temperatures (right)

(b) Saturation (left) and current fuel vapor species mass fraction (right)
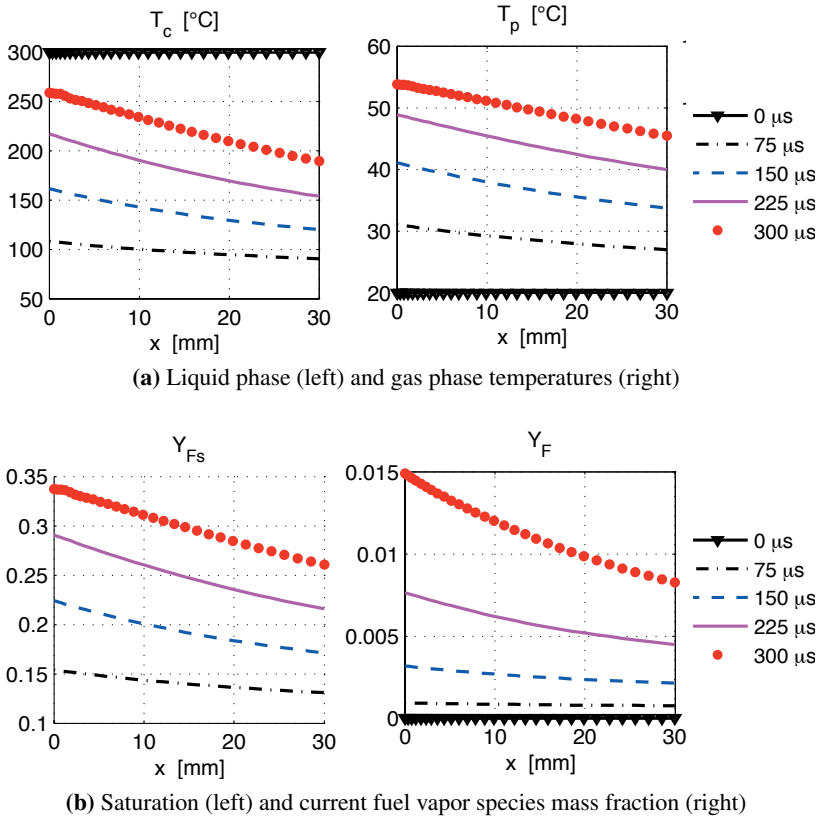
Figure 4.21: Transient liquid phase warm-up due to *thermal diffusion at a lower gas pressure level* of $p_g = 1\,\text{bar}$ (no species diffusion)

on species diffusion is nevertheless visible from figure 4.22: A smaller cross-stream length scale leads to increased cross-stream diffusion of fuel vapor species and consequentially to lower levels of species mass fraction within the DSZ.
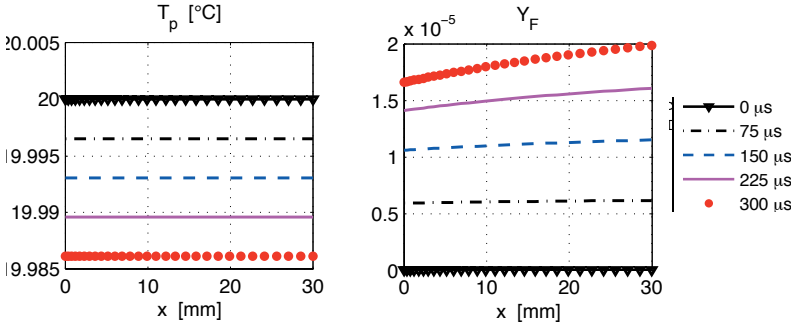
Figure 4.22: Liquid phase temperature T_p (left) and fuel vapor species mass fraction Y_F (right) during evaporation and due to *fuel vapor species diffusion* (no thermal diffusion); $p_g = 10\,\mathrm{bar}$
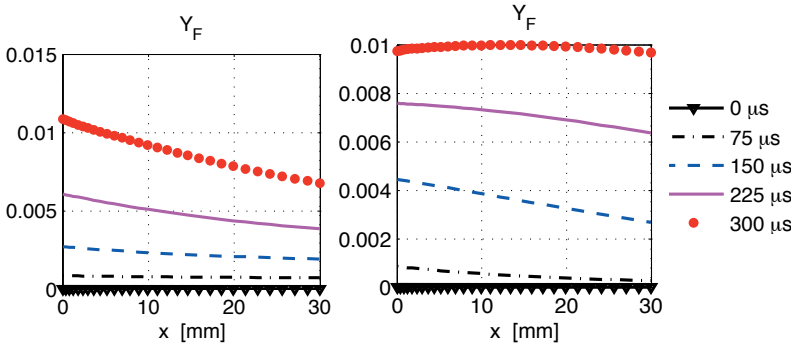
Figure 4.23: Fuel vapor species mass fraction Y_F during evaporation due to *both thermal and species diffusion*: at gas pressure levels $p_g = 1\,\mathrm{bar}$ (left) and $p_g = 10\,\mathrm{bar}$ (right)

Allowing both thermal and species cross-stream diffusion results in the fuel species streamwise profiles presented in figure 4.23: For both global pressure levels, the additional effect of fuel species diffusion reduces the values of Y_F at $t = 300\,\mu s$ and $x \approx 0$ from $Y_F \approx 0.015$ by about 30%.

4.5 Turbulence

Because the local cross-stream gradient of the carrier phase velocity is considered to have a major influence on the overall penetration behavior of the hollow cone spray (section 4.3.2), also cross-stream diffusion of streamwise momentum due to turbulent fluctuations has to be expected to increase cross-stream transport.

Close to the injector, the local boundary layer thickness should be of the order of the injector exit cross-section length scale. Due to the initially small boundary layer thickness, the boundary layer flow is likely to be laminar at the injection outlet.*** On the other hand, the presence of small liquid droplets introduces disturbances to the carrier phase flow and may promote the onset of turbulence.

If turbulent fluctuations do first occur, their intensity is heavily promoted by the strong cross-stream gradients within the mean carrier phase velocity profile. Because the mean diffusive effect of turbulence is orders of magnitude larger than the molecular viscosity and cross-stream diffusion of streamwise momentum is considered in the present model (see section 4.3), a simple turbulence model is incorporated.

Recall that according to the *turbulent gradient diffusion hypothesis*, the diffusive flux

$$\langle u_j \Phi \rangle = -\mathscr{D}_T \frac{\partial \langle \Phi \rangle}{\partial x_j} \tag{4.79}$$

due to fluctuations of the scalar quantity Φ is approximated [93]. In

---

***For example at a maximum injector exit speed of $200\,\mathrm{m/s}$ and a maximum injector opening half width of about $15\mu m$, only a Reynolds number of the order of $1.5 \cdot 10^5$ is reached.

the Reynolds averaged momentum equation

$$\frac{\overline{D}\,\langle U_i\rangle}{\overline{Dt}} = \frac{\partial}{\partial x_j}\left[-\frac{1}{\rho}\,\langle p\rangle\,\delta_{ij} + \frac{\mu}{\rho}\overline{S}_{ij} - \langle u_i u_j\rangle\right]$$

$$\text{with}\quad \overline{S}_{ij} = \frac{1}{2}\left(\frac{\partial\langle U_i\rangle}{\partial x_j} + \frac{\partial\langle U_j\rangle}{\partial x_i}\right) \tag{4.80}$$

an additional term resulting from the fluctuating velocity component – the Reynolds stress tensor $\langle u_i u_j\rangle$ – occurs. The *turbulent viscosity hypothesis* states that the deviatoric stress due to turbulent fluctuations (the anisotropic part of the Reynolds stress tensor $\langle u_i u_j\rangle$) is determined by the local mean rate of strain in terms of a linear relation [124]:

$$-\langle u_i u_j\rangle + \frac{2}{3}\,k\,\delta_{ij} = 2\,\nu_T\,\overline{S}_{ij}\,. \tag{4.81}$$

The turbulent viscosity (or turbulent exchange coefficient for momentum) is determined by a combination of a characteristic length $\mathscr{L}_T$ and velocity $\mathscr{U}_T$:

$$\nu_T = \mathscr{L}_T\,\mathscr{U}_T\,. \tag{4.82}$$

In the context of large eddy simulation, Smagorinski [117] models the transport of turbulent eddies which are not spatially resolved by means of a sub-grid turbulent viscosity

$$\nu_T^{(SG)} = l_m^2\,\sqrt{2\,\overline{S}_{ij}^2}\,. \tag{4.83}$$

The maximum length scale which may locally occur and not be spatially resolved is defined by the local filter width Δ characterizing the grid cell size

$$l_m = C_{Smag}\,\Delta\,. \tag{4.84}$$

This is identical to the application of a mixing length model (zero

equation turbulence model).

$$v_T = l_m^2 \left| \frac{\partial U}{\partial y} \right| \tag{4.85}$$

In the context of the presented boundary layer model, the local gradient could be approximated by the length scale $\mathscr{L}_T = l_m = \delta_\tau$ and the velocity scale $\mathscr{U}_T = \tilde{U}_c$, so that the turbulent viscosity would be

$$v_T = \delta_\tau \, \tilde{U}_c \tag{4.86}$$

and the rate of change of local boundary layer thickness due to turbulent viscosity

$$\left(\frac{\partial \delta_\tau}{\partial t} \right)_T = \frac{v_T}{\delta_\tau} \tag{4.87}$$

would simply come out to be $\left(\frac{\partial \delta_\tau}{\partial t} \right)_T = \tilde{U}_c$: Due to turbulent fluctuations, the temporal change of the boundary layer thickness δ_τ would be of the order of the streamwise convective velocity. This is a simple but too simplifying description of turbulent diffusivity effect since the turbulent diffusion would be over-estimated.

More detail is introduced by applying a one-equation turbulence model and solving a transport equation for the turbulent kinetic energy k [93].

$$k = \frac{1}{2} \langle u_i u_i \rangle \tag{4.88}$$

$$\frac{\partial k}{\partial t} + \frac{\partial (k \, u_j)}{\partial x_j} = \frac{\partial}{\partial x_j} \left(\frac{v_T}{Pr_T} \frac{\partial k}{\partial x_j} \right) + \mathscr{P}_k - \varepsilon_k \tag{4.89}$$

In only one spatial dimension (ξ) and cone coordinates, the conserva-

tion equation at the presumed spray center line reads

$$\frac{\partial k}{\partial t} + \frac{\partial (k\,U_c)}{\partial \xi} + \frac{k\,U_c}{\xi} = \underbrace{\frac{\partial}{\partial \xi}\left(\frac{\nu_T}{Pr_T}\frac{\partial k}{\partial \xi}\right)}_{\Pi_{\nu_T}} + \mathscr{P}_k - \varepsilon_k \,. \qquad (4.90)$$

The turbulent viscosity ν_T, the shear induced rates of production $\mathscr{P}_k$ and dissipation ε_k are quantified with appropriate model constants stemming from experiments [93] (see table 4.3).

$$\nu_T = C_\mu \frac{k^2}{\varepsilon} = c_t\,l_m\,k^{1/2} \qquad (4.91)$$

$$\mathscr{P}_k = \nu_T \left(\frac{\partial U}{\partial \eta}\right)^2 \qquad (4.92)$$

$$\varepsilon_k = \frac{C_\mu\,k^{3/2}}{c_t\,l_m} \qquad (4.93)$$

The length scale l_m (which is intrinsic to the one-equation model described above and fixes the ratio of the level of turbulent kinetic energy and its dissipation rate)

$$l_m = \frac{C_\mu}{c_t}\frac{k^{3/2}}{\varepsilon_k} \qquad (4.94)$$

has to be specified a priori. Here it is assumed that the local length scale l_m corresponds to the cross-stream length scale δ_τ. The local cross-stream gradient in the production is again approximated with

the local shear time scale (eq. (4.11)) so that

$$v_T = c_t \, \delta_\tau \, k^{1/2} \,, \tag{4.95}$$

$$\mathscr{P}_k = v_T \, \frac{1}{\mathscr{T}^{(c)\,2}_{shear}} = v_T \left(\frac{U_c}{\delta_\tau} \right)^2 \,, \tag{4.96}$$

$$\varepsilon_k = \frac{C_\mu \, k^{3/2}}{c_t \, \delta_\tau} \,. \tag{4.97}$$

Yet one more level in detail is incorporated in a so called two equation model where the turbulent length scale is variable and a separate transport equation for the dissipation rate ε_k is solved [93].

$$\frac{\partial \varepsilon_k}{\partial t} + \frac{\partial (\varepsilon_k \, U_c)}{\partial \xi} + \frac{(\varepsilon_k \, U_c)}{\xi} = \frac{\partial}{\partial \xi} \left(\frac{v_T}{Pr_\varepsilon} \frac{\partial \varepsilon_k}{\partial \xi} \right) + C_{\varepsilon 1} \frac{\mathscr{P}_k \, \varepsilon_k}{k} - C_{\varepsilon 2} \frac{\varepsilon_k^2}{k} \tag{4.98}$$

C_μ	c_t	$C_{\varepsilon 1}$	$C_{\varepsilon 2}$	Pr_k	Pr_ε
0.09	0.55	1.44	1.92	1	1.3

Table 4.3: One- and two-equation turbulence model constants [93]

4.6 Summary

Mass and momentum conservation of the two-phase jet are described by four variables $(M_p, U_p, \delta_\tau, U_c)$ which are a function of the independent variables ξ and t. The four corresponding transport equations are compactly repeated in the following.

$$\frac{\partial M_p}{\partial t} + \frac{\partial (M_p \, U_p)}{\partial \xi} + \frac{M_p \, U_p}{\xi} = \Gamma_p \tag{4.4}$$

$$\frac{\partial (M_p \, U_p)}{\partial t} + \frac{\partial (M_p \, U_p^2)}{\partial \xi} + \frac{M_p \, U_p^2}{\xi} = -\mathscr{F}_D \tag{4.7}$$

$$\frac{\partial \delta_\tau}{\partial t} + \frac{4 \, \delta_\tau}{U_c} \frac{\partial U_c}{\partial t} + \delta_\tau \frac{\partial U_c}{\partial \xi} \left(3.55 - 0.75 \frac{\delta_\tau}{\xi \, \tan \theta} \right)$$
$$+ \delta_\tau \frac{U_c}{\xi} \left(0.75 - 0.5 \frac{\delta_\tau}{\xi \, \tan \theta} \right) + 0.9 \, U_c \frac{\partial \delta_\tau}{\partial \xi} = \frac{6 \, \nu_{eff}}{\delta_\tau} \tag{4.46}$$

The effective viscosity is the sum of the molecular and the turbulent viscosity

$$\nu_{eff} = \frac{\mu_c}{\rho_c^{(DSZ)}} + \nu_T \tag{4.99}$$

where the turbulent viscosity ν_T is defined by equation (4.91) in the turbulence section (sec. 4.5).

The dispersed phase experiences the total drag force

$$\mathscr{F}_D = M_p \frac{18 \, \mu_c \, f_{SN}}{\rho_p \, D_p^2} \, (U_p - U_c) . \tag{4.6}$$

Part of the total drag force is diffusively transported away from the dense spray zone at either side of the hollow cone sheet (factor "2" in

the numerator of eq. (4.25)) so that the carrier phase is only exposed to an effective drag force

$$\frac{\partial U_c}{\partial t} + U_c \frac{\partial U_c}{\partial \xi} = \frac{\mathscr{F}_D}{\rho_c^{(DSZ)}} - 2 \, v_{eff} \frac{U_c}{\delta_\tau^2} = \Phi_D^{(eff)} \, . \tag{4.25}$$

If evaporation is considered, equations for three additional variables (the temperatures of both phases T_p and T_c and the fuel species mass fraction $Y_F = \frac{M_F}{M_c}$) are solved.

$$\frac{\partial Y_F}{\partial t} + \frac{\partial (Y_F \, U_c)}{\partial \xi} + \frac{Y_F \, U_c}{\xi} = \frac{1}{\rho_c^{(DSZ)}} \left(\Gamma^{(evap)} - 2 \cdot \Gamma_{Y_F}^{(diff)} \right) \tag{4.56}$$

$$\frac{\partial (M_p \, T_p)}{\partial t} + \frac{\partial (M_p \, T_p \, U_p)}{\partial \xi} + \frac{M_p \, T_p \, U_p}{\xi} = \frac{\Pi_p}{C_l} \tag{4.63}$$

$$\frac{\partial T_c}{\partial t} + \frac{\partial (T_c \, U_c)}{\partial \xi} + \frac{T_c \, U_c}{\xi} = \frac{1}{\rho_c^{(DSZ)} \, C_v} \left(2 \cdot \Pi_c^{(diff)} - \Pi_p \right) \tag{4.64}$$

The source terms are defined by equations (4.57), (4.60), (4.65), and (4.69).

If an additional contribution to the cross-stream boundary layer thickness δ_τ resulting from turbulent fluctuations of the carrier phase is considered, an additional conservation equation for the turbulent kinetic energy at the DSZ is solved.

$$\frac{\partial k}{\partial t} + \frac{\partial (k \, U_c)}{\partial \xi} + \frac{k \, U_c}{\xi} = \underbrace{\frac{\partial}{\partial \xi} \left(\frac{v_T}{Pr_T} \frac{\partial k}{\partial \xi} \right)}_{\Pi_{v_T}} + \mathscr{P}_k - \varepsilon_k \, . \tag{4.90}$$

5 Conclusion

In this thesis hollow cone sprays are investigated. A thorough discussion of both two-phase flow physics as well as available models and a boundary layer assessment of the hollow cone flow is carried out (section 2). Based on an experimentally validated CFD model, the two-phase flow induced by the injection is characterized (section 3) before the main findings are utilized to derive a simplified spray model. Finally, its behavior (namely momentum exchange and evaporation) at constant global thermodynamic conditions is studied (section 4).

The vast range of physical length and time scales incorporated in internal combustion engines for automotive applications necessitates the development of simplified models for injection processes. For direct injecting gasoline engines applying multiple injections per working cycle, the need of a transient and one-dimensional spray model is established (section 2.3). The assessment of the hollow cone boundary layer shows that the second order cross-stream term dominates the viscous terms (section 2.4.1).

The analysis of the experimentally validated CFD model reveals that comparatively simple physical models (Eulerian dispersed phase treatment with only one particle size class) sufficiently describe flow characteristics such as the global penetration of the dispersed phase and the induced carrier phase velocity field outside the dense hollow cone spray very well (section 3.2.2).
The strong acceleration of the carrier phase due to injected liquid fuel induces cross-stream velocity profiles similar to those resulting from an accelerated wall (section 3.2.3). Even when turbulent effects such as a turbulent dispersion force on the liquid phase lead to broader

cross-stream profiles, this flow pattern is maintained, especially close to the injection outlet. The resulting shear forces limit the acceleration of the carrier phase, which is directly exposed to the dispersed phase. As a result, the injection induced carrier phase boundary layer is crucial for the evolution of the momentum exchange along the main injection direction and the global penetration depth.

Due to the non-symmetric environment of the dense spray elements, a flow pattern develops which is non-symmetric with respect to the hollow cone geometry. Nevertheless, the injection direction – which is prescribed by the injector design – is found to be the dominant flow direction, also at positions further away from the injection outlet (section 3.2.4).

A simplified spray model for hollow cone sprays is presented. It is based on the main two-phase characteristics first introduced in section 2 and supported by the CFD analysis (section 3.2). According to the discussed requirements of engine system simulation, the description is

- *two-phase*, i.e. no mixture model assumption is applied, but momentum as well as energy conservation are covered for each phase by separate transport equations;

- *transient*, i.e. the response to time-invariant boundary conditions is implicitly described (the conservation equations contain temporal rates of change of the conserved variables);

- *one-dimensional*, i.e. fluxes along the main injection direction are accounted for (the description contains the steamwise gradients of the conserved variables).

As the first major modeling step, the model employs the property of the "accelerated wall" type cross-stream velocity profile: With respect to the carrier phase, the dispersed phase mass is modeled to occupy a cross-stream width approaching zero (the "dense spray zone" DSZ, section 4.3.1). The second most distinctive modeling part is the deriva-

tion of a transport equation for the cross-stream length scale, which is characteristic to the mean diffusion rate of mass, momentum, and energy in the cross-stream direction (section 4.3.3).

The proposed *transient two-phase boundary layer (ttBL)* model is first assessed with respect to momentum conservation transport. The model produces the well known square root shape of the streamwise boundary layer profile for a single phase jet (section 4.3.6.1).
For the injection induced two-phase flow (section 4.3.6.2), the contraction term in the transport equation for the cross-stream length scale (accounting for "excess entrainment" of carrier phase mass into the dense spray region) limits the cross-stream growth of the boundary layer. The temporal development of the spray front position depending on the global thermodynamic state of the carrier phase corresponds to the experimental data (section 4.3.6.3).
The modeling assumption of a characteristic cross-stream length scale is also applied to both thermal energy diffusion towards and fuel vapor species diffusion away from the dense spray region (section 4.4). The results provide a qualitative insight into the (due to the saturation state within the DSZ) highly non-linear evolution of liquid phase warm-up and fuel species concentration.

The proposed *ttBL* model constitutes a new approach to two-phase flow modeling of dense sprays: It extends the commonly applied Schiller-Naumann drag law and the Spalding evaporation model. The carrier phase fluxes of momentum, thermal energy, and fuel species are primarily controlled by diffusion through the boundary layer adjacent to the dense spray. While the model is applied to a one-dimensional description here, it may well serve as a sub-grid model to multi-dimensional flow simulation models.

While in general, the predictions of the *ttBL* model are in good agreement with experimental data, some discrepancies may be observed:
The velocity magnitude of convective transport within the carrier phase during injection obtained by the ttBL model is comparatively low. Al-

though measurements of the "true" carrier phase velocity in regions of highest dispersed phase volume loading are not available, increased magnitudes of carrier phase velocity (such as observed from the CFD results in section 3.2.4) should be expected.

The low carrier phase velocity magnitudes result from the small cross-stream length scales characterizing the shear force. They again are a result of the "excess entrainment" term in the cross-stream length scale transport equation; and the weights of the terms in the transport equation result from the presumed cross-stream profile shape and the upper integration limit applied in section 4.3.3. During the derivation of the model both have been intuitively chosen (i.e. a Taylor series expansion of second order as the most general profile shape featuring a non-zero curvature and a spatial integration over just the length scale which is modeled).

Further attention may focus on both the CFD modeling and the one-dimensional model: When further analyzing evaporation by means of CFD, more detail will have to be incorporated, especially the consideration of poly-dispersion. Since smaller particles are also more affected by turbulent fluctuations, turbulence effects will need to be investigated in more detail. The proposed ttBL model requires further development. As next steps, the model's sensitivity to turbulence effects, the choice of the cross-steam length scale measure characterizing the cross-stream diffusion, and its ability to appropriately describe the diffusion of energy and species mass require future attention.

Bibliography

[1] Abraham, J.: *What is adequate resolution in the numerical computations of transient jets?* SAE Paper 970051, 1997.

[2] Abramovich, G.: *The theory of turbulent jets*. M.I.T. Press, 1963.

[3] Adomeit, Ph. and S. Pischinger and: *Analysis of cyclic fluctuations of charge motion and mixture formation in a DISI engine in stratified operation*. SAE Paper 2007-01-1412, 2007.

[4] Anderson, J.: *Computational Fluid Dynamics*. Mcgraw-Hill, 1995.

[5] Ansys, Inc.: *Ansys cfx solver, release 10*.

[6] Apte, S., K. Maheshy, and T. Lundgren: *A Eulerian-Lagrangian model to simulate two-phase/particulate fows*. In *Center for Turbulence Research*, 2003.

[7] Aramburo, E.: *A new methodology for modelling impinging sprays based on drop size moments*. PhD thesis, Univ. Manchester, 2004.

[8] Atkins, P. and J de Paula: *Physical chemistry*. Oxford Univ. Press, 2006.

[9] Atthasit, A.: *Etude experimentale des phenomenes d'interaction dans les jet diphasiques denses au moyen de jets rectilihnes momodisperses*. PhD thesis, L'ecole nationale superieure de l'aeronautique et de l'espace, 2003.

[10] Automotive, Continental: *Spray characterization of two piezo-injectors for different fuels using multiple optical measurement techniques*. Internal communication, 2007.

[11] Batchelor, G.: *An introduction to fluid dynamics*. Cambridge Math. Library, 2000.

[12] Baumgarten, C.: *Mixture Formation in Internal Combustion Engines*. Springer, 2006.

[13] Baumgarten, C., J. Stegemann, and G. Merker: *A new model for cavitation induced primary breakup of Diesel sprays*. Proc. 18th ILASS Europe, pages 15 – 20, 2002.

[14] Beck, J.: *Computational modelling of polydisperse sprays without segregation into droplet size classes*. PhD thesis, Univ. Manchester, 2000.

[15] Beck, J. and A. Watkins: *On the development of spray submodels based on droplet size moments*. J. Comp. Phys., 182:586 – 621, 2002.

[16] Beck, J. and A. Watkins: *The droplet number moments approach to spray modelling: The development of heat and mass transfer sub-models*. Int. J. Heat Fluid Flow, 24:242 – 259, 2003.

[17] Beck, J. and A. Watkins: *On the development of a spray model based on drop-size moments*. Proc. Roy. Soc. London, 459:1365 – 1394, 2003.

[18] Bocksell, T. and E. Loth: *Random walk models for particle diffusion in free-shear flows*. AIAA Journal, 39:1086 – 1096, 2001.

[19] Boivin, M., O. Simonin, and K. Squires: *Direct numerical simulation of turbulence modulation by particles in isotropic turbulence*. J. Fluid Mech., 375:235 – 263, 1998.

[20] Bollweg, P. and A. Kaufmann: *Dynamic burn rate modeling for the 1D simulation of a gdi engine in homogeneous and stratified operation mode*. SAE Int. J. Engines, 1(1):1045 – 1056, 2008.

[21] Bollweg, P., A. Kaufmann, and W. Polifke: *Derivation and application of a poly-celerid method for poly-dispersed two-phase flows*. In *6th International Conference Multiphase Flow*, 2007.

[22] Brennen: *Fundamentals of Multiphase Flow*. Cambridge Univ. Pr., 2005.

[23] Brown, D. and E. Kauppinen: *A method of moments based cfd model for polydisperse aerosol flows with strong interphase mass and heat transfer*. Comp. Fluids, 35:762 – 780, 2006.

[24] Burns, A., T. Frank, . Hamill, and J. Shi: *The Favre averaged drag model for turbulent dispersion in Eulerian multi-phase flows*. In *Int. Conf. on Multiphase Flow*, 2004.

[25] Carvalho, I., M. Heitoyr, and D. Santos: *Liquid film disintegration*. Int. J. Multiphase Flow, 28:773 – 789, 2002.

[26] Castagné, M., E. Chevé, J. Dumas, and S. Henriot: *Advanced tools for analysis of gasoline direct injection engines*. SAE Paper 2000-01-1903, 2000.

[27] Chapman, S. and T. Cowling: *The mathematical theory of non-uniform gases*. Cambridge Univ. Press, 1970.

[28] Chryssakis, C., K. Driscoll, and V. Sick ad D. Assanis: *Validation of an enhanced liquid sheet atomozation model against quantitative laser diagnostic measurements*. In *ILASS Europe*, 2002.

[29] Chryssakis, Ch., D. Assanis, J. Lee, and K. Nishida: *Fuel spray simulation of high-pressure swirl-injector for disi engines and comparison with laser diagnostic measurements*. SAE Paper 2003-01-0007, 2003.

[30] Colin, O., F. Ducros, and D. Veynante: *A thickened flame model for large eddy simulations of turbulent premixed combustion.* Phys. Fluids, 12, 2000.

[31] Cossali, G.: *An integrated model for gas entrainment into full cone sprays.* J. Fluid Mech., 439:353 – 366, 2001.

[32] Cousin, J. and H. Nuglisch: *Modeling of internal flow in high pressure swirl injectors.* SAE Paper 2001-01-0963, 2001.

[33] Crowe, C.: *On models for turbulence modulation in fluid-particle flows.* Int. J. Multiphase Flow, 26:719 – 727, 2000.

[34] Crowe, C., M. Sommerfeld, and Y. Tsuji: *Multiphase Flows with Droplets and Particles.* CRC Press, 1998.

[35] da Pinna, A. and G. Corbinelli: *Measurement of the penetraion depth of a hollow cone spray in a constant pressure chamber.* Internal Communication, Siemens AG, 2004.

[36] de Francqueville, L., B. Thirouard, V. Ricordeau, J. Cherel, and L. Hermant: *Experimental investigation of the air entrainment characteristics within the periphery of a gasoline direct injection (GDI) spray by PIV.* In *ILASS Americas*, 2005.

[37] de Luca, L. and M. Costa: *Instability of a spatially developing sheet.* J. Fluid Mech., 337:127 – 144, 1997.

[38] Deen, N. and J. Kuipers: *Numerical simulation of dense gas-particle flows using the Euler-Lagrange approach.* Prog. Comp. Fluid Dynamics, 7, 2007.

[39] Delay, G.: *Analyse des ecoulements transitoires dans les systemes d'injection directe essence effets sor l'entainement d'air instationnaire du spray.* PhD thesis, INP Toulouse, 2005.

[40] Delay, G., A. Arbeau, R. Bazile, and G. Charnay: *Experimental analysis of density effects on air entrainment in Diesel and gasoline dense sprays by PIV on fluorescent dyes.* In *6th World*

Conference on Experimental Heat Transfer, Fluid Mechanics, and Thermodynamics, 2005.

[41] Delay, G., R. Bazile, G. Charnay, and H. Nuglisch: *Coupling between instantaneous liquid flow rate and transient air entrainment for GDI sprays*. In *3ʳᵈ International symposium on two-phase flow modeling and experimentation*, 2004.

[42] Delay, G., R. Bazile, G. Charnay, and H. Nuglisch: *Temporal dependency of air entrainement to liquid flow rate variations for gasoline direct injection sprays*. In *12ᵗʰ International Symposium on Applications of Laser Techniques to Fluid Mechanics*, 2004.

[43] Desjardins, O., R. Fox, and P. Villedieu: *A quadrature-based moment closure for the Williams spray equation*. In *Center for Turbulence Research*, 2006.

[44] Domingo, P., L. Vervisch, and J. Réveillon: *Dns analysis of partially premixed combustion in spray and gaseous turbulent flame-bases stabilized in hot air*. Combust. Flame, 140 (3):172 – 195, 2005.

[45] Drew, D. and S. Passman: *Theory of Multicomponent Fluids*. Springer, New York, 1999.

[46] Elghobashi, S. and T. Abou-Arab: *A two-equation turbulence model for two-phase flows*. Phys. Fluids, 26:931 – 938, 1983.

[47] Elghobashi, S. and G. Truesdell: *On the two-way interaction between homogeneous turbulence and dispersed solid particles. i: Turbulence modification*. Phys. Fluids, 7:1790 – 1801, 1993.

[48] Fan, R., D. Marchisio, and R. Fox: *Application of the direct quadrature method of moments to polydisperse gas-solid fluidized beds*. Powder Technology, 139:7 – 20, 2004.

[49] Fefferman, C.: *Existence and smoothness of the Navier-Stokes equations (official problem descrip-*

tion). In *http://www.claymath.org/millennium/Navier-Stokes_Equations/navierstokes.pdf (Clay Mathematics Institute)*, 2008.

[50] Ferry, J. and S. Balachandar: *A fast Eulerian method for disperse two-phase flow.* Int. J. Multiphase Flow, 27:1199 – 1226, 2001.

[51] Ferry, J. and S. Balachandar: *Equilibrium expansion for the Eulerian velocity of small particles.* Powder Technol., 125:131 – 139, 2002.

[52] Ferziger, J. and M. Peric: *Computational Methods for Fluid Dynamics.* Springer, 2002.

[53] Fevrier, P. and O. Simonin: *Constitutive relations for fluid-particle velocity correlations in gas-solid turbulent flows.* In *Int. conf. on multiphase flows*, 1998.

[54] Fornberg, B.: *Generation of finite difference formulas on arbitrarily spaced grids.* Mathematics of Computation, 51(184):699 – 706, 1988.

[55] Fornberg, B.: *Calculation of weights in finite difference formulas.* Society of industrial and Applied Mathematics Review, 40(3):685 – 691, 1998.

[56] Gharaibah, E., M. Brandt, and W. Polifke: *Numerical model of dispersed two phase flow in aerated stirred vessels based on presumed shape number density functions.* In *Proc. of the German-Japanese Workshop on Multi-Phase Flow*, 2002.

[57] Han, Z., L. Fan, and R.D. Reitz: *Multidimensional modeling of spray atomization and air-fuel mixing in a direct-injection spark-ignition engine.* SAE Paper, (970884), 1997.

[58] Hentschel, W., A. Homburg, G. Ohmstede, T. Müller, and G. Grünefeld: *Investigation of spray formation of DI gasoline*

hollow-cone injectors inside a pressure chamber and a glass ring engine by multiple optical techniques. SAE Paper 1999-01-3660, 1999.

[59] Heywood, J.: *Internal combustion engine fundamentals*. McGraw-Hill, 1988.

[60] Hieber, D.: *An investigation of the mesh dependence of the stochastic discrete droplet model applied to dense liquid sprays*. Master's thesis, Michigan Techn. University, 2001.

[61] Hiroyasu, H.: *Break-up length of a liquid jet and internal flow in a nozzle*. In *ICLASS-91*, 1991.

[62] Hiroyasu, H., T. Kadota, and M. Arai: *Development and use of a spray combustion model to predict Diesel engine efficiency and pollutant emissions*. JSME, 26:569 – 583, 1983.

[63] Hirsch, C.: *Numerical Computation of Internal and External Flows*, volume 2: Computational Methods for Inviscid and Viscous Flows. John Wiley & Sons, New York, 1990.

[64] Hunt, J., A. Wray, and P. Moin: *Eddies, stream and convergende zones in turbulent flows*. In *CTR summer program*, 1988.

[65] Ishii, M. and T. Hibiki: *Thermo-fluid Dynamics of Two-Phase Flow*. Springer, 2005.

[66] Jazayeri, S. and X. Li: *Nonlinear instability of plane liquid sheet*. J. Fluid Mech., 406:281 – 308, 2000.

[67] Jeong, J. and F. Hussain: *On the identification of a vortex*. J. Fluid Mech., 285:69 – 94, 1995.

[68] Kaufmann, A.: *Towards Eulerian-Eulerian Large Eddy Simulation of Reactive Two-Phase Flows*. PhD thesis, CERFACS, 2004.

[69] Kim, I. and W. Sirignano: *Three-dimensional wavedistortion and disintegration of thin planar liquid sheets*. J. Fluid Mech., 410:147 – 183, 2000.

[70] Kolev, N.: *Multiphase Flow Dynamics 1 – Fundamentals*. Springer, 2004.

[71] Kouremenos, D., C. Rakopoulos, and D. Hountalas: *Multi-zone modeling for the prediction of pollutant emissions and performance of DI Diesel engines*. SAE Paper 970635, 1997.

[72] Krueger, Chr.: *Validierung eines 1D-Spraymodells zur Simulation der Gemischbildung in direkteinspritzenden Dieselmotoren*. PhD thesis, RWTH Aachen, 2001.

[73] Kuo, K.: *Principles of Combustion*. John Wiley & Sons, Inc., Hoboken, New Jersey, USA, 2005.

[74] Langen, P., T. Melcher, S. Missy, and C. Schwarz: *New BMW Six- and Four-Cylinder Petrol Engines with High Precision Injection and Stratified Combustion*. In 28th *Int. Vienna Engine Symp.*, 2007.

[75] Laurent, F., M. Massot, and P. Villedieu: *Eulerian multi-fuid modeling for the numerical simulation of polydisperse dense liquid sprays*. J. Comp. Phys., 194:505 – 543, 2004.

[76] Li, X. and R. Tankin: *On the temporal instability of a two-dimensional viscous liquid sheet*. J. Fluid Mech., 220:425 – 443, 1991.

[77] Liepmann, H. and A. Roshko: *Elements of gasdynamics*. Dover publications, 1957.

[78] Lin, S., Z. Lian, and B. Creighton: *Absolute and convective instability of a liquid sheet*. J. Fluid Mech., 220:673 – 689, 1990.

[79] Lopez de Bertodano, M.: *Two fluid model for two-phase turbulent jets*. Nuclear engineering and design, 179:65 – 74, 1998.

[80] Loth, E.: *An Eulerian turbulent diffusion model for particles and bubbles*. Int. J. Multiphase Flow, 27:1051 – 1063, 2001.

[81] Madsen, J.: *Computational and experimental study of sprays from the breakup of water sheets*. PhD thesis, 2006.

[82] Malvern, Inc.: *Spray particle analyzer*. page http://www.malvern.de/LabGer/products/spraytec/spraytec.htm, 2008.

[83] Marchi, A., J. Nourl, Y. Yan, and C. Arcoumanis: *Internal flow and spray characteristics of pintle-type outwards opening piezo injectors for gasoline direct-injection engines*. SAE Paper 2007-01-1406, 2007.

[84] Marchisio, D. and R. Fox: *Solution of population balance equations using the direct quadrature method of moments*. J. Aerosol. Sci., 36:43 – 73, 2005.

[85] Marmottant, P. and E. Villermaux: *On spray formation*. J. Fluid Mech., 421:73 – 111, 2004.

[86] Massol, A.: *Simulations numeriques d'ecoulements a travers des reseaux fixes de spheres monodisperses et bidisperses, pour des nombres de Reynolds moderes*. PhD thesis, INP Toulouse, 2004.

[87] Mehring, C. and W. Sirignano: *Nonlinear capillary wave distortion and disintegration of thin planar liquid sheets*. J. Fluid Mech., 388:69 – 113, 1999.

[88] Menter, F.: *Two-equation eddy-viscosity turbulence models for engineering applications*. AIAA journal, 32:1598 – 1605, 1994.

[89] Moon, S., Ch. Bae, J. Choi, and E. Abo-Serie: *The influence of airflow on fuel spray characteristics from a slit injector*. Fuel, 86:400 – 409, 2007.

[90] Mossa, J.: *Extension polydisperse pour la description Euler-Euler des ecoulements diphasiques reactives*. PhD thesis, INP Toulouse, 2005.

[91] Ortmann, R., S. Arndt, J. Raimann, R. Grzeszik, and G. Würfel: *Methods and analysis of fuel injection, mixture preparation and charge stratification in different direct injected si engines*. SAE Paper 2001-01-0970, 2001.

[92] Peters, N. and J. Göttgens: *Scaling of buoyant turbulent jet diffusion flames*. Comb. Flame, 85:206 – 214, 1991.

[93] Pope, S.: *Turbulent Flows*. Cambridge Univ. Press, 2000.

[94] Prandtl, L. and O. Tietjens: *Fundamentals of hydrodynamics and aeromechanics*. Dover publications, 1934.

[95] Preussner, C., C. Döring, S. Fehler, and S. Kampmann: *GDI: Interaction between mixture preparation, combustion system and injector performance*. SAE Paper 980498, 1998.

[96] Prosperetti, A.: *Computational Methods for Multiphase Flow*. Cambridge Univ Pr, 2006.

[97] Prosperi, B.: *Analyse de l'entrainement d'air induit par le developpement instationnaire d'un spray conique creux. Application a l'injection directe essence*. PhD thesis, IMF Toulouse, 2008.

[98] Prosperi, B., J. Helie, and R. Bazile: *PIV measurements of injection pressure influence on gas entrainment in GDI engines*. In *ILASS Europe*, 2007.

[99] Renz, U.: *Heat and mass transfer (lecture script)*. Lehrstuhl fuer Waermebertragung und Klimatechnik, RWTH Aachen, Aachen, 2002.

[100] Riber, E.: *Developpement de la methode de simulation aux grandes echelles pour les ecoulements diphasiques turbulents*. PhD thesis, INP Toulouse, 2007.

[101] Roisman, I., L. Araneo, and C. Tropea: *Effect of ambient pressure on penetration of a diesel spray*. Int. J. Multiphase Flow, 33:904 – 920, 2007.

[102] Rusche, H.: *Computational Fluid Dynamcis of Dispersed Two-Phase Flows at High Phase Fractions*. PhD thesis, Imperial College London, 2002.

[103] Saber, H. and M. El-Genk: *On the breakup of a thin liquid film subject to interfacial shear*. J. Fluid Mech., 421:113 – 133, 2004.

[104] Sato, Y. and K. Sekoguchi: *Liquid velocity distribution in two-phase bubbly flow*. Int. J. Multiphase Flow, 2:79, 1975.

[105] Sazhin, S., C. Crua, D. Kennaird, and M. Heikal: *The initial stage of fuel spray penetration*. Fuel, 82:875 – 885, 2003.

[106] Scheele, M.: *Potentialabschaetzung zur Verbesserung des indizierten Wirkungsgrades kleinvolumiger Ottomotoren*. PhD thesis, Hannover Univ., 1999.

[107] Schiller, L. and A. Naumann: *A drag coefficient correlation*. VDI Zeitung, 77:318 – 320, 1935.

[108] Schlichting, H. and K. Gersten: *Boundary Layer Theory*. Springer, 2001.

[109] Schroeder, W.: *Fluidmechanik*. Wissenschaftsverlag Mainz in Aachen, 2000.

[110] Schwarz, C., E. Schuenemann, and B. Durst: *Potentials of the spray-guided BMW DI combustion system*. SAE Paper 2006-01-1265, 2006.

[111] Senecal, P., D. Schmidt, I. Nouar, C. Rutland, R. Reitz, and M. Corradini: *Modeling high-speed viscous liquid sheet atomization*. Int. J. Multiphase Flow, 25:1073 – 1097, 1999.

[112] Silverman, I. and W. Sirignano: *Multi-droplet interaction effects in dense sprays*. Int. J. Multiphase Flow, 20:99 – 116, 1994.

[113] Simonin, O.: *Prediction of the dispersed phase turbulence in partcle-laden jets*. In *Proc. 4th int. symp. on gas solid flows*. ASME FED, 1991.

[114] Simonin, O.: *Combustion and turbulence in two-phase flows*. Lecture series, von Karman institute for fluid dynamics, 1996.

[115] Simonin, O., P. Fevrier, and J. Lavieville: *On the spacial distribution of heavy-particle velocities in turbulent flow: from continuous field to particulate chaos*. J. of Turbulence, 3, 2002.

[116] Sirignano, W.: *Fluid Dynamics and Transport of Droplets and Sprays*. Cambridge University Press, Cambridge, 1999.

[117] Smagorinski, J.: *General circulation experiments with the primitive equations. i. the basic experiment*. Monthly Weather Review, 91:99 – 164, 1963.

[118] Sommerfeld, M.: *Review of numerical modeling of dispersed two-phase flows: A stochastic Lagrangian model*. In *Fifth Int. Symp. on Refined Flow Modeling and Turbulence Measurement*, 1993.

[119] Sommerfeld, M.: *Inter-particle collisions in turbulent flows: A Lagrangian model*. In *First int. symp. on turbulence and shear flow phenomena*, 1999.

[120] Squire, K. and J. Eaton: *Particle response and turbulence modification in isotropic turbulence*. Phys. Fluids A, 2:1191 – 1203, 1990.

[121] Squire, K. and Eaton J: *Effect of selective modification of turbulence on two-equation models for particle-laden turbulent flows*. J. Fluid Engng, 116:778 – 784, 1994.

[122] Stiesch, G.: *Modeling Engine Spray and Combustion Processes. Heat and Mass Transfer*. Springer, 2003.

[123] Suh, E. and C. Rutland: *Numerical study of fuel/air mixture preparation in a GDI engine*. SAE Paper 1999-01-3657, 1999.

[124] Tennekes, M. and J. Lumley: *A First Course in Turbulence*. MIT Press, 1972.

[125] Tryggvason, G., Bunner B. Esmaeeli A. Juric D. Al Rawahi N. Tauber W. Han J. Nas S. & Jan Y. J: *A front-tracking method for the com- putations of multiphase flow*. J. Comp. Phys., 169:708 – 759, 2001.

[126] Vermorel, O., B. Bedat, O. Simonin, and T. Poinsot: *Numerical study and modelling of turbulence modulation in a particle laden slab flow*. JoT, 4, 2003.

[127] Villedieu, Ph. and O. Simonin: *Modeling of coalescence in turbulent gas-droplet flows*. Comm. Math. Sci., 1:13 – 33, 2004.

[128] Virepinte, J.: *Edude du comportement dynamique et thermique de thermique de gouttes en regime d'interaction dans le cas de jets rectilignes*. PhD thesis, L'ecole nationale superieure de l'aeronautique et de l'espace, 1999.

[129] Wan, Y.: *Numerical Study of Transient Fuel Sprays with Autoignition and Combustion Under Diesel-Engine Relevant Conditions*. PhD thesis, RWTH Aachen, 1997.

[130] Warnecke, V., E. Achleitner, and H. Baecker: *Development status of the Siemens VDO piezo injection system for spray-guided combustion*. In *27th Int. Vienna Engine Symp.*, 2006.

[131] Williams, F.: *Spray combustion and atomization*. Phys. Fluids, 1:541 – 545, 1958.

A Navier-Stokes equations in conical coordinates

Conical coordinates

Conical coordinates and adjacent velocities according to figure 3.2.1

$$\xi = r\sin\theta - z\cos\theta \qquad \hat{u} = u\sin\theta - w\cos\theta \qquad \text{(A.1)}$$

$$\eta = r\cos\theta + z\sin\theta \qquad \hat{w} = u\cos\theta + w\sin\theta \qquad \text{(A.2)}$$

or inversely

$$r = \xi\sin\theta + \eta\cos\theta \qquad u = \hat{u}\sin\theta + \hat{w}\cos\theta \qquad \text{(A.3)}$$

$$z = -\xi\cos\theta + \eta\sin\theta \qquad w = -\hat{u}\cos\theta + \hat{w}\sin\theta \qquad \text{(A.4)}$$

Transformation of the partial differentials

$$
\begin{aligned}
\begin{pmatrix} \frac{\partial}{\partial r} \\ \frac{\partial}{\partial z} \end{pmatrix}
&= \begin{pmatrix} \frac{\partial \xi}{\partial r}\frac{\partial}{\partial \xi} + \frac{\partial \eta}{\partial r}\frac{\partial}{\partial \eta} \\ \frac{\partial \xi}{\partial z}\frac{\partial}{\partial \xi} + \frac{\partial \eta}{\partial z}\frac{\partial}{\partial \eta} \end{pmatrix}
= \begin{pmatrix} \frac{\partial}{\partial r}\xi & \frac{\partial}{\partial r}\eta \\ \frac{\partial}{\partial z}\xi & \frac{\partial}{\partial z}\eta \end{pmatrix}\begin{pmatrix} \frac{\partial}{\partial \xi} \\ \frac{\partial}{\partial \eta} \end{pmatrix} \\
&= \left[\begin{pmatrix} \frac{\partial}{\partial r} \\ \frac{\partial}{\partial z} \end{pmatrix}(\xi \quad \eta) \right]\begin{pmatrix} \frac{\partial}{\partial \xi} \\ \frac{\partial}{\partial \eta} \end{pmatrix} = \begin{pmatrix} \sin\theta & \cos\theta \\ -\cos\theta & \sin\theta \end{pmatrix}\begin{pmatrix} \frac{\partial}{\partial \xi} \\ \frac{\partial}{\partial \eta} \end{pmatrix}
\end{aligned}
\qquad \text{(A.5)}
$$

Conservative

Continuity

$$\frac{\partial}{\partial t}\rho + \frac{\partial}{\partial \xi}\rho\hat{u} + \frac{\partial}{\partial \eta}\rho\hat{v} + \rho\frac{\hat{u}\,\sin\theta + \hat{v}\,\cos\theta}{\xi\,\sin\theta + \eta\,\cos\theta} = \Gamma^{(e)} \qquad \text{(A.6)}$$

Momentum along main injection direction (ξ-direction)

$$\frac{\partial}{\partial t}\rho\hat{u} + \frac{\partial}{\partial \xi}\rho\hat{u}^2 + \frac{\partial}{\partial \eta}\rho\hat{u}\hat{v} + \rho \underbrace{\frac{\hat{u}^2 \, \sin\theta + \hat{u}\hat{v} \, \cos\theta}{\xi \, \sin\theta + \eta \, \cos\theta}}_{R^{(m)}}$$

$$= -\frac{\partial P}{\partial \xi} + \mu \left[\frac{\partial^2 \hat{u}}{\partial \xi^2} + \frac{\sin\theta \, \frac{\partial \hat{u}}{\partial \xi} + \cos\theta \, \frac{\partial \hat{u}}{\partial \eta}}{\xi \, \sin\theta + \eta \, \cos\theta} + \frac{\partial^2 \hat{u}}{\partial \eta^2} - \sin\theta \, \frac{\hat{u} \, \sin\theta + \hat{v} \, \cos\theta}{(\xi \, \sin\theta + \eta \, \cos\theta)^2} \right] + I^{(m}$$

(A.7)

Momentum normal to the main injection direction (η-direction)

$$\frac{\partial}{\partial t}\rho\hat{v} + \frac{\partial}{\partial \xi}\rho\hat{u}\hat{v} + \frac{\partial}{\partial \eta}\rho\hat{v}^2 + \rho \underbrace{\frac{\hat{u}\hat{v} \, \sin\theta + \hat{v}^2 \, \cos\theta}{\xi \, \sin\theta + \eta \, \cos\theta}}_{R^{(n)}}$$

$$= -\frac{\partial P}{\partial \eta} + \mu \left[\frac{\partial^2 \hat{v}}{\partial \xi^2} + \frac{\sin\theta \, \frac{\partial \hat{v}}{\partial \xi} + \cos\theta \, \frac{\partial \hat{v}}{\partial \eta}}{\xi \, \sin\theta + \eta \, \cos\theta} + \frac{\partial^2 \hat{v}}{\partial \eta^2} - \cos\theta \, \frac{\hat{u} \, \sin\theta + \hat{v} \, \cos\theta}{(\xi \, \sin\theta + \eta \, \cos\theta)^2} \right] + J^{(n}$$

(A.8)

Primitive

"Axial" momentum (along main injection direction ξ), incompressible, primitive

$$\frac{\partial \hat{u}}{\partial t} + \hat{u} \, \frac{\partial \hat{u}}{\partial \xi} + \hat{v} \, \frac{\partial \hat{u}}{\partial \eta} = -\frac{1}{\rho} \frac{\partial}{\partial \xi} P$$

$$+ \nu \left[\frac{\partial^2 \hat{u}}{\partial \xi^2} + \frac{\sin\theta \, \frac{\partial \hat{u}}{\partial \xi} + \cos\theta \, \frac{\partial \hat{u}}{\partial \eta}}{\xi \, \sin\theta + \eta \, \cos\theta} + \frac{\partial^2 \hat{u}}{\partial \eta^2} - \sin\theta \, \frac{\hat{u} \, \sin\theta + \hat{v} \, \cos\theta}{(\xi \, \sin\theta + \eta \, \cos\theta)^2} \right] + I^{(m)}$$

(A.9)

"Radial" momentum (normal to the main injection direction η)

$$
\frac{\partial \hat{v}}{\partial t} + \hat{u}\frac{\partial \hat{v}}{\partial \xi} + \hat{v}\frac{\partial \hat{v}}{\partial \eta} = -\frac{1}{\rho}\frac{\partial P}{\partial \eta}
$$

$$
+ \nu \left[\frac{\partial^2 \hat{v}}{\partial \xi^2} + \frac{\sin\theta\ \frac{\partial \hat{v}}{\partial \xi} + \cos\theta\ \frac{\partial \hat{v}}{\partial \eta}}{\xi\ \sin\theta + \eta\ \cos\theta} + \frac{\partial^2 \hat{v}}{\partial \eta^2} - \cos\theta\ \frac{\hat{u}\ \sin\theta + \hat{v}\ \cos\theta}{(\xi\ \sin\theta + \eta\ \cos\theta)^2} \right] + J^{(m)}
$$

$$(A.10)$$

B Boundary layer fluxes

With the assumption of the cross-stream velocity profile according to eq. (4.32), a certain amount of momentum I is contained within a boundary layer of thickness δ_τ and of centerline velocity U_c. When the local boundary layer is exposed to transient flow conditions (i.e. due to a drag force), also the local boundary layer thickness scale δ_τ changes: $\frac{\partial \delta_\tau}{\partial t} \neq 0$.

Figure B.1 describes the boundary layer in a quiescent and non-deformable control volume. At some streamwise position x, consider a control volume of length ∂x, width b and height $\delta(x)$. Fluid enters the control volume with the velocity $u(x, y)$ from the left. At the right boundary, fluid leaves the control volume with the velocity $u(x + \partial x, y) = u(x) + \partial u$. At the upper boundary, the fluid carries the streamwise velocity $u' = u(x', y = \delta)$ which may be linearly approximated
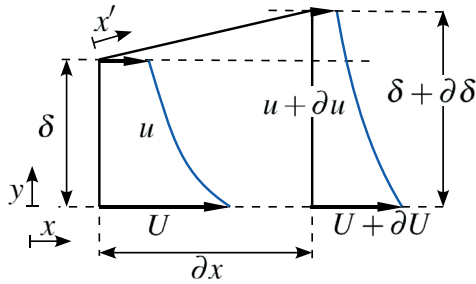
$$u(x', \delta) = u(x, \delta) + \frac{\partial u}{\partial x} x' . \tag{B.1}$$

The same applies to the cross-stream velocity component

$$v(x', \delta) = v(x, \delta) + \frac{\partial v}{\partial x} x' \tag{B.2}$$

at the upper boundary of the control volume.

According to Reynolds' transport theorem, the rate of change of B contained in a control volume CV is obtained by integration over the

Figure B.1: Boundary layer control volume; sketch

conserved quantity *b*. The rate of change

$$\frac{\partial B}{\partial t} = \int\limits_{CV} \rho \, b \, dV + \int\limits_{CS} \rho \, b \, (\vec{v} \cdot \vec{n}) \, dA \qquad \text{(B.3)}$$

is composed by volume sources (integral over the control volume *CV*) and the net flux across the control volume boundary (integral over the control surface *CS*).

Steady state convection

In the steady state flow condition, the mass

$$\frac{\partial m}{\partial t} = \int \rho \, (\vec{v} \cdot \vec{n}) \, dA = 0 \qquad \text{(B.4)}$$

and momentum equations

$$\frac{\partial I}{\partial t} = \int \rho \, \vec{v} \, (\vec{v} \cdot \vec{n}) \, dA = \sum \vec{F}_{ext} \qquad \text{(B.5)}$$

are obtained. For the control volume as depicted in figure B.1, the continuity equation (divided by $(\rho\,b)$)

$$\frac{\dot{m}}{\rho\,b} = 0 =$$

$$-\int_{y=0}^{\delta} u\,dy + \int_{y=0}^{\delta+\partial\delta} (u+\partial u)\,dy - \int_{x'=x}^{x+\partial x'} u'\,\sin\alpha\,dx' + \int_{x'=x}^{x+\partial x'} v'\,\cos\alpha\,dx'$$

(B.6)

and the convective part of the streamwise momentum equation

$$\frac{i_x^{(conv)}}{\rho\,b}$$

$$= -\int_{y=0}^{\delta} u^2\,dy + \int_{y=0}^{\delta+\partial\delta} (u+\partial u)^2\,dy - \int_{x'=x}^{x+\partial x'} u'^2\,\sin\alpha\,dx' + \int_{x'=x}^{x+\partial x'} u'\,v'\,\cos\alpha\,dx'$$

$$= -\int_{y=0}^{\delta} (2\,u\,\partial u + (\partial u)^2)\,dy + \int_{y=\delta}^{\delta+\partial\delta} (u+\partial u)^2\,dy$$

$$-\int_{x'=x}^{x+\partial x'} u'^2\,\sin\alpha\,dx' + \int_{x'=x}^{x+\partial x'} u'\,v'\,\cos\alpha\,dx'$$

(B.7)

are formed. The inclined length increment of the upper boundary dx' may be expressed in terms of the streamwise increment dx:

$$\sin\alpha\,dx' = \partial\delta = \tan\alpha\,dx = \frac{\partial\delta}{\partial x}\,dx \qquad \text{and} \qquad \cos\alpha\,dx' = dx\,.$$

(B.8)

Also, the increment of the upper integration limit $\partial x'$ may be approximated:

$$\partial x' = \sqrt{(\partial x)^2 + (\partial \delta)^2} \, . \tag{B.9}$$

For the flow investigated here, cross-stream gradients are orders of magnitude larger than the corresponding streamwise gradients (cp. the boundary layer assumption in eq. (4.15)). As a consequence, the cross-stream characteristic length scale is $\partial \delta \ll \partial x$ and $\partial x' \rightarrow \partial x$. The continuity equation simplifies to

$$\frac{\dot{m}}{\rho \, b} = 0 = \int_{y=0}^{\delta} \partial u \, dy + \int_{y=\delta}^{\delta+\partial\delta} (u + \partial u) \, dy - \frac{\partial \delta}{\partial x} \int_{x'=x}^{x+dx} u' \, dx' + \int_{x'=x}^{x+dx} v' \, dx' \, . \tag{B.10}$$

The second last term defines the mass flux due to the gradient $\frac{\partial \delta}{\partial x}$ while the last term represents the mass flux due to convection through the upper boundary at $\eta = \delta$.

The simplified streamwise momentum convection reads*

$$\frac{\dot{i}_x^{(conv)}}{\rho \, b} = - \int_{y=0}^{\delta} (2 \, u \, \partial u + (\partial u)^2) \, dy + \int_{y=\delta}^{\delta+\partial\delta} (u + \partial u)^2 \, dy$$

$$- \frac{\partial \delta}{\partial x} \int_{x'=x}^{x+dx} u'^2 \, dx' + \int_{x'=x}^{x+dx} u' \, v' \, dx' \, . \tag{B.11}$$

With the presumed cross-stream velocity profile (equation (4.32)), the integrals may be evaluated. For simplicity, the results for the plane 2D

---

* If u' would be constant – i.e. if the upper boundary would be in the free flow regime –, the last term could easily be substituted by the continuity equation. In that case $\partial \delta = 0$.

case are presented here:

$$u(y) = \hat{U}(y) = U \left(1 - \frac{y}{\delta} + \frac{y^2}{2\,\delta^2}\right)$$

$$\partial u(y) = \partial \hat{U}(y) = \partial U \left(1 - \frac{y}{\delta} + \frac{y^2}{2\,\delta^2}\right) + U\,\frac{y}{\delta^2}\left(1 - \frac{y}{\delta}\right)\partial\delta\,,$$

$$\text{(B.12)}$$

so that at the upper boundary $y = \delta$,

$$u' = \hat{U}(y = \delta) = \frac{U}{2} \qquad \text{and} \qquad v' = \hat{V}(y = \delta) = -\frac{1}{2}\,\frac{\partial(\delta U)}{\partial x}$$

$$\frac{\partial u'}{\partial x} = \frac{\partial \hat{U}(y = \delta)}{\partial x} = \frac{1}{2}\,\frac{\partial U}{\partial x} \qquad \text{and} \qquad \frac{\partial v'}{\partial x} = -\frac{1}{2}\,\frac{\partial^2(\delta U)}{\partial x^2}$$

$$\text{(B.13)}$$

If the assumed velocity profile is inserted, the continuity equation

$$\frac{1}{\rho\,b}\,\frac{d\dot{m}^{(conv)}}{dx} = \frac{\delta}{2}\,\frac{dU}{dx} - \frac{1}{3}\,\frac{d(\delta U)}{dx} = \frac{\delta}{6}\,\frac{dU}{dx} - \frac{1}{3}\,U\,\frac{d\delta}{dx} \qquad \text{(B.14)}$$

and the convective part of the streamwise momentum

$$\frac{1}{\rho\,b}\,\frac{d\dot{I}_x^{(conv)}}{dx} = \frac{37}{30}\,U\delta\,\frac{dU}{dx} - \frac{1}{4}\left[\left(\frac{d(\delta U)}{dx} + x\cdot\frac{d^2(\delta U)}{dx^2}\right)\left(U + x\cdot\frac{d(\delta U)}{dx}\right)\right]$$

$$= \frac{59}{60}\,U\delta\,\frac{dU}{dx} - \frac{1}{4}\,U^2\,\frac{\partial\delta}{\partial x}$$

$$- \frac{1}{4}\,x\left[\left(\frac{d(\delta U)}{dx}\right)^2 + \left(U + x\cdot\frac{\partial(\delta U)}{\partial x}\right)\frac{d^2(\delta U)}{dx^2}\right]$$

$$\text{(B.15)}$$

are obtained.

If the flow decelerates along the streamwise direction ($\frac{\partial U}{\partial x} < 0$), the

contained mass flux increases along the streamwise direction ($\frac{\partial \dot{m}}{\partial x} > 0$). Because at constant speed ($\frac{\partial u}{\partial x} = 0$) and at increasing boundary layer thickness ($\frac{\partial \delta}{\partial x} > 0$) more mass leaves the control volume at the right side in figure B.1, the net contained mass flux decreases along the steamwise direction: $\frac{\partial \dot{m}}{\partial x} < 0$.

For the assessment of the integral momentum equation (B.15), first consider streamwise profiles of $\delta(x)$ and $U(x)$ so that $\frac{\partial (\delta U)}{\partial x} = 0$. In that case, the streamwise momentum flux due to convection changes proportionally to the contained momentum δU and proportional to the steamwise velocity gradient $\frac{\partial U}{\partial x}$. In a steady jet flow, usually $\frac{\partial \delta}{\partial x} > 0$ and $\frac{\partial U}{\partial x} < 0$ so that for $\frac{\partial (\delta U)}{\partial x} = 0$, the momentum flux contained in the control volume (fig. B.1) decreases along the streamwise direction: $\frac{d I_x^{(conv)}}{dx} < 0$. This corresponds to the observation on the continuity equation above: The assumed changes in the cross-stream velocity profile cause the amount of momentum leaving the control volume on the right to exceed the momentum entering from the left. [†]

[†] The Reynolds stress tensor

$$\sigma_{ji} = \tau_{ji} - -p\,\delta_{ji} = \mu \left(\frac{\partial u_j}{\partial x_i} + \frac{\partial u_i}{\partial x_j} \right) - p\,\delta_{ji} \qquad \text{(B.16)}$$

For the evaluation of the shear stresses τ_{ji}, the Gauss theorem

$$\int_{\delta V} \frac{\partial u_i}{\partial x_j} dA_i = \int_V \frac{\partial}{\partial x_i} \frac{\partial u_i}{\partial x_j} dV = \int_V \frac{\partial}{\partial x_j} \frac{\partial u_i}{\partial x_i} dV = 0 \qquad \text{(B.17)}$$

in combination with the incompressibility assumption ($\frac{\partial u_i}{\partial x_i} = 0$) indicate that the terms due to the surface integrals $\int_{\delta V} \frac{\partial u_i}{\partial x_j} dA_i = 0$.

Steady state momentum diffusion

In the streamwise direction, the contribution of the boundary integrals

$$
\int_{y=0}^{\delta} \tau_{1i}\, dA_i + \int_{y=0}^{\delta+\partial\delta} \tau_{1i}\, dA_i = -b \int_{y=0}^{\delta} \mu \frac{\partial u}{\partial x}\bigg|_{x}\, dy + b \int_{y=0}^{\delta+\partial\delta} \mu \frac{\partial u}{\partial x}\bigg|_{x+dx}\, dy
$$

$$(B.18)$$

to the streamwise momentum integral are negligible for flow conditions outside the viscous dominated regime with Reynolds numbers $\mathrm{Re} \ll 1$.

The assumed cross-stream velocity profile (eq. (4.32)) results in a constant diffusion rate across the boundary layer of thickness $\partial\delta$ so that the momentum flux within the control volume does not change due to cross-stream viscous diffusion. Because $\frac{\partial u}{\partial y}\big|_{y=0} = -\frac{U}{\delta}$, the shear stress introduced to the control volume at the lower boundary is

$$
\int \tau_{1i}\, dA_i = -b \int_{x'=x}^{x+\partial x'} \mu \; \frac{\partial u}{\partial y}\bigg|_{y=0}\, dx' = b\,\mu\, \frac{U}{\delta}\, dx\,.
$$

$$(B.19)$$

Because pressure fluctuations are assumed to propagate fast compared to convective fluxes ($Ma < 0.3$), the contribution of pressure gradients to the streamwise momentum equation is neglected here.

Transient flow

The analysis of the momentum fluxes within the boundary layer and their changes due to the proposed model is based on a quiescent and non-deformable control volume. A temporarily changing control volume (boundary layer thickness) is excluded from the analysis.

But if the changes of mass and momentum fluxes due to $\frac{\partial\delta}{\partial t} \neq 0$ are conceived as volume source terms, the contribution of the variable

boundary layer thickness may be characterized:

$$\left(\frac{\partial m}{\partial t}\right)^{(trans)} = \frac{\partial}{\partial t}\int_{\partial V}\rho\,dV = \frac{\partial}{\partial t}\left(\rho\,b\,dx\int_{y=0}^{\delta}dy\right) = \rho\,b\,dx\,\frac{\partial\delta}{\partial t}\,,$$

$$\text{(B.20)}$$

$$\left(\frac{\partial I_x}{\partial t}\right)^{(trans)} = \frac{\partial}{\partial t}\int_{\partial V}\rho\,u\,dV = \frac{\partial}{\partial t}\left(\rho\,b\,dx\int_{y=0}^{\delta}u\,dy\right) = \rho\,b\,dx\,\frac{2}{3}\frac{\partial(\delta U)}{\partial t}\,.$$

$$\text{(B.21)}$$

In combination with the convective parts (equaitons (B.14) and (B.15)) and the diffusive term (equation (B.19)), you obtain

$$\frac{1}{\rho\,b}\frac{\partial\dot{m}}{\partial x} = \frac{\partial\delta}{\partial t} = \frac{\delta}{6}\frac{dU}{dx} - \frac{1}{3}U\frac{d\delta}{dx} \qquad \text{(B.22)}$$

and

$$\frac{1}{\rho\,b}\frac{\partial\dot{I}_x}{\partial x} = \frac{2}{3}\frac{\partial(\delta U)}{\partial t}$$

$$= \frac{59}{60}U\delta\frac{dU}{dx} - \frac{1}{4}U^2\frac{\partial\delta}{\partial x}$$

$$-\frac{1}{4}x\left[\left(\frac{d(\delta U)}{dx}\right)^2 + \left(U + x\cdot\frac{\partial(\delta U)}{\partial x}\right)\frac{d^2(\delta U)}{dx^2}\right]$$

$$-v\frac{U}{\delta}\,.$$

$$\text{(B.23)}$$